HIGH TEMPERATURE SPINTRONIC DEVICES

by

Debashish Basu

A dissertation submitted in partial fulfillment
of the requirements for the degree of
Doctor of Philosophy
(Electrical Engineering)
in The University of Michigan
2010

Doctoral Committee:

Professor Pallab K. Bhattacharya, Chair
Professor Duncan G. Steel
Associate Professor Jamie D. Phillips
Associate Professor Kevin P. Pipe

© Debashish Basu 2010
All Rights Reserved

To

PKB

ACKNOWLEDGMENTS

I would like to express my heartfelt gratitude to all those who have contributed or have been involved in my dissertation work. First and foremost I would like to thank my thesis advisor Prof. Pallab Bhattacharya, for giving me this opportunity to work on cutting-edge research. His unique way of handling the toughest scientific challenges through clever ingenuity and sheer persistence has been and will be a constant source of motivation for all my endeavors. I also want to thank other members of my doctoral committee: Professors Duncan Steel, Kevin Pipe, and Jamie Phillips, for their time, insightful comments, and valuable suggestions.

My thesis would not be even half complete without the immense contribution put forward by Dr. Dipankar Saha. His constant help and encouragement has helped me cross numerous hurdles I have faced in realizing the devices that are part of this thesis. I would like to thank Dr. Jonghyun Shin, Dr. Michael Holub, Dr. Jun Yang and Chi-sen Lee for their help in getting me acquainted with epitaxial growth, device fabrication and characterization. I am also thankful to Dr Guan Huang, Hyun Kum, Ayan Das and Dr. Wei Guo for their constant support. I would like to extend my gratitude to those graduate students with whom I have not directly collaborated but whose assistance is greatly appreciated. I thank Dr Swapnajit Chakrabarty, Dr. Weiming Wang, Dr. Kuen-Ting Shu, Junseok Heo, Animesh Banerjee, Sishir Bhowmick, Min Kim, Shafat Jahangir and Meng Zhang for their support.

A notable portion of the data presented in my thesis was acquired using instruments and equipments belonging to other groups. I would like to acknowledge Dr.

Chris Kojiro for his help with the Quantum Design SQUID magnetometer located at the chemistry department and Gwanghyeon Baek for his help in reflectivity measurements.

Excellent support of the Lurie nanofabrication facility staff is greatly appreciated. My special thanks to Dennis Schweiger and Dr Dennis Grimard, whose generous help and cheerful demeanor have helped me come out of seemingly hopeless situations. I would also like to thank Edward Tang, Leslie George, Matthew Oonk, Sandrine Martin and Gregory McEwan for their mentorship and help in device fabrication and characterization. I am grateful to Kyle Banas of DCO for the help he extended whenever we had issues with our computer and to people in the mechanical workshop for the help they extended.

I thank Melanie Caughey, Lisa Vogel, Denise Oscar, Laura Jarels, Deb Swartz, Frances Doman, and Beth Stalnaker for administrative support throughout my graduate career. I wish to acknowledge the University of Michigan Rackham Graduate School for providing partial fellowships to support my graduate education, the Office of Naval Research and the National Science Foundation for funding this research.

TABLE OF CONTENTS

DEDICATION ii

ACKNOWLEDGMENTS iii

LIST OF FIGURES viii

LIST OF TABLES xvi

LIST OF APPENDICES xvii

ABSTRACT xviii

CHAPTER

I. BACKGROUND 1

1.1 Introduction 1
1.2 Spintronics 3
1.2.1 Spin injection and detection 3
1.2.2 Spin transport 6
1.2.3 Spin orbit interaction and spin manipulation 14
1.3 Semiconductor Spintronics 16
1.3.1 Dilute magnetic materials 17
1.3.2 Ferromagnetic metal spin injectors 18
1.3.3 Half metallic metal spin injectors 19
1.3.4 Semiconductor spintronic devices 21
1.4 Organization of Thesis 22

II. EPITAXIAL GROWTH AND CHARACTERIZATION OF FERROMAGNETIC MnAs 26

2.1 Introduction 26
2.2 Epitaxially grown MnAs thin films 28
2.3 Magnetic properties and characterization 33
2.4 Electrical injection and detection of spin injection in MnAs/ $In_{0.52}Al_{0.48}As$ lateral spin valves 37
2.5 Summary 41

III. ELECTRIC FIELD CONTROL OF MAGNETORESISTANCE IN A LATERAL InAs QUANTUM WELL SPIN VALVE 43

3.1 Introduction 43
3.2 Design, growth and fabrication of modulation doped InAs /$In_{0.53}Ga_{0.47}As$/ $In_{0.52}Al_{0.48}As$ heterostructure 44
3.3 Device measurement and characterization 46
3.4 Control experiments 51
3.5 Summary 52

IV. CHARACTERISTICS OF A HIGH TEMPERATURE VERTICAL SPIN VALVE: THE ROLE OF DEFECT FREE P-DOPED GaAs...... 53

4.1 Introduction 53
4.2 Design, epitaxial growth and fabrication of a vertical spin valve 54
4.3 Energy band diagrams and valence band electron tunneling................ 57
4.4 Experimental characterization and device modeling 61
4.5 Control devices 65
4.6 Conclusion 67

V. HIGH TEMPERATURE InAs/GaAs QUANTUM DOT SPIN LASER: DESIGN AND FABRICATION 68

5.1 Introduction 68
5.2 Epitaxial growth and fabrication 70
5.3 Threshold current reduction and output circular polarization 71
5.4 Modeling of QD spin VCSEL 75
5.5 Conclusion 77

VI. ELECTRICAL MODULATION OF POLARIZATION AND GAIN ANISOTROPY OF A SPIN LASER 78

6.1 Introduction 78
6.2 Analysis of laser characteristics from spin polarized laser rate equations 79
6.3 Device characterization and modeling 83
6.4 Polarization modulation in a spin laser under continuous wave excitation 85
6.5 Conclusion 87

VII. TRANSIENT CHARACTERISTICS OF AN ELECTRICALLY INJECTED QUANTUM DOT SPIN LASER:THE CASE FOR 100% OUTPUT POLARIZATION 88

7.1 Introduction 88
7.2 Calculated small- and large-signal modulation characteristics of a spin laser 90
7.3 Output polarization 98

7.4 Experimental results: Characteristics of quantum dot spin VCSELs ... 99
7.5 Conclusion 103

VIII. CONCLUSIONS AND SUGGESTIONS FOR FUTURE WORK . 105

8.1 Summary of Completed Work 105
8.1.1 Spin polarized lasers 105
8.1.2 Spin polarized electronic devices....................................... 106
8.2 Suggestions for Future Work 107
8.2.1 Spin injectors with out-of-plane easy axis of magnetization 107
8.2.2 High temperature spin polarized Fabry-Perot lasers........... 107
8.2.3 Vertical Spin transistors.. 110

APPENDICES 112

BIBLIOGRAPHY 139

LIST OF FIGURES

Figure

1.1: Gamut of different physical phenomenon associated with spintronics. 2

1.2: Technology performance evaluation chart of spin transistors showing different aspects of device realization and compatibility. 2

1.3: Schematic diagrams of the density of states of a ferromagnetic injector/detector and a non-magnetic metal/semiconductor. In (a) zero bias condition; (b) finite bias condition. 4

1.4: Schematic shows the measurement geometry for non-local spin accumulation in metals or semiconductors. 6

1.5: A schematic representation showing measuring non-local spin accumulation by detecting of spin Hall voltages using the lateral spin valve type geometry. 7

1.6: Measurement geometry for estimating spin accumulation and precession using the lateral spin valve type geometry. 8

1.7: Allowed radiative interband transitions in case of quantum confined structures where the degenracy of the HH and LH is lifted by epitaxial strain and confinement. 9

1.8: Schematic representation of the electron-phonon mediated spin flip. 10

1.9: Shows the origin of DP spin relaxation mechanism in non-centrosymmetric semiconductors. 11

1.10: Shows the origin of BAP spin relaxation mechanism in degenerately p doped semiconductors. 12

1.11: Shows the nature of hyperfine interaction involving spin polarized electron and a spin polarized atomic nucleus. 13

1.12: Spin relaxation in n-type GaAs with (a) doping concentratio and; (b) temperature. 13

1.13: Schematic showing the working principle behind the ballistic spin transistor using Rashba spin-orbit couping. 15

1.14: The density of states for a typical 3d-ferromagnet. The partially filled d-bands are split by the exchange interaction. 18

1.15: Classification of half-metals. The diagrams show schematic densities of states for spin-up (red) and spin-down (blue) electrons. E_F is the Fermi energy, E_μ is the mobility edge energy, Δ is the gap for one electron spin, and Δ_{sf} is the spin-flip gap. (a) Type IA (e.g., CrO_2) and (b) Type IB (e.g., Sr_2FeMoO_6) half-metals have only a or b electrons at the Fermi level, with a gap for the other spin direction. (c) Type II half-metals are similar to Type I, but have narrow bands where the electrons are localized, and conduction is by hopping; shown here is a Type IIB half-metal (e.g., Fe_3O_4). (d) Type III half-metals have a mixture of delocalized electrons with one spin direction and localized electrons with the other; shown here is a Type IIIA half-metal (e.g., $La_{0.7}Sr_{0.3}MnO_3$). The illustration on the left in (a) shows a cation in octahedral oxygen coordination and the splitting of the one-electron energy levels into t2g and eg states. In a solid, these states broaden to form the 3d bands.. 20

1.16: Crystal structures of full Heusler alloys, half Heusler alloys. 21

1.17: Schematic repesentation of the different types of semiconductor based spin polarized devices realized to date.(a) Spin polarized optoelectronic device; (b) Lateral spin based electrical device and;(c) vertical spin based electrical device. 21

2.1: A ball and stick diagram showing the arrangement of atoms together with the lattice constants for ferromagnetic MnAs. 27

2.2: RHEED pattern of a c(2×4)-InP(001) surface taken along the (a) [110] and (b) [1$\bar{1}$0] azimuths.. 28

2.3: RHEED pattern of a type-B MnAs film taken along the (a) [110] and (b) [1$\bar{1}$0] azimuths in the presence of an As_4 flux during the nucleation phase. RHEED pattern taken along the (c) [110] and (d) [1$\bar{1}$0] azimuths before the annealing the sample. 29

2.4: RHEED pattern of a type-B MnAs film taken along the [1$\bar{1}$0] azimuths in the presence of an As_4 flux during the anneal phase. 30

2.5: Roughness and surface morphology of MnAs film (2.5 μm × 2.5 μm) (left) and (500 nm × 500 nm) (right): (a) after 5 nm of growth on (001)InP. Micrographs shows an area of 2.5 μm × 2.5 μm; (b) after 5 nm of growth on (001)InP. Micrographs show an area of 500 nm × 500 nm; (c) after annealing a 35 nm film on (001)InP. Micrographs show an area of 2.5 μm × 2.5 μm; (d) after annealing a 35 nm film on (001)InP. Micrographs show an area of 500 nm × 500 nm; (e) after annealing a 35 nm film on $In_{0.53}Ga_{0.47}As$ lattice matched to (001)InP. Micrographs show an area of 2.5 μm × 2.5 μm; (f) after annealing a 35 nm film on $In_{0.53}Ga_{0.47}As$ lattice matched to (001)InP. Micrographs show an area of 500 nm × 500 nm. 32

2.6: (a) Kerr rotation of epitaxially grown and annealed type-B MnAs on InP(001) measured at 10 K and 290 K with applied magnetic field in the $[1\bar{1}0]$ direction; (b) coercivity measured at different temperatures for 35 nm epitaxially grown layer. Inset shows the variation in $\Delta\theta_K$ as a function of temperature. The solid lines are drawn as a guide for the eye.. 34

2.7: (a) Normalized values of the longitudinal Kerr magneto-optic effect versus in-plane applied field H for the MnAs sample at room temperature; (b) Magnetic hysteresis measured for a 35 nm MnAs/InP(001) layer recorded at 10 K in the out-of-plane direction using a SQUID magnetometer. Inset shows variation of the normalized moment at low applied fields, indicating small remanence and coercivity.. 35

2.8: (a) The spin valve shows two MR peaks corresponding to the case when the polarizer and the analyzer are magnetized in opposite directions. The MR decreases with increasing temperature due to decreasing spin-relaxation time; (b) ΔV change as a function of applied magnetic field for a 0.8 μm channel length nonlocal spin valve. Open and closed symbols represent the cases of descending and ascending magnetic fields, respectively. 38

2.9: (a) Peak magnetoresistance vs channel length measured at 10 K. (b) Peak ΔV (= $V_{\uparrow\uparrow}$-$V_{\uparrow\downarrow}$) vs temperature for a 0.8 μm spin valve with applied biases of I_B=100, 200, 300, and 400 μA. The lines represent a linear least squares fit to the data. 39

2.10: Spin precession measurement in presence of perpendicular magnetic field. ... 41

3.1: Schematic representation of: (a) heterostructure of $InAs/In_{0.53}Ga_{0.47}As$ QW spin modulator with ferromagnetic MnAs as spin injector. The entire heterostructure is grown by molecular beam epitaxy; (b) biasing arrangement for the measurements which are done by applying a constant current bias across the MnAs polarizer and analyzer contacts of the spin valve and varying the gate bias V_G between the gate and polarizer

terminals. The variation of magnetoresistance with V_G is determined by measuring the difference in voltage V for parallel and antiparallel magnetization of the polarizer and analyzer. 45

3.2: Magnetoresistance measured at 10 K in a conventional spin valve fabricated with an identical heterostructure (figure 3.1(a)), without gate bias. The channel length for the device is 0.6 μm. The inset shows peak magnetoresistance vs. bias current measured in the same device at different temperatures. The dashed lines are guides to the eye. 47

3.3: Measured modulation of magnetoresistance with gate bias at 10 and 20K in an $InAs/In_{0.53}Ga_{0.47}As$ QW spin valve for (a) spin transport normal to direction of magnetization; and (b) spin transport parallel to direction of magnetization. The direction of magnetization is always along the $[1\bar{1}0]$ direction, which is the easy axis of magnetization of type B MnAs contacts. The insets show the measured output voltage V as a function of normalized V_G for parallel and antiparallel magnetization (maximum actual gate voltage applied for this measurement is 8V). 48

3.4: (a) Measured output voltage versus gate bias for parallel and antiparallel magnetization of the polarizer and analyzer contacts at a constant bias current of 150 uA.(b) The magnetoresistance vs. gate bias measured for a control device with non-magnetic analyzer. 49

3.5: Measured output voltage V for parallel and antiparallel magnetizations of the polarizer/analyzer, and magnetoresistance as a function of gate bias V_G for a GaAs spin valve with a gate terminal as shown in Fig. 1(b) (maximum actual gate voltage applied for this measurement is 5V).................................. 51

4.1: (a) Schematic band diagram to illustrate valence band electron tunneling from ferromagnet (FM) Fermi level to the empty valence band states of semiconductor (SC) through insulating tunnel barrier (TB); (b) semiconductor heterostructure and two terminal vertical spin valve for electrical spin injection and detection; (c) TEM image showing ferromagnet/semiconductor sharp interfaces; (d) x-ray diffraction measurements indicate absence of Mn segregation in the fully grown heterostructure;(e)α-phase MnAs peak seen as a shoulder to the (002)GaAs secondary peak at 33.03^o;and (f) magnetoresistance as a function of magnetic field in vertical spin-valves. Spin polarized electrons tunnel from MnAs Fermi level into the empty valence band states of p-doped GaAs. The carriers then drift and diffuse through GaAs. Finally, the spin polarized electrons tunnel out to the empty conduction band states of the second MnAs contact. 56

4.2: Energy band diagrams and electric field profile for different bias conditions and doping concentrations. Band diagrams for (a) $p = 9 \times 10^{19} cm^{-3}$

(degenerately doped) and $V_B = 0$, (b) $p = 2 \times 10^{19}$ cm^{-3} (non-degenerately doped) and $V_B = 0$, (c) $p = 9 \times 10^{19}$ cm^{-3} and $V_B = 1V$ (low bias), and (d) $p = 9 \times 10^{19}$ cm^{-3} and $V_B = 2V$ (high bias); (e) electric field profile under various operating conditions and doping densities. Electrons can directly tunnel from ferromagnet Fermi level to the empty valence band states of degenerately doped GaAs. Unpolarized electrons may tunnel out at large bias, which do not contribute to the spin polarized current. The electric field increases rapidly with bias at the drain end; (f) Energy band diagram for lightly *p*-doped ($p = 10^{17}$ cm^{-3}) GaAs:Mn layer. Under equilibrium condition, there is no available state for electrons to tunnel out into the second ferromagnetic (FM) contact. 59

4.3: Measured and calculated characteristics of vertical spin valves with p-doped GaAs channel. Measured peak magnetoresistance is shown as a function of (a) temperature and (b) bias. (c) MnAs polarization and (d) spin diffusion length and spin relaxation time as a function of temperature are shown. Reduced ferromagnetic contact polarization due to spin wave excitation (SW), spin independent tunneling (SIT) conduction due to the hopping transport at the ferromagnet/semiconductor interface, and spin relaxation (SR) in the GaAs channel can explain the observed dependency (also shown in (a)). The spin relaxation in the p-doped GaAs is dominated by the BAP mechanism which is found to be relatively insensitive to temperature for $T > 125$ K. 64

4.4: (a) Semiconductor heterostructure of the two terminal vertical spin valve for electrical spin injection and detection. In this device the manganese doping concentration was also increased to 1.5 %; (b) TEM image showing ferromagnet/semiconductor stacking faults and unclear interfaces. There is also significant segregration of manganese in the GaAs layer; and (c) magnetoresistance as a function of magnetic field in vertical spin-valves. (d) Measured and calculated characteristics of vertical spin valves with p-doped GaAs channel. 66

4.5: (a) Semiconductor heterostructure of the two terminal vertical spin valve for electrical spin injection and detection. In this device the thickness of the GaAs layer was reduced to 1 nm; (b) Measured characteristics of vertical spin valves with p-doped GaAs channel. 66

5.1: Schematic cross section of an InAs QD spin-VCSEL heterostructure with (a) magnetic and (b) nonmagnetic n-contact grown by MBE.. 71

5.2: Measured degree of output circular polarization vs magnetic field for a 15 μm mesa diameter MnAs spin-VCSEL (circle) and control VCSEL (square) measured at 200 K are shown. The spin-VCSEL polarization closely follows the out-of-plane magnetization curve for MnAs. 73

5.3: Threshold current reduction vs magnetic field for a 15 μm mesa diameter MnAs spin-VCSEL measured at 200 K. Inset shows the measured light-current characteristics. 74

5.4: (a) Emission intensity enhancement vs normalized current (I/I_{th}) measured for different magnetic fields; (b) variation in threshold current reduction ($\Delta I_{th}/I_{th}$) vs normalizedcurrent (I/I_{th}) measured at a magnetic field of 3.1T. 75

5.5: (a) Calculated threshold current reduction vs pump-current spin polarization for spin relaxation time τ_{sf} = 75 ps; (b) calculated variation of the spin polarization values in the barrier and in the QDs vs normalized current. 77

6.1: Heterostructure of GaAs-based spin-VCSEL grown by molecular beam epitaxy. The active (gain) region consists of 10 periods of self-organized InAs/GaAs quantum dotsplaced in a GaAs – λ cavity. The top DBR mirror consists of 5 pairs of ZnSe/MgF_2 deposited by PVD. The ferromagnetic MnAs/$Al_{0.1}Ga_{0.9}As$ tunnel injector contact is regrown selectively on GaAs after a mesa-etch stop, as shown in the figure. 79

6.2: Schematic representation of the variation of carriers spins polarization with distance from ferromagnetic contact (MnAs) in VCSEL in accordance with the spin diffusion equation. The barrier (cavity) is at distance x_1 and the quantum dot region is at distance x_2. The spin polarization decreases with increasing pump current. In the barrier and quantum dots the polarization decreases from $P_{spin,1}$ to $P_{spin,2}$ and Π_{S1} to Π_{S2}, respectively. 80

6.3: Data from 15 μm diameter InAs/GaAs QD spin VCSEL at 200 K: (a) calculated and measured reduction of threshold current with magnetic field applied perpendicular (hard axis) to the plane of the MnAs contact. The inset shows the calculated and measured percentage reduction of threshold current with field; (b) calculated variation of gain anisotropy parameter, as defined in Eqn. (5.9) (text) with normalized pump current. 84

6.4: (a) Calculated and measured modulation of output circular polarization of InAs/GaAs QD spin VCSEL as a function of normalized pump current at different magnetic fields. The inset shows calculated polarization for constant pump current spin polarization, instead of the variation of P_{spin} shown in Fig. 5.2; (b) measured modulation index versus pump current. The calculated values are shown for currents at and above threshold. 86

7.1: Calculated large-signal modulation characteristics of spin laser showing temporal variation and relaxation oscillations of (a) photon density, (b) electron density, and (c) output polarization. The output polarization of the spin laser reaches a value of 100% when the favored mode only is lasing

and the relaxation oscillations are initiated after the less favored mode attains threshold. 93

7.2: Calculated upper limit of relaxation oscillation frequency as a function of current density for the conventional and spin lasers. The oscillation frequency increases with increasing bias for both the polarization modes. The oscillation frequency of the conventional laser always lies in between the two modes of the spin laser. 94

7.3: Calculated small-signal frequency response of the spin laser when: (a) the favored polarization mode, and (b) both polarization modes are lasing. The response from a conventional laser is also shown for comparison. The spin laser bandwidth increases when only one mode is lasing and decreases when both the modes are lasing; (c) effect of gain compression (ε) on modulation bandwidth calculated for the spin and conventional lasers; (d) phasor diagram of the polarization modes. 95

7.4: (a) Time-averaged output circular polarization (Π_c) as a function of time for various t_{on} and t_{off} of an ideal square pulse bias with zero rise and fall times. Π_c can be tuned in a wide range by varying the ON and OFF period. The output circular polarization can be made very high independent of the spin relaxation time in the active region by suitably tuning the pulse width and duty cycle of the bias current; (b) Π_c calculated and measured for a spin laser with a pulse current bias having finite identical rise and fall times (1.5 ns). The simulations correspond to a quantum dot spin polarization of 6 % estimated for a 10 μm diameter VCSEL measured at 230 K. The dotted lines correspond to the time averaged output polarizations measured in these devices. 97

7.5: Spin VCSEL heterostructure grown by molecular beam epitaxy. The $MnAs/Al_{0.1}Ga_{0.9}As$ spin injector is formed by epitaxial regrowth. 98

7.6: (a) The measured dc light-current characteristics for a 10 μm mesa diameter spin-VCSEL measured at 230 K in the Faraday geometry. Inset shows threshold current reduction vs applied magnetic field; (b) Measured degree of time-average output circular polarization vs ton of the square pulse bias with rise and fall times of 1.5 ns. The inset shows the value of peak output polarization measured for different values of current bias. 102

8.1: Heterostructure of the proposed InP based wide quantum well edge emitting laser. 108

8.2: Light-output characteristics of an InP based multi-quantum well conventional edge emitting laser. 109

8.3: (a) Proposed spin-edge emitting laser with distinct spin injector pad sizes in order to realize fast polarization switching; (b) hysteresis characteristics of the ferromagnetic spin injector pads. 109

8.4: Schematic showing the heterostructure of the proposed spin based three terminal transistor. 110

8.5: Magnetoresistance versus gate bias characteristics measured at room temperature for an applied constant drain to source current bias of (a) I_{ds} = -1mA and; (b) I_{ds} = -3mA. 111

LIST OF TABLES

Table

1.1: Transition probability for allowed transitions and the polarization resulting from these transitions in case of a surface emitting device. 8

2.1: Basic lattice parameters of bulk ferromagnetic MnAs. 27

5.1: Quantum dot parameters at 200 K used to analyze spin laser performance characteristics. 76

7.1: Laser parameters used to study dynamic characteristics of spin laser. 104

LIST OF APPENDICES

Appendix

A. ANALYTICAL MODULATION OF BANDWIDTH CALCULATIONS OF A SPIN-POLARIZED LASER 112

B. SOLUTION OF DRIFT DIFFUSION EQUATION AND LASER RATE EQUATIONS AT STEADY STATE 119

B.1 Derivation of relation between P_{spin} and $\Pi_{s,b}$ 119
B.2 Field-dependent threshold current 120
B.3 Output polarization 120
B.4 Gain anisotropy parameter 121
B.5 Determination of quantum dot spin polarization Π_S in terms of laser parameters 121

C. SOLUTION OF DRIFT DIFFUSION EQUATION FOR A SPIN MODULATOR.. 123

C.1 Infinite channel approximation 123
C.2 Finite channel length 127

D. MOLECULAR BEAM EPITAXY 131

E. FABRICATION OF A SPIN VERTICAL CAVITY SURFACE EMITTING LASER 135

ABSTRACT

Spintronics is a rapidly developing multidisciplinary field which investigates avenues of exploiting the spin degree of freedom in charge carriers and the nucleus of atoms to design novel devices that would outperform existing ones based on complementary-metal-oxide-semiconductor (CMOS) technology. Spin-polarized semiconductor based coherent light sources promise an ability to predict, stabilize and control orthogonal polarization states with reduced input power requirements. This doctoral thesis investigates different aspects of design, epitaxial growth, fabrication, characterization and modeling of spin based electronic and optoelectronic devices working near room temperature.

We have demonstrated modulation of magnetoresistance in an InAs/ $In_{0.53}Ga_{0.47}As$/ $In_{0.52}Al_{0.48}As$ lateral spin valve with a gate electrode placed alongside the MnAs polarizer contact and outside the current transport channel. The results indicate that the change in magnetoresistance is caused, in part, by Rashba spin-orbit coupling due to the gate bias. In order to achieve higher working temperatures devices for real world applications MnAs/GaAs/MnAs based vertical spin valves have been realized. We have attributed the near room temperature operation of these devices to valence band electron tunneling of

spin polarized carriers in and out of a heavily p-doped GaAs:Mn layer. Peak magnetoresistance of 40 % and 1 % have been observed at 10 K and 300 K respectively.

The continuous wave as well as high frequency dynamics of spin-polarized carriers and photons in a spin laser have been studied. Besides lowering of threshold currents, it has been theoretically estimated that these devices can show larger small-signal modulation bandwidth and 100% output polarization, independent of the injected carrier spin polarization, under appropriate biasing conditions. Measurements were done at 230 K on a InAs/GaAs quantum dot spin vertical cavity surface emitting laser (VCSEL). A time-averaged output polarization of 55% is measured with an active region spin polarization of 5-6%. A peak threshold current reduction of 4.5 % and a polarization modulation index of 0.6 have been measured in these devices under continuous wave bias. The output characteristics, both DC and transient, match very well with those calculated from the theory.

CHAPTER I

Background

1.1 Introduction

Spintronics is a new and emerging field of research based fundamentally on the control of spin polarization of charge carriers in solid state devices. Research in this area has led to the realization of a new paradigm of electronic as well as optoelectronic devices with distinct potential advantages of reduced power consumption, increased integration densities, faster data transfer and consequently higher bandwidth compared to the conventional semiconductor based devices. Over the past few decades silicon micro electronics has seen unprecedented growth since the first experimental demonstration of the transistor. Moore's law, [1] proposed by Intel co-founder Gordon Moore, has been driving technology and innovations in this area since the first integrated circuits were realized in the late 1950's. The continued dimensional and functional scaling of complementary metal oxide semiconductor based electronic devices has resulted in new applications and features which have revolutionized the fields of information processing. In order to sustain such advancements several technologies have been explored as an alternative to the present day silicon devices. The research in the field of these emerging

devices as well as materials is primarily to ward off apparent stagnation in information processing capability once the CMOS technology approaches its fundamental limits. The international technology roadmap for semiconductors (ITRS) has identified several possible alternatives for CMOS in order to sustain circuit scaling

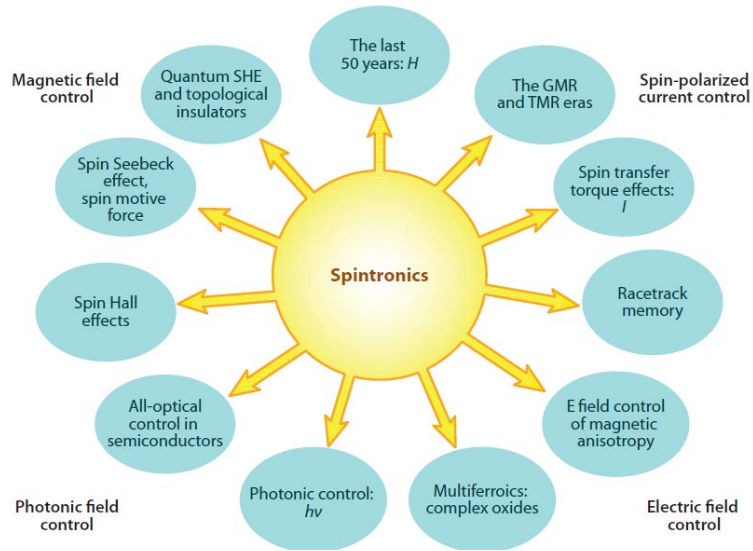

Fig 1.1: Gamut of different physical phenomenon associated with spintronics.

and to improve cost-to-function metric for future integrated circuits. [2] Spin

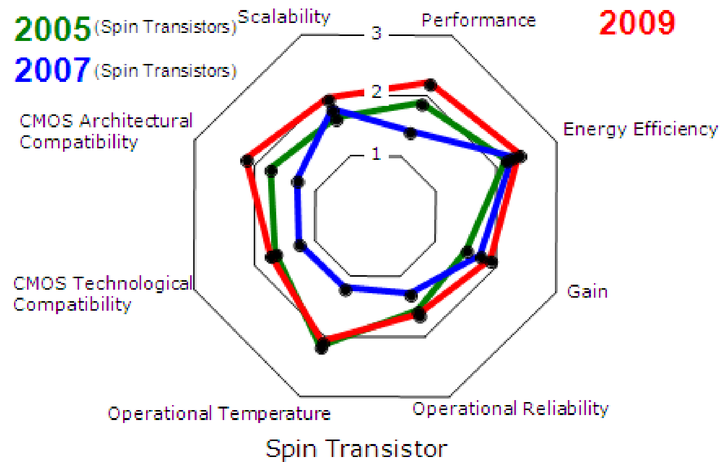

Fig 1.2: Technology performance evaluation chart of spin transistors showing different aspects of device realization and compatibility [2]

transistors, classified as "Non-conventional charge based extended CMOS devices", is one of many candidates which has received a lot of attention. Besides finding applications as an alternative to current CMOS spin polarized electrons can be used to study a whole gamut of novel physical phenomenon which might be of great scientific and future technological importance (Fig. 1.1). [3]

1.2 Spintronics

The commercial application of spintronic devices has been primarily in the area of all metal spin valves used in the realization of magnetic hard disks. The discovery of the giant magnetoresistive effect by Albert Fert and Peter Grunberg (Nobel prize 2007) [4,5] has stimulated a lot of research in all metallic as well as semiconductor based spintronics in the recent years. The four common aspects associated with any spin based device are spin injection, spin transport, spin manipulation and finally spin detection. Here we discuss these relevant processes in a more detail.

1.2.1 Spin Injection and Detection

The hierarchy starts with the injection of non-equilibrium spin into a conductor or into the conduction/valence band of a semiconductor. This can be achieved via optical excitation with circularly polarized light source (only in direct band gap semiconductors) or electrically using a ferromagnet as a contact. For optical excitation, the rules of momentum conservation dictate the orientation of the spin polarized electron-hole pairs that are created in the process. The efficiency with which the polarized carriers are generated in a semiconductor depends on whether the material has any degree of quantum confinement. In bulk semiconductors the efficiency is 50 % while in epitaxially strained 2D or 1D structures it is 100 %.[6] A more detailed treatment of optical effects

in semiconductors can be found elsewhere.[6]

In order to realize devices with practical applications electrical injection is quintessential. The fig. 1.3 is a schematic representation of the processes involved in the efficient injection of spin polarized carriers in a semiconductor or a metal.

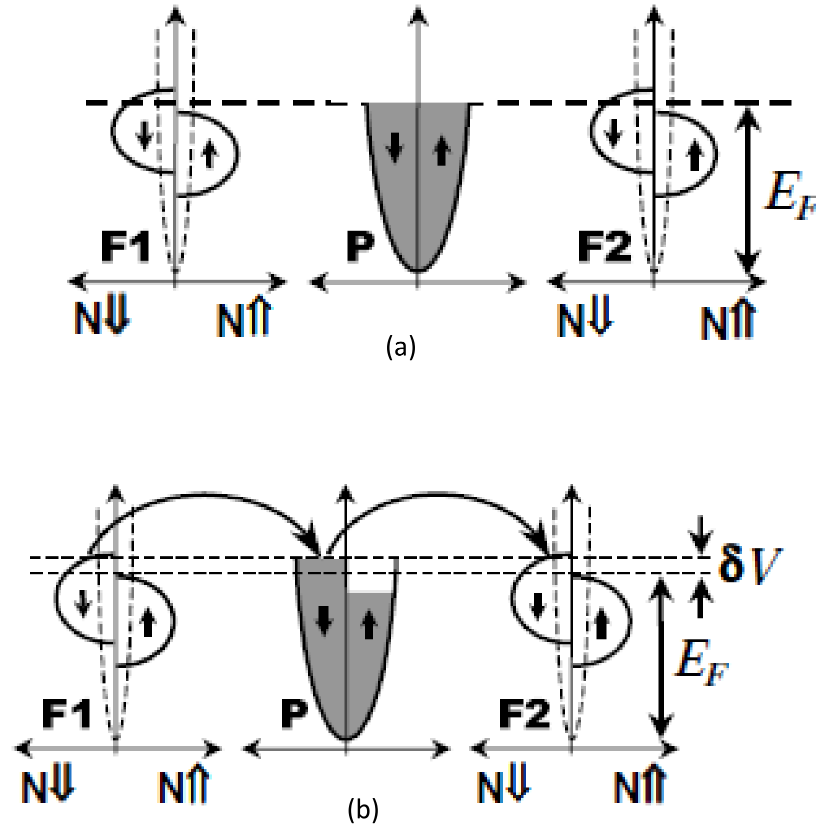

Fig.1.3: Schematic diagrams of the density of states of a ferromagnetic injector/detector and a non-magnetic metal/semiconductor. In (a) zero bias condition; (b) finite bias condition.

An obvious choice for spin injector is a ferromagnet (labeled F1 and F2), where an unequal distribution of spin-up and spin-down carriers exist at Fermi level under equilibrium condition. On the other hand, there is no such disparity in the non-magnetic metal or semiconductor (labeled P). Under application of an electric field, unequal amount spin-up and spin-down carriers enter **P** creating an imbalance. The concentration

of carriers of different spin orientation is represented mathematically by the electrochemical potential for that spin configuration. The imbalance is quantified by a split in this electrochemical potential represented by $\Delta\mu$. Here we would like to point out that spin injection in all-metals systems were realized much earlier compared to those in semiconductors. The conductivity mismatch between ferromagnet and semiconductor restricts the spin injection efficiencies to <0.1 %.[7] However a seminal proposal to incorporate tunnel contacts at the ferromagnet/semiconductor interface [8] was presented as a solution by Rashba et.al. to overcome this problem. The tunnel barriers provide high spin selectivity at the point of injection resulting in increased efficiency of spin injection into semiconductors. This proposition was later experimentally proven by several groups [9-11].Tunnel contacts can be broadly categorized into two:

a) insulating tunnel barrier contacts realized with materials like AlO_x or MgO.

b) Schottky tunnel contacts.

In this work we have used the latter as it is easier to realize by molecular beam epitaxial growth techniques. Ferromagnetic semi-metal MnAs has been the material of choice in all our experiments for the same reason. Properties of the ferromagnet will be discussed in detail in the subsequent chapters.

Detection of spin polarized carriers in a semiconductor can be done optically or electrically. Electrical detection of spin accumulation is done in the non-local geometry in order to eliminate spurious effects [10,11] that may lead to wrong conclusions. A schematic for measurement of non-local spin accumulation is shown in fig 1.4. The ferromagnet F1 is called the injector ferromagnet while ferromagnet F2 acts as the detector. The dimensions of F1 and F2 are carefully chosen such that there is a difference

in coercivity between these pads. This ensures distinctly different values at which the pad magnetization directions flips resulting in an unambiguious switching response in the spin accumulation characteristics. The distance between the pads are also carefully designed to be smaller than or equal to the spin diffusion length of the material (N) into which the spin polarized carriers are injected. Current is injected from F1 into N as shown by the arrow which indicates the direction of flow of the electrons. The spin accumulation is sensed by F2 which is positioned at a distance L from F1. The absence of any applied potential between F2 and N ensures that there is no charge current that can flow in this direction. However, spin information diffuses in all directions creating non-equilibrium distribution of spin polarized carriers around the injector pad F1. This is detected by F2 as a non-local voltage V. The advantage of this geometry is that it ensures the F2 terminal detects and measures the effect created only by the spin degree of freedom.

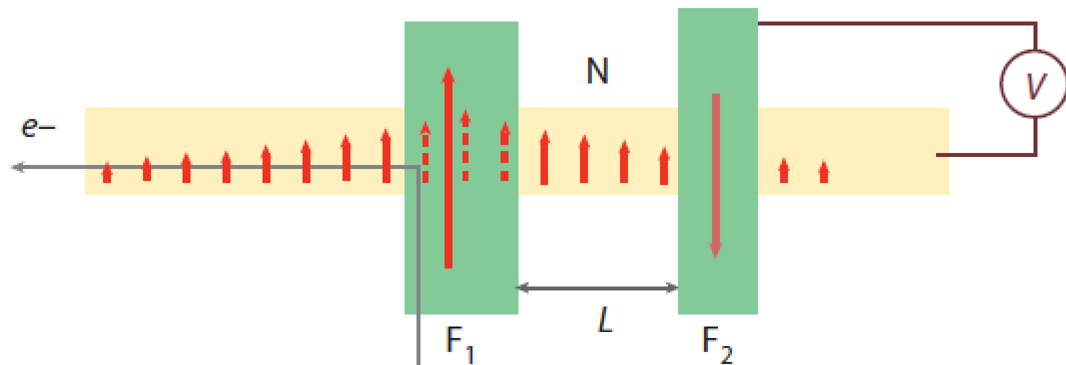

Fig. 1.4: Schematic shows the measurement geometry for non-local spin accumulation in metals or semiconductors.

Besides the non-local measurement of spin accumulation, spin injection and detection can also be measured by accurately detecting the voltage generated by the spin Hall

effect.[12] An arrangement for the measurement of spin Hall effect voltages is show in the fig. 1.5. In this geometry the current I is injected from the ferromagnet into the non-magnetic material N away from the Hall cross. A spin hall voltage V_{SH} is measured between the two hall probes. The spin Hall effect is a consequence of a seperation of the spin up and spin down carriers in N due to spin-orbit interaction [13] together with non-equilibrium spin accumulation near the ferromagnetic injector.

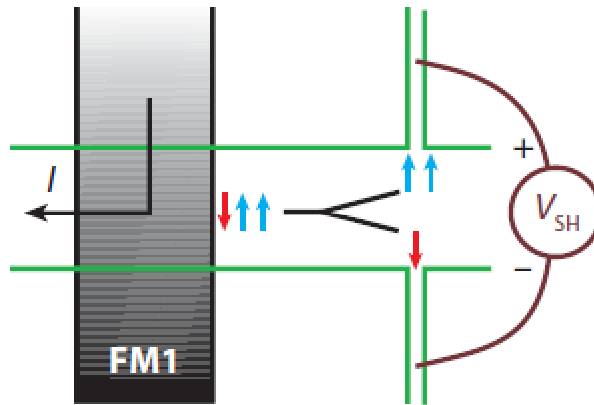

Fig 1.5: A schematic representation showing measuring non-local spin accumulation by detecting of spin Hall voltages using the lateral spin valve type geometry.

Another elegant way to measure and detect spin injection and spin accumulation electrically is by observing the Hanle effect. This effect refers to the dependence of the magnitude of the spin accumulation signal on magnetic field applied perpendicular to the injected spin. It has been observed that in presence of strong magnetic fields there are coherently decaying oscillations of non-local spin accumulation signal due to spin precession. The processes like spin diffusion, spin precession and spin relaxation are invoked in order to describe the density of spin polarization at a known distance from the spin injector. The geometry for the measurement of non-local Hanle effect signal is shown in fig. 1.6. The spin component of the signal can be estimated by the expression:[10]

$$s_x(x,t) = \frac{1}{\sqrt{4\pi Dt}} e^{-(x-v_d t)^2/4Dt} e^{-t/T_2} sin(\omega_0 t) \quad 1.1$$

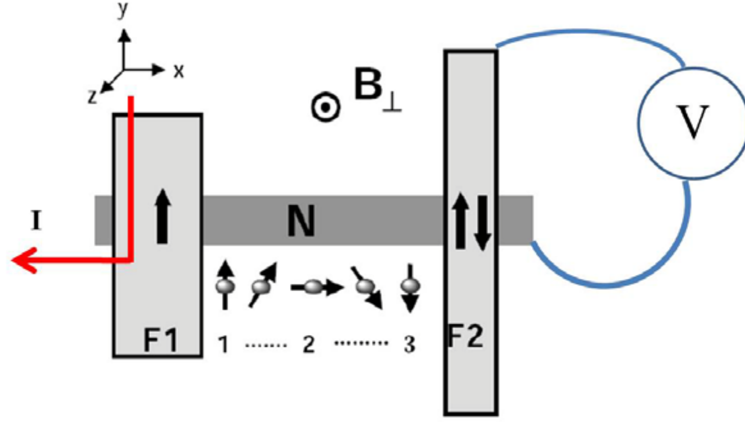

Fig. 1.6: Measurement geometry for estimating spin accumulation and precession using the lateral spin valve type geometry.

Optical detection of spin polarized carriers is similar to optical generation. The difference lies in the fact that circulary polarized photons are generated when the spin polarized electrons recombine with the holes in the active region of a light emitting diode (LED) or a laser. In light emitting diodes there is a direct relation between optical polarization to the spin polarization governed by the optical selection rules. The table 1.1

Transition	*Matrix element,* M_{if}	Δm_j	*Emission*	$\lvert M_{if}\rvert^2$
CB↑⇒HH↑	$\langle \frac{3}{2},+\frac{3}{2}\lvert\mu_x\rvert\frac{1}{2},+\frac{1}{2}\rangle$	-1	σ^+	$\frac{1}{2}\lvert\langle p_x\lvert\mu_x\rvert s\rangle\rvert^2$
CB↓⇒HH↓	$\langle \frac{3}{2},-\frac{3}{2}\lvert\mu_x\rvert\frac{1}{2},-\frac{1}{2}\rangle$	$+1$	σ^-	$\frac{1}{2}\lvert\langle p_x\lvert\mu_x\rvert s\rangle\rvert^2$
CB↑⇒LH↓	$\langle \frac{3}{2},-\frac{1}{2}\lvert\mu_x\rvert\frac{1}{2},+\frac{1}{2}\rangle$	$+1$	σ^-	$\frac{1}{6}\lvert\langle p_x\lvert\mu_x\rvert s\rangle\rvert^2$
CB↓⇒LH↑	$\langle \frac{3}{2},+\frac{1}{2}\lvert\mu_x\rvert\frac{1}{2},-\frac{1}{2}\rangle$	$+1$	σ^-	$\frac{1}{6}\lvert\langle p_x\lvert\mu_x\rvert s\rangle\rvert^2$

Table 1.1: Transition probability for allowed transitions and the polarization resulting from these transitions in case of a surface emitting device.

shows the possible interband transitions and the optical polarization in case of

semiconductors. [6] The transisiton rate is determined by the Fermi golden rule:

$$W_{if} = \frac{2\pi}{\hbar} \left| M_{if} \right|^2 g(h\nu) \qquad 1.2$$

Where M_{if} is the matrix element for transition and $g(h\nu)$ is the density of final states. The matrix element is determined from the initial and the final wavefunctions corresponding to the electronic states. It can be shown quantum mechanically that only those transitions are allowed where the matrix element has nonzero values. This theory also predicts that the conduction band (CB) - heavy hole (HH) transitions are three times more probable than its light hole (LH) counterparts. Thus in quantum confined direct bandgap semiconductor heterostructures it can be shown that the output circular polarization is a direct measure of the degree of spin polarization of the recombining carriers. Fig. 1.7 shows a schematic representation of this phenomenon.

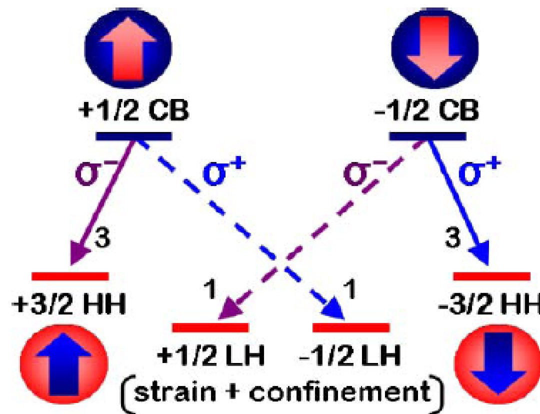

Fig 1.7: Allowed radiative interband transitions in case of quantum confined structures where the degenracy of the HH and LH is lifted by epitaxial strain and confinement.

1.2.2 Spin transport

The non-equilibrium distribution of spin polarized carriers injected into metals or semiconductors have a finite lifetime, which is also refered to as the spin relaxation time

of carriers in the given material. In order to attain the expected functionality it is imperative that the spin polarized carriers are detected before the spin information is lost due to spin relaxation. The design of the spin transport channel has to be done keeping in mind this very important parameter. There are four spin relaxation mechanisms for conduction electrons in metals and semiconductors. They are Elliot-Yafet (EY) [14], Dyakonov-Perel (DP) [15], Bir-Arhonov-Pikus (BAP) [16] and hyperfine interactions. The strength and importance of each mechanism is key to designing efficient metal as well as semiconductor based spintronic devices.

Elliot-Yafet mode of spin relaxation is caused by electron-phonon scattering or momentum scattering of spin polarized carriers off impurities in the bulk material [14,17]. A schematic representation of this scattering mode is shown in Fig.1.8.

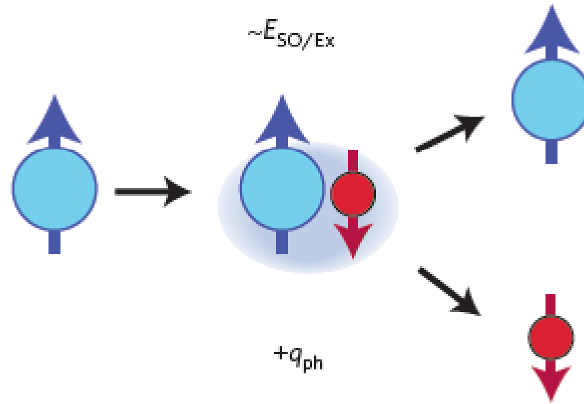

Fig. 1.8: Schematic representation of the electron-phonon mediated spin flip.

During this scattering process the intermediate state is an intermixed state with both spin up and spin down character arising from the spin orbit interaction. Expressions for spin lifetime or momentum scattering rates for this mechanism indicate that the EY is dominant in materials which have smaller bandgap and larger spin orbit coupling. This

spin relaxation mechanism completely describes carrier spin lifetime in metals and in semiconductors which are centrosymmetric (e.g. silicon). Here it is worth mentioning that although EY mechanism can explain the spin relaxation in most metals there are a few exceptions. Several polyvalent metals like aluminum, palladium etc show significant deviation from the values predicted by this model. This devation has been explained from spin-hot-spot theory [18] discussion of which is beyond the scope of this thesis.

The D'yakonov-Perel spin relaxation mechanism is operative in materials or heterostructures which do not have a center of symmetry.[15,19] In absence of symmetry the momentum states of the spin polarized carriers are not degenerate. This spin splitting can be represented as a intrinsic **k** dependent magnetic field (B(**k**)). This field forces the charge carriers to precess around this magnetic field with a frequency called the Larmor frequency, which is proportional to B(**k**). When this precessing electron is scattered by a phonon or a impurity center there is a sudden local change in this internal field. This

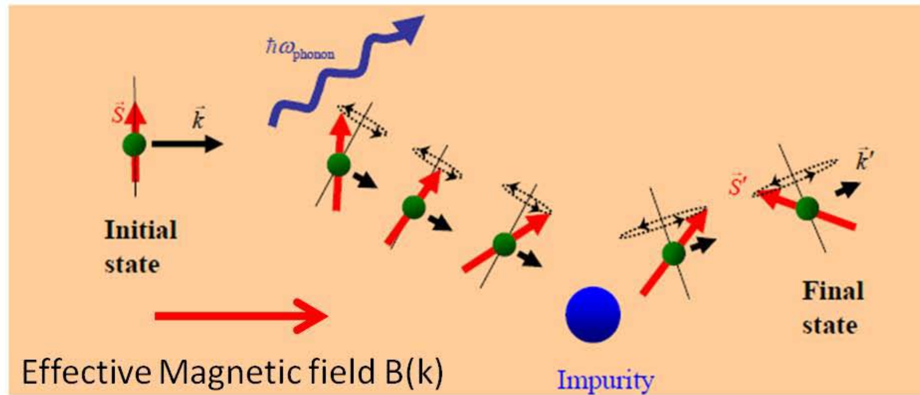

Fig. 1.9: Shows the origin of DP spin relaxation mechanism in non-centrosymmetric semiconductors

causes the precession axis to change randomly leading to decoherence of spin information. There are three principal sources of this built-in magnetic field. They are:

1. Inversion asymmetry intrinsic to crystal structure of the bulk constituents e.g.

zincblende in case of GaAs. This is known as bulk inversion asymmetry (BIA)

2. Inversion asymmetry arising from a certain arrangement of dissimilar materials such as in semiconductor heterojunctions. This is known as structural inversion asymmetry (SIA).
3. Asymmetry arising from the configuration of bonding at the interface between materials which have no common atoms. This is also known as native inversion asymmetry (NIA).

The Bir-Aronov-Pikus mechanism dominates in p-doped semiconductors due to the exchange interaction between electrons and holes.[16,17] The spin polarized electrons exchange spin information with unpolarized holes during an exchange interaction such that the total spin is preserved. However, due to strong intermixing of the heavy hole and the spin splitoff band, spin polarized holes tend to lose spin information very quickly due

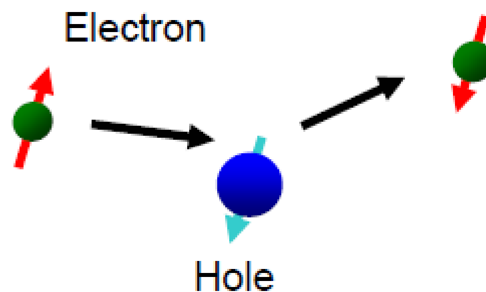

Fig. 1.10 : Shows the origin of BAP spin relaxation mechanism in degenerately p doped semiconductors.

to strong spin-orbit interaction. A schematic of the spin exchange is shown in Fig. 1.10. Thus, holes in a p-doped material act as a sink for electron spin polarization. The instant the spin polarized electrons transfer the spin information to this sink the information is lost almost instantaneously. [19]

Hyperfine interaction is an exchange interaction between the magnetic moment of

electrons and that of the nuclei. This interaction is too weak to manifest itself in metals or bulk semiconductors. For itinerant electrons this effect is negligible. This effect is observable for bound electrons whose wavefunction spreads over a large number of

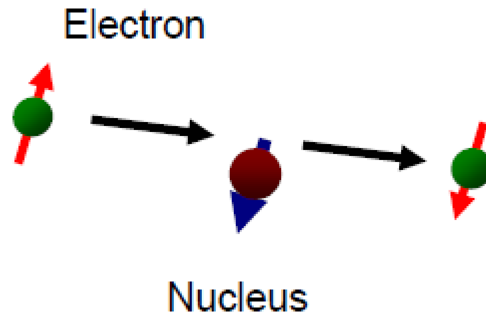

Fig. 1.11: Shows the nature of hyperfine interaction involving spin polarized electron and a spin polarized atomic nucleus.

nearby lattice centers.[20] The schematic in fig. 1.11 shows interaction that may occur between bound electrons and a nuclei which may lead to decoherence of spin polarization information.

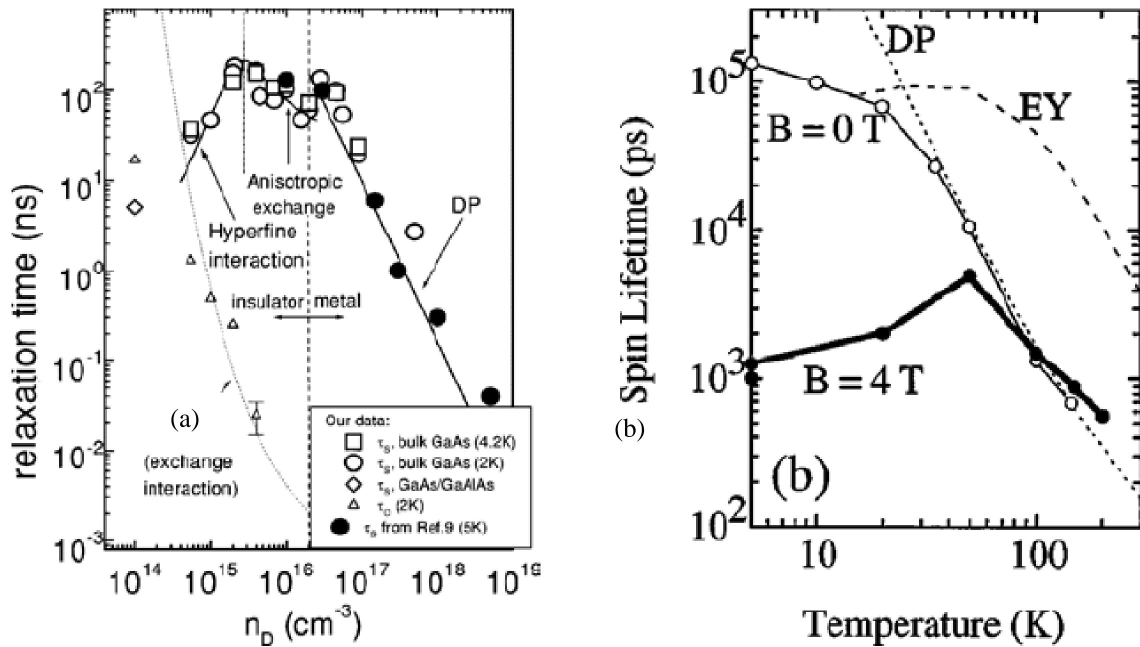

Fig1.12: Spin relaxation in n-type GaAs with (a) doping concentration[21] and; (b) temperature[22]

A detailed treatment of this mechanism is beyond the scope of this document.

The relative contribution of these four processes depend on the material system (metals or semiconductors) material quality (defect density, doping concentration) and experimental conditions (temperature, magnetic field, electrical or optical excitations as seen in Fig. 1.12). [21,22] However it is seen that EY mechanism dominates in metals and and for holes in semiconductors. BAP dominates for degenerately p-doped semiconductors and for the rest DP is the most dominant spin relaxation mechanism.

1.2.3 Spin orbit interaction and spin manipulation

The motion of electrons in an electric field can be represented by an equivalent magnetic field in the electrons frame of reference. The interaction of the electron with this equivalent magnetic field gives rise to spin-orbit interaction (SOI). We have discussed in the previous section that in noncentrosymmetric semiconductors (BIA) and/or semiconductor heterostructures lacking in symmetry (SIA) there is breaking of the double spin degeneracy of the electronic states. The spin orbit interaction that originates from the structure inversion asymmetry of the confining potential is usually referred to as the Rashba spin orbit coupling.[23] There is another mechanism, called the Dresselhaus SOI, which is due to bulk inversion asymmetry of the constituent material itself.[24]

The Rashba spin splitting observed in heterostructures which have structure inversion asymmetry can be expressed as a corresponding Hamiltonian where the precession vector is given by the following espression:[23,25]

$$\Omega_{\mathrm{k}} = 2\alpha_{\mathrm{BR}}(\mathbf{k} \times \mathbf{n}) \tag{1.2}$$

Here, α_{BR} is the parameter depending on spin orbit coupling and the asymmetry of the confining electrostatic potential in the given heterostructure. The most interesting aspect

of this phenonemon is the fact that the α_{BR} can be tuned electrostatically. Thus the spin precession in these heterostructures can be precisely controlled without presence of any external magnetic field. This interesting fact led to the proposal of the pioneering Datta Das spin transistor proposal (Fig 1.13). [26] The gate dependence of the α_{BR} parameter has

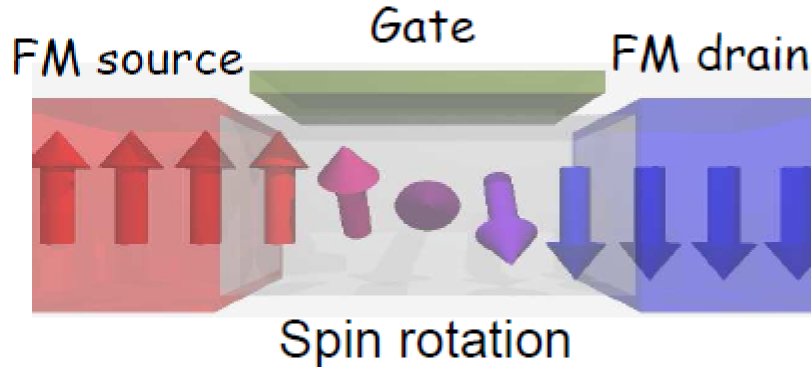

Fig 1.13: Schematic showing the working principle behind the ballistic spin transistor using Rashba spin-orbit couping.

been studied by numerous groups [27,28] and work is in progress in order to optimize this parameter in order to realize an efficient spin transistor.

The spin orbit interaction related effects in materials having BIA are referred to as Dresselhaus SOI. The intrinsic Larmor precession vector in the case of a bulk compound semiconductor is given by :[24]

$$\Omega_k = \alpha\hbar^2\left(2m_c^3E_g\right)^{-1/2}\kappa \qquad 1.3$$

Where κ is a parameter which is proportional to the cube of the lattice momentum vector. The constant α is a dimensionless parameter which indictes the strength of the spin orbit interaction.

In systems having contributions from both Rashba and Dresselhaus spin orbit interaction there are significant challenges in isolating the relative contribution from each

term.[28] It has been reported that in several systems [29] the interference of Dresselhaus and Rashba has led to the vanishing of the spin orbit interaction even though their individual contribution is large. Novel techniques based on spin galvanic effect [30] and photo galvanic effect [31] allows for experimental separation of these effects in quantum confined heterostructures.[32]

1.3 Semiconductor Spintronics

All metal spintronic devices have gained wide acceptance from the commercial stand point. The hard disk drives have already been realized for information storage based on an effect called the anisotropic magnetoresistance effect. The discovery of the giant magnetoresistance effect [4,5] allowed to increase the density of the information that can be stored in hard drives. In contrast to metals, semiconductors have larger spin relaxation times [21,22]. This advantage has stimulated a lot focussed research in the field of semiconductor spintronics. Besides this, the equilibrium carrier densities in semiconductors can be varied and since these densities are tunable, it is possible to realize devices whose electric properties can be tunable by application of a gate potential. In the next section different materials for spin injection and different categories of semiconductor based spintronic devices will be discussed in brief.

Electrical injection of spin polarized carriers in nonmagnetic semiconductors can be realized by direct injection from a source of spin polarized carriers.This can be achieved by replacing conventional metal contacts with magnetic materials. Magnetic materials have several intrinsic properties like saturation magnetic moment, Curie temperature and magneto-crystalline anisotropy. An ideal spin injector should have high Curie temperature to enable high temperature spin injection, large magnetic moment in order to

ensure high efficiency of spin injection and large magneto-crystalline anisotropy so that accidental demagnatization of the contact can be avoided in the presence of stray field in a different direction. There are three broad categories of spin injectors that are useful for spintronic research : (1) Dilute magnetic semiconductors as spin aligning contacts, (2) ferromagnetic metallic thin films and (3) half metallic or semimetallic ferromagnets. In the following sections we will briefly dicuss different important characteristics of all the three categories of spin injectors. The epitaxial growth and characterization of semimetallic MnAs thin film is studied in great detail in this work and can be found in chapter two.

1.3.1 Dilute magnetic materials

Semiconductors and insulators with ferromagetic properties were first observed in Cr-spinels and Eu-chalogenides. However these naturally occuring materials have low Curie temperature and are difficult to realize by epitaxial growth techniques. Later the discovery of ferromagnetism in Mn doped InAs and GaAs triggered a lot of research in the development of ferromagnetic semiconductors. [33] The Mn dopant atom replaces the Ga atom and hence acts as an acceptor introducing a hole. The Mn atom has an inherent magnetic moment. The interaction between the Mn d-states and the valence band p-states (p-d interaction) leads to the feromagnetic alignment of Mn-ions. Increasing the Mn concentration and correspondingly the hole concentration leads to a higher Curie temperature. However the incorporation of higher Mn atoms in the GaAs lattice is thermodynamically unstable. Increase in the growth temperatures of Mn doped GaAs leads to the formation of MnAs clusters instead of a homogeneous film. Low growth temperatures lead to the formation of a large concentration of As-antisites[34]

which partly removes holes introduced by substitutional Mn. This drawback has severely affected the application of these materials as spin injectors for realizing realizing high temperature spintronic devices. Mn doped II-VI materials (ZnMnSe) have sp-d interaction leading to a large g-factor. Thus, the presence of relatively small magnetic fields can induce large Zeeman splitting. Hence these materials, have also been used as spin aligners in order to realize injection of large spin polarization in semiconductors but with limited practical applications.

1.3.2 Ferromagnetic metal spin injectors

Ferromagnetic materials like iron (Fe), nickel (Ni), cobalt (Co) and their alloys have high Curie temperature and large magnetic moments hence are suitable candidates for spin injectors. Partially filled d-shells which are split due to exchange interaction is the cause of ferromagnetism in these materials. However, the conduction electrons in these materials are not fully spin polarized. This is because of the simultaneous presence of 4s

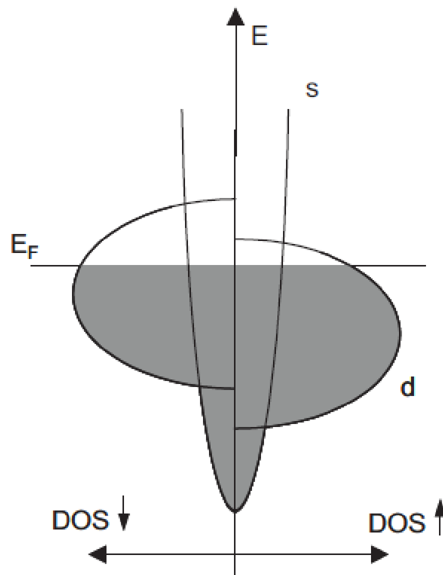

Fig. 1.14: The density of states for a typical 3d-ferromagnet. The partially filled d-bands are split by the exchange interaction.

electrons at the Fermi level. The schematic shown in fig. 1.14 shows the density of states of a typical 3d ferromagnet. Ferromagnetic contacts have been widely used to realize spin based electronic and optoelectronic devices.[35-39] Even room temperature operation of spintronic devices have been reported with these materials.[39] However one has to be extremely careful in order to ensure spin injection into the semiconductor and to determine injection efficiency.

1.3.3 Half metallic metal spin injectors

Electrons that have only one kind of spin contribute to its metallic property in half metallic metals. The other set do not contribute to conduction as they lie above the Fermi level. There are no elemental metals that have a half-metal behaviour. The basic difference between half metals and semi-metals is that the former is definitely composed of ferromagnetic material but the latter is not. There are three different types of half metals. Fig. 1.15 shows detailed classifications of half metallic metals with examples.[40] These materials have 100 % spin polarization unlike the naturally occring metals and tend to have high Curie tempreatures. Hence, theoretically these materials are the ideal candidates for spin injection and detection. Heusler alloys are a special category of halfmetallic alloys which have crystal structures and lattice parameters similar to zinc-

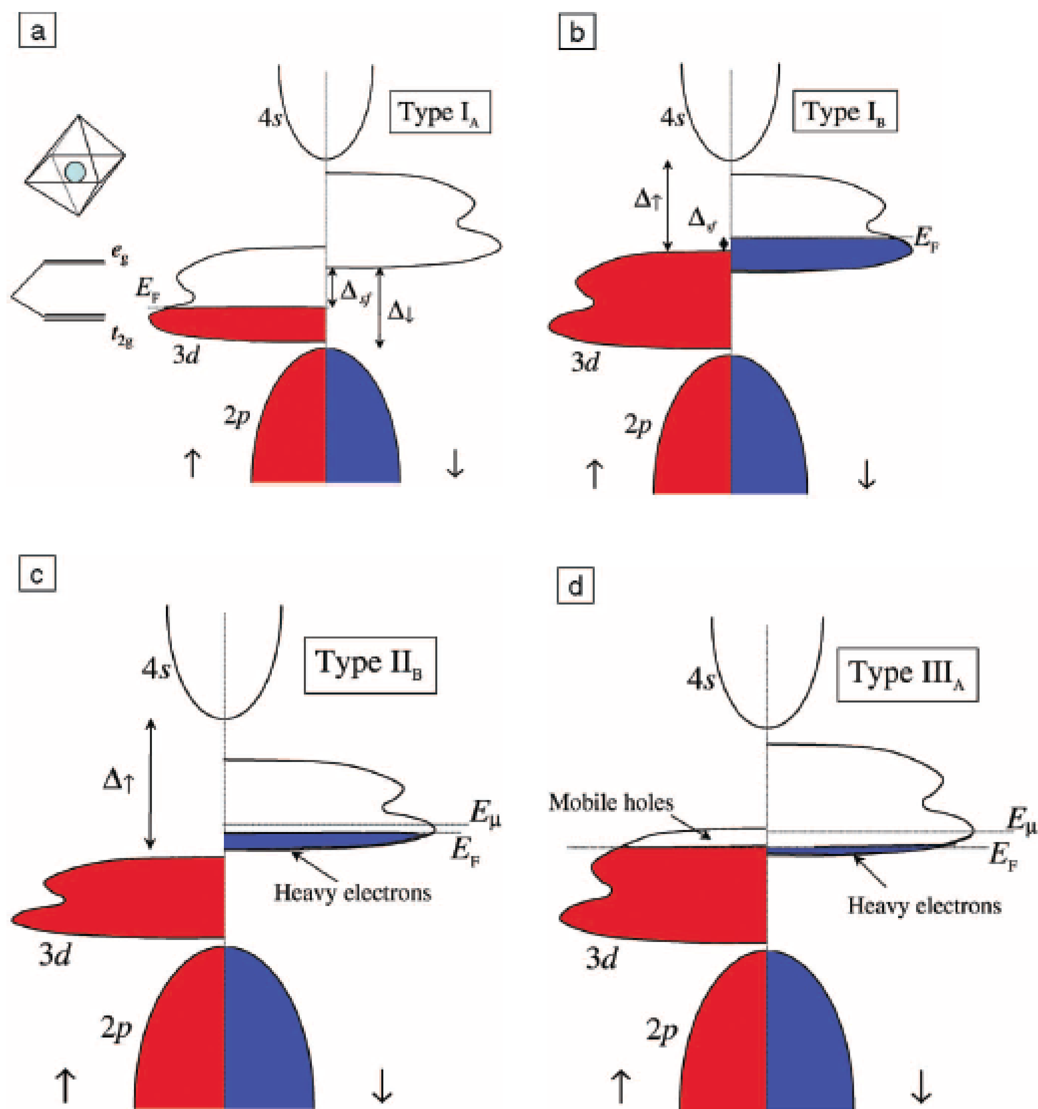

Fig. 1.15: Classification of half-metals. The diagrams show schematic densities of states for spin-up (red) and spin-down (blue) electrons. E_F is the Fermi energy, E_μ is the mobility edge energy, Δ is the gap for one electron spin, and Δ_{sf} is the spin-flip gap. (a) Type IA (e.g., CrO_2) and (b) Type IB (e.g., Sr_2FeMoO_6) half-metals have only aor belectrons at the Fermi level, with a gap for the other spin direction. (c) Type II half-metals are similar to Type I, but have narrow bands where the electrons are localized, and conduction is by hopping; shown here is a Type IIB half-metal (e.g., Fe_3O_4). (d) Type III half-metals have a mixture of delocalized electrons with one spin direction and localized electrons with the other; shown here is a Type IIIA half-metal (e.g., $La_{0.7}Sr_{0.3}MnO_3$). The illustration on the left in (a) shows a cation in octahedral oxygen coordination and the splitting of the one-electron energy levels into t2g and eg states. In a solid, these states broaden to form the 3d bands.[40]

blende III-V semiconductors. These alloys can be further subdivided into two types. Full Heusler alloys of the form X_2YZ or half Heusler alloys. Fig. 1.16 shows a schematic

repersentation of the crystal structure of the different forms of Heusler alloys. [41]

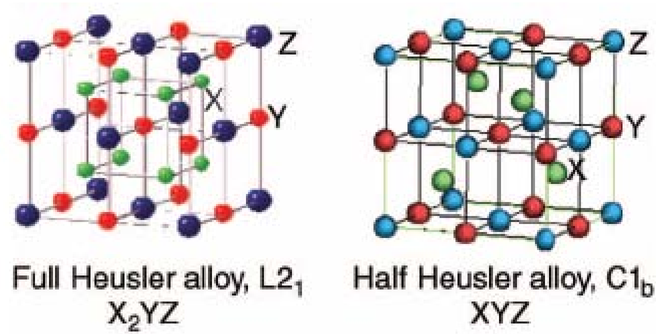

Fig.1.16: Crystal structures of full Heusler alloys, half Heusler alloys

Several such alloys have high Curie temperatures but the major challenge lies in controlling the composition, atomic ordering and defects both in the film and at the interface with semiconductors.

1.3.4 Semiconductor spintronic devices

Semiconductor based spintronic devices can be broadly classified into 3 categories. These are: 1. Spin based optoelectronic devices, 2. Lateral spin based electronic devices and 3. Vertical spin based devices. The first proposed spin-electronic device that created

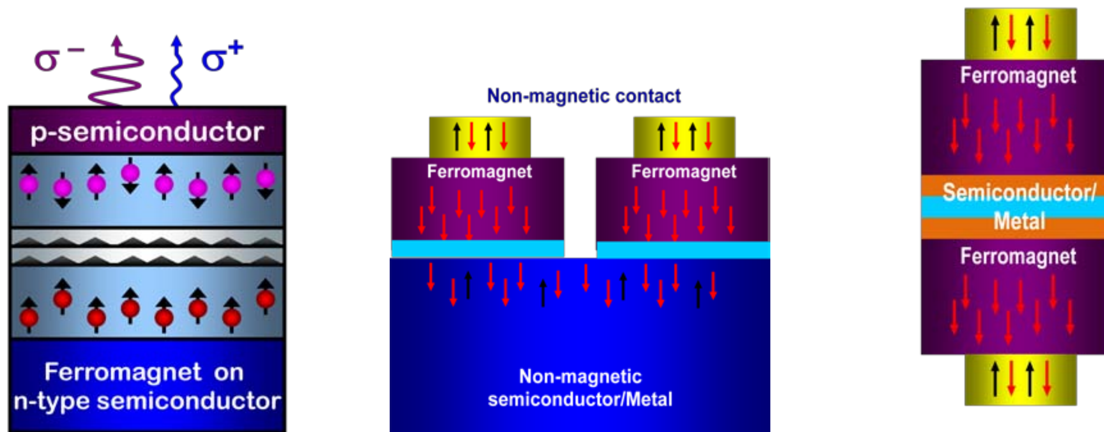

Fig. 1.17: Schematic repesentation of the different types of semiconductor based spin polarized devices realized to date.(a) Spin polarized optoelectronic device; (b) Lateral spin based electrical device and;(c) vertical spin based electrical device.

a lot of interest was the electronic analog of an electro-optic modulator commonly known

as the Datta-Das transistor.[26] Other than the spin transistor several different proposed devices include reconfigurable spin logic [42], room temperature spin-transference device [43], electron spin resonance transistor [44], a 2d channel spin valve controlled by ferromagnetic gates [45], spin capacitor [46], spin Esaki diodes [47], spin lasers [48], unipolar magnetic diodes [49], spin light-emitting diodes [50], field-effect magnetic switch [51], or spinflip or single electron spin-valve transistors [52]. This thesis primarily deals with the design and realization of lateral spin transistor, high temperature vertical spin valves and spin lasers operating near room temperature.

1.4 Thesis Organization

The research described in this thesis is focused on realizing high temperature spin based electronic and optoelectronic devices. The spin based electrical devices can be promising alternatives to present day CMOS technology. The power dissipation in conventional CMOS circuit elements can be completely described by equilibrium statistical mechanics. It can be shown that for non-equilibrium systems the energy dissipation can be much lower. A complete treatment of non-equilibrium systems are done by invoking the dynamic equations of motion e.g. the Bloch equations and can be found elsewhere. [19] Spin of an electron can be used as a state variable in such a non-equilibrium system, as spin relaxation times are much larger than carrier relaxation times and/or the switching times in circuits. The ratio of the minimum energy dissipated in a switching spintronic circuit to the conventional charge based circuit is given by: [53]

$$\frac{\Delta E_{spin}}{\Delta E_{CMOS}} = \frac{tanh(1)}{log2} \times \frac{\tau_{sw}}{\tau_C} \approx 10^{-4} \tag{1.4}$$

where, τ_{sw} and τ_C are the spin switch times and the clocking times respectively. These

numerical estimates are subject to the condition that spin relaxation times (τ_{SR}) are much larger than the spin switch times. Hence spintronic devices have a distinct advantage over its charge based counterpart so far as power dissipation is concerned. The novel spin-polarized coherent light sources, with lower input power requirement and predictable output polarization can find numerous applications in optical communication systems and biomedical research.

The most critical component of any spintronic device is its spin injector contact. Chapter 2 describes a detailed study on the heteroepitaxial growth and characterization of ferromagnetic MnAs as efficient spin injectors into III-V based semiconductors including GaAs, InP and other ternaries lattice matched to InP. The growth dynamics of such highly lattice mismatched materials are studied by atomic force microscopy and X-ray diffraction techniques. The electrical characterization of the heteroepitaxial layers are also done by fabricating conventional lateral spin valve devices of different channel lengths. A peak magnetoresistance of ~1.2 % is measured in conventional spin valves at 10 K with a channel length of 500 nm. The calculated spin diffusion length at 10 K is 1.55 μm and spin injection efficiency below the injector contact is found to be 28.8 %.

In Chapter 3 we discuss growth, fabrication and characterization of devices where we use this optimized spin injector contact in order to demonstrate modulation of magnetoresistance in the absence of an external magnetic field. The device used in the study is an $InAs/In_{0.53}Ga_{0.47}As/In_{0.52}Al_{0.48}As$ quantum well lateral spin valve with a gate electrode placed alongside the MnAs polarizer contact and outside the channel is realized for this study. The electron mobility at room temperature in the InAs channel is ~5500 cm^2/V-s. The magnetoresistance changes from 0.14% to 4% at 10 K in this device when

the spin transport is in the direction of magnetization of the polarizer and analyzer contacts. We also discuss several control experiments performed in order to ensure the effect is primarily due to spin injection manipulation and detection.

High temperature operation of spin based electronic devices can be achieved by reducing the electron transport length. In Chapter 4 we discuss the characteristics of high temperature MnAs/GaAs based vertical spin valves. We point out the challenges of epitaxially growing relatively defect free, device quality GaAs:Mn on top of MnAs which are characterized by transmission electron microscopy as well as X-ray diffraction measurements. These devices show a peak magnetoresistance of ~40 % measured at 10 K and ~1 % at room temperature. The high values of magnetoresistance are explained by invoking valence band electron tunneling through degenerately p-doped semiconductor. A model for the temperature dependence in these devices is also discussed at length.

Chapter 5 and 6 discusses about the realization of InAs/GaAs quantum dot based high temperature (working at 200 K) spin polarized vertical cavity surface emitting laser and its characteristics under DC bias. Peak degree of output circular polarization of ~14 % is measured at 200K with a maximum threshold reduction of ~5 % under continuous wave (CW) current excitation. The operation of these VCSELs is modeled by solving the spin dependent carrier-photon rate equations. The importance of incorporating spin drift-diffusion model together with the rate equation is highlighted in chapter 6. Bias dependence of output circular polarization with a modulation index of 0.6 is theoretically calculated and experimentally determined.

In chapter 7 we describe a novel theoretical prediction and then the experimental realization of a high degree of output circular polarization from a spin laser in spite of a

low degree of carrier spin polarization in the active region. We discuss analytical as well as numerical techniques to model transient and high frequency response of spin lasers. The growth, fabrication and characterization of an electrically injected InAs/GaAs quantum dot spin-VCSELs with a mesa diameter of 10 μm operating at 230 K is presented. A maximum degree of circular polarization of 55 % is measured in these devices under pulsed biased condition. A peak threshold reduction on the other hand is ~ 5% which is indicative of a low degree of spin polarization in the active region. Finally we present a detailed discussion about agreement between the experimental data with those calculated from the model.

In Chapter 8, the main contributions of this research are summarized and several suggestions for future developments in three terminal spin-polarized electrical devices, and room temperature edge emitting lasers are made.

CHAPTER II

Epitaxial Growth and Characterization of Ferromagnetic MnAs

2.1 Introduction

Though bulk MnAs was first studied by Heusler [54] in 1904, the ferromagnetic properties of this semimetal were first reported in 1911 by Hilpert *et.al*. with an observed Curie temperature of ~40 ^{o}C. [55,56] X-ray diffraction measurements on polycrystalline MnAs revealed that an abrupt change in the lattice constant occurs just near this temperature. It was later reported that a second phase transition proceeds at ~130 ^{o}C, this time without any volume change. Magnetic susceptibility measurements confirmed that the material is paramagnetic for temperatures above 40°C. Single crystal XRD measurements revealed that this material undergoes a change in the crystallographic structure, from hexagonal NiAs type (α-MnAs) to the orthorhombic MnP type (β-MnAs), at the first order phase transition point. [57] This distortion was found to disappear for temperatures above 126°C (γ-MnAs). A ball and stick diagram shows the crystal structure α-MnAs where the dimension of the *a* and *c* axis are 5.7 Å and 3.7 Å respectively. The table 2.1 shows a detailed set of parameters used for generating the ball and stick diagram.[58]

With emerging interest in spintronics, epitaxial growth of ferromagnetic spin injectors on semiconductor substrates have become a key towards the realization of spin based logic devices and large scale circuits [35,42]. The growth of MnAs as a

ferromagnetic spin injector by heteroepitaxy on (001)GaAs and (001)InP substrates is

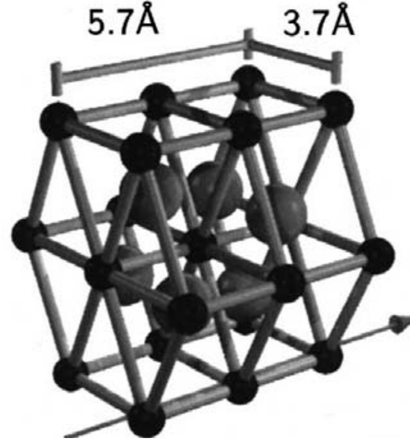

Fig. 2.1: A ball and stick diagram showing the arrangement of atoms together with the lattice constants for ferromagnetic MnAs

basic vectors of the Bravais lattice	$\boldsymbol{a}_1 = a\left(\frac{1}{2}, \frac{\sqrt{3}}{2}, 0\right)$
	$\boldsymbol{a}_2 = a\left(-\frac{1}{2}, \frac{\sqrt{3}}{2}, 0\right)$
	$\boldsymbol{a}_3 = c(0, 0, 1)$
bacis vectors of the reciprocal lattice	$\boldsymbol{b}_1 = \left(\frac{2\pi}{a}\right)\left(1, -\frac{\sqrt{3}}{3}, 0\right)$
	$\boldsymbol{b}_2 = \left(\frac{2\pi}{a}\right)\left(-1, -\frac{\sqrt{3}}{3}, 0\right)$
	$\boldsymbol{b}_3 = \left(\frac{2\pi}{c}\right)(0, 0, 1)$
atomic positions	As: 0; $\frac{1}{3}(\boldsymbol{a}_1 + \boldsymbol{a}_2) + \frac{1}{2}\boldsymbol{a}_3$
	Mn: $\frac{2}{3}(\boldsymbol{a}_1 + \boldsymbol{a}_2) + \frac{1}{4}\boldsymbol{a}_3$;
	$\frac{2}{3}(\boldsymbol{a}_1 + \boldsymbol{a}_2) + \frac{3}{4}\boldsymbol{a}_3$
lattice constants	$a = 7.7037$ at. units
	$c/a = 1.532$
sphere radii	$R_{\mathrm{Mn}} = 2.2675$ at. units
	$R_{\mathrm{As}} = 2.6085$ at. units

Table 2.1: Basic lattice parameters of bulk ferromagnetic MnAs.[58]

challenging due to the remarkably large geometrical and anisotropic thermal mismatch between these materials. In the current work MnAs has been used extensively as a spin

injector in realizing several spin polarized electronic and optoelectronic devices because of its high Curie temperature and formation of relatively defect free interfaces with III-V semiconductors with no intermediate magnetically dead layers. In the next few sections we will discuss about the epitaxial growth and characterization of MnAs thin films on InP based lattice matched semiconductors.

2.2 Epitaxially grown MnAs thin films on InP

Epitaxial layers of MnAs were grown directly on Sn-doped InP(001) substrates and on Si-doped $In_{0.53}Ga_{0.47}As$ lattice matched to InP using solid source MBE. The lattice mismatch between the *a* axis of MnAs and InP is 36.5%. For growth on InP, the substrate temperature was first raised to 535 ^{o}C with an arsenic (As_4) beam equivalent pressure (BEP) of 6.6×10^{-6} torr to remove surface oxides. A typical RHEED pattern

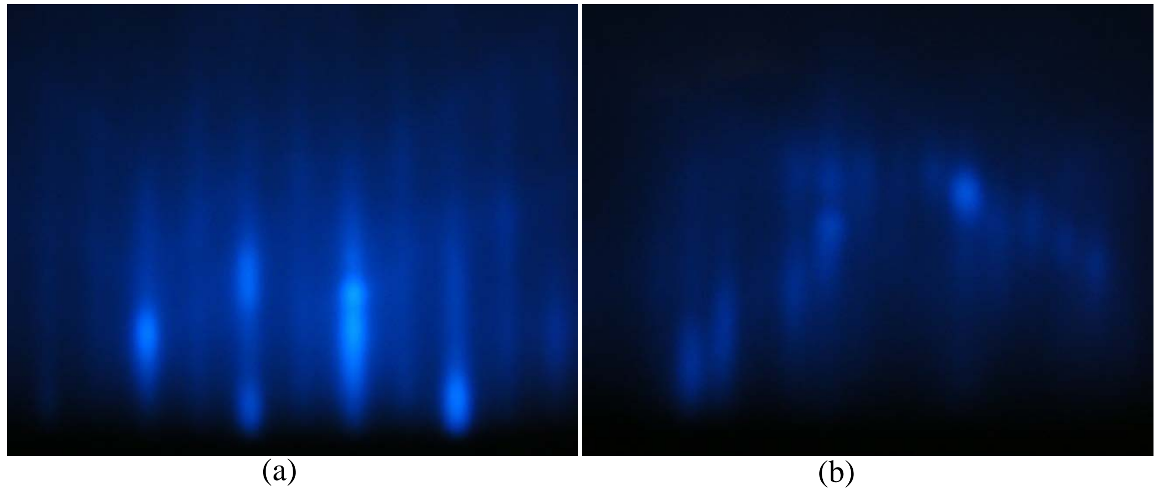

(a) (b)

Fig.2.2: RHEED pattern of a c(2×4)-InP(001) surface taken along the (a) [110] and (b) [010] azimuths.

for arsenic rich surface reconstruction of InP at 535 ^{o}C is shown in fig 2.2.

The temperature was then reduced to 200 ^{o}C. A few monolayers of MnAs were

grown in the nucleation phase with a As/Mn BEP ratio of 90. The substrate temperature was then raised to 250 ^{o}C and the As/Mn flux ratio was reduced to 50 to ensure a higher growth rate. Fig 2.3 shows RHEED reconstruction patterns observed just after the nucleation phase before the temperature was raised to 250°C. It is seen that patterns are spotty and diffuse (Fig. 2.3 (a,b)). This indicates that the surface roughness is significant during this phase. This was later verified by atomic force microscopy measurements carried out on the 5 nm thick MnAs layer on InP. As the growth progresses the patterns became streakier and a clear 1 x1 pattern was observed for a 35 nm MnAs thin film (Fig. 2.3 (c,d)).

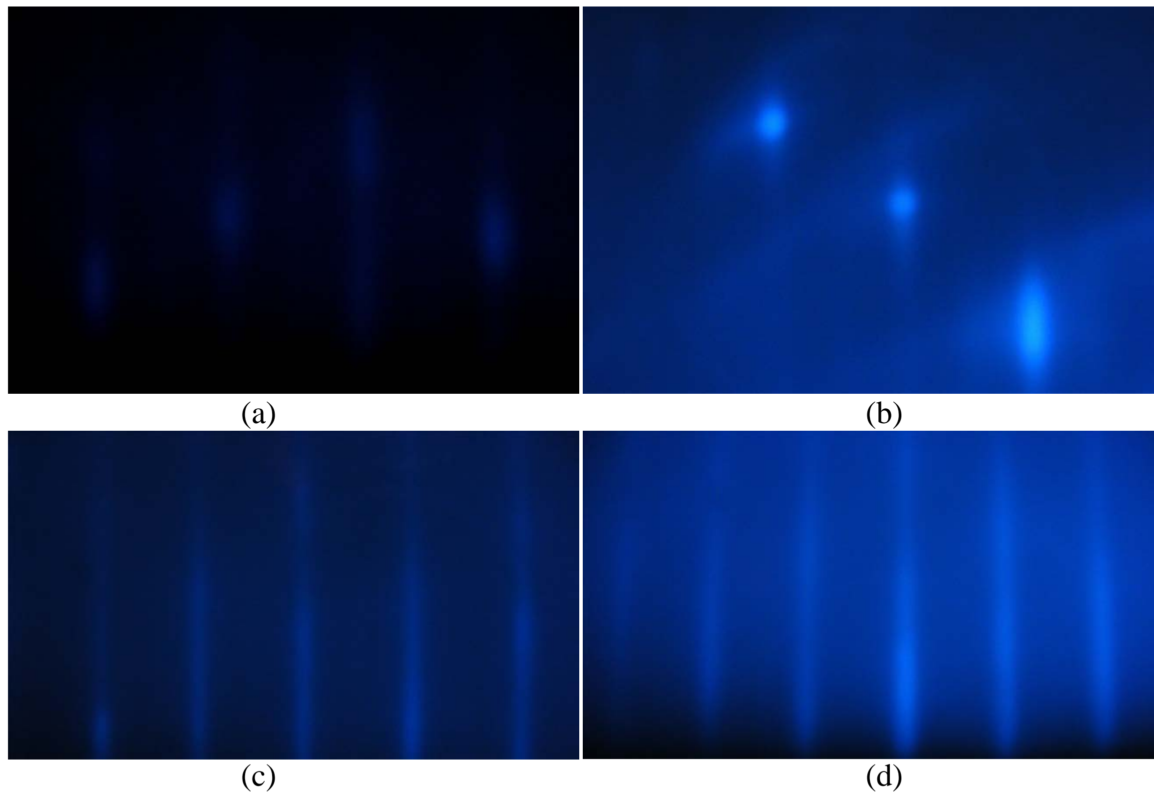

(a) (b) (c) (d)

Fig. 2.3: RHEED pattern of a type-B MnAs film taken along the (a) [110] and (b) [1$\bar{1}$0]azimuths in the presence of an As4 flux during the nucleation phase. RHEED pattern taken along the (c) [110] and (d) [1$\bar{1}$0] azimuths before the annealing the sample.

Finally, a post growth in situ anneal was done at 360 ^{o}C for 2 minutes under an arsenic

BEP of 7×10^{-6} Torr, to improve the surface morphology.

In-situ RHEED patterns observed during the anneal phase of the MnAs films is shown in fig. 2.4. A (1× 1) surface reconstruction observed in the case of growth on (001)InP abruptly changed to a (4×1) reconstruction, upon annealing under conditions mentioned above. The change in reconstruction was not reversible on lowering the anneal temperature. In contrast, the RHEED patterns in the case of MnAs grown on $In_{0.53}Ga_{0.47}As$ show a (1× 1) reconstruction, with no observable change after annealing.

Fig. 2.4: RHEED pattern of a type-B MnAs film taken along the $[1\bar{1}0]$ azimuths in the presence of an As_4 flux during the anneal phase.

The surface reconstruction of InP consists of mixed In-P dimers while $In_{0.53}Ga_{0.47}As$ consists of dimers and missing dimers along the symmetry directions, resulting is a very different template for growth initiation. Hence there is significant difference in the surface phase diagram of MnAs [59] grown on these different materials under the same conditions of growth. The surface morphology of these as-grown and annealed MnAs layers were then investigated by atomic force microscopy.

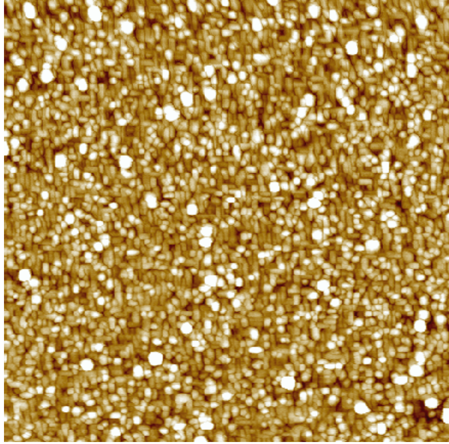

(a)

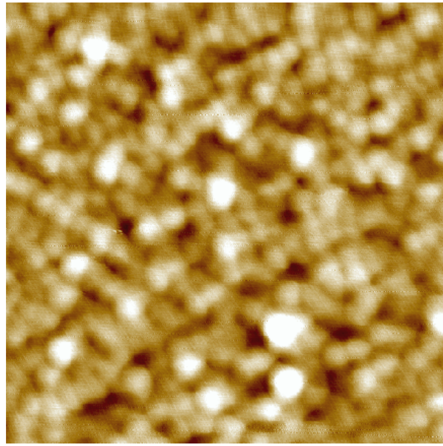

(b)

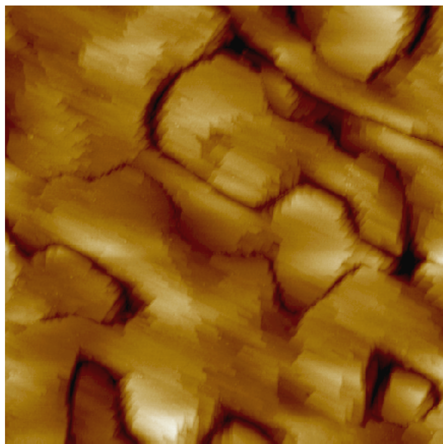

(c)

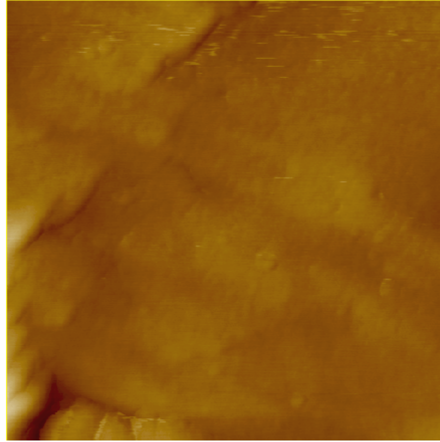

(d)

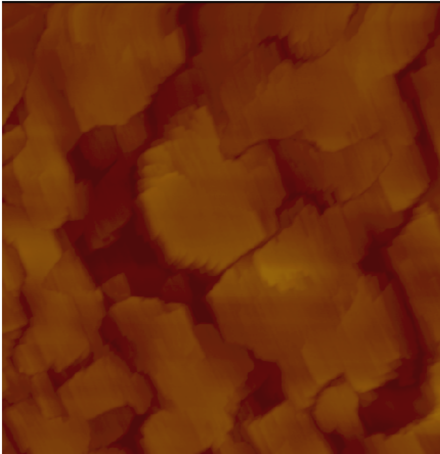

(e)

(f)

Figure 2.5: Roughness and surface morphology of MnAs film (2.5 μm × 2.5 μm) (left) and (500 nm ×

500 nm) (right): (a) after 5 nm of growth on (001)InP. Micrographs shows an area of 2.5 μm × 2.5 μm; (b) after 5 nm of growth on (001)InP. Micrographs show an area of 500 nm × 500 nm; (c) after annealing a 35 nm film on (001)InP. Micrographs show an area of 2.5 μm × 2.5 μm; (d) after annealing a 35 nm film on (001)InP. Micrographs show an area of 500 nm × 500 nm; (e) after annealing a 35 nm film on $In_{0.53}Ga_{0.47}As$ lattice matched to (001)InP. Micrographs show an area of 2.5 μm × 2.5 μm; (f) after annealing a 35 nm film on $In_{0.53}Ga_{0.47}As$ lattice matched to (001)InP. Micrographs show an area of 500 nm × 500 nm.

The results are depicted in Fig. 2.5 for 2.5 μm × 2.5 μm and 500 nm × 500 nm surface areas. The images from a 5-nm thick as-grown layer of MnAs on (001) InP (Fig. 2.5(a,b)) indicate that growth is in the form of 3D islands (Volmer-Weber or Stranski-Krastanov growth modes). As the layer thickness increases these islands coalesce. The root mean square (rms) value of surface roughness of a 35 nm MnAs epitaxial layer on InP was found to be 19 Å over a lateral distance of 2.5 μm. The surface morphology of this layer improved considerably after annealing, as shown in Fig. 2.5(c,d). The small and separated islands coalesce and form larger ones with rms value of surface roughness of 7 Å over a lateral distance of 0.5 μm. This occurs in spite of the fact that the annealing step creates a layer with a (4 ×1) reconstruction. The reduction of surface roughness is attributed to the increase in the in-plane grain size of the MnAs layer upon annealing and increasing monolayer thickness.[60] X-ray diffraction measurements done on MnAs films indicate that the approximate grain size for a 35 nm film is ~30 nm. AFM measurements were also done on as-grown and annealed MnAs layers on $In_{0.53}Ga_{0.47}As$ lattice matched to InP and the rms value of surface roughness was found to be 22 Å for a 35 nm thick layer (Fig. 2.5(e,f)). The surface morphology of the film was not much different from that of MnAs grown on InP.

2.3. Magnetic properties and characterization

The in-plane magnetic properties of 35 nm MnAs epitaxial layers grown on InP and lattice-matched $In_{0.53}Ga_{0.47}As$ were studied by longitudinal magneto-optic Kerr effect (MOKE) measurements. Results indicate that in both cases the $[\bar{1}\bar{1}20]$ MnAs orientation, which is the easy axis of magnetization, is parallel to $[\bar{1}10]$ InP. This

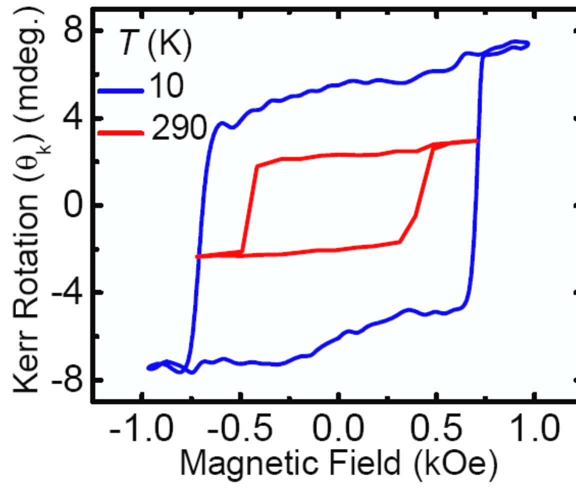

(a)

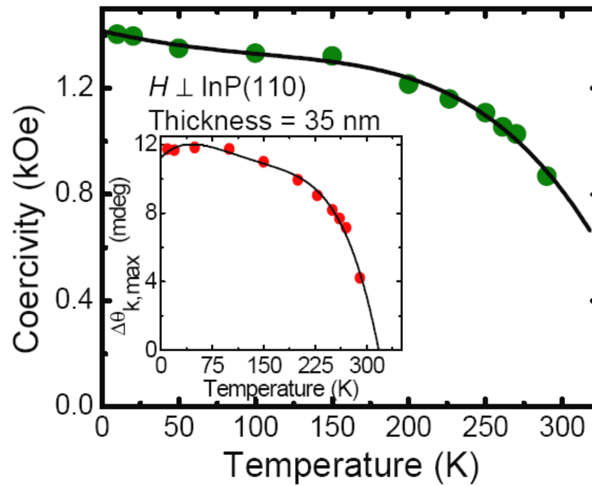

(b)

Fig. 2.6 (a) Kerr rotation of epitaxially grown and annealed type-B MnAs on InP(001) measured at 10 K and 290 K with applied magnetic field in the $[\bar{1}10]$ direction; (b) coercivity measured at different temperatures for 35 nm epitaxially grown layer. Inset shows the variation in $\Delta\theta_K$ as a function of temperature. The solid lines are drawn as a guide for the eye.

direction of magnetization is the same as in type-B MnAs [61]. The Kerr rotation θ_k is 6.2 milli-degrees at 10 K (Fig. 2.6(a)) but decreases to 2 milli-degrees at 290 K. The lack of squareness of the Kerr rotation vs applied magnetic field curves at the point where the direction of magnetization switches can be attributed to the coexistence of two planes, $(\bar{1}102)$ and $(\bar{1}101)$, for epitaxially grown type-B MnAs [61]. The coercivity (H_C) of the film decreases with temperature as shown in Fig. 2.2(b). The change in the value of H_C over the temperature range of 10 – 300 K is 39%. Magnetic hysteresis is not observed in the InP[110] direction, which indicates that the MnAs layer has in-plane uniaxial magnetic anisotropy. The inset to Fig. 2.2(b) shows the temperature dependence of the differential Kerr rotation, $\Delta\theta_k$. Here $\Delta\theta_k = \theta_{k,max} - \theta_{k,min}$ and $\theta_{k,max}$ and $\theta_{k,min}$ are respectively, the maximum and minimum Kerr rotation angles measured at a particular temperature. The Curie temperature of the MnAs layer, estimated from the Kerr rotation data and the Curie-Wiess law, is 315 K which is comparable to that measured for films grown on (001)GaAs [62]. The Kerr rotation characteristics and Curie temperature of MnAs grown on lattice-matched $In_{0.53}Ga_{0.47}As$ were identical to the ones grown on (001)InP.

At equilibrium, in the presence of an external magnetic field H, the orientation of

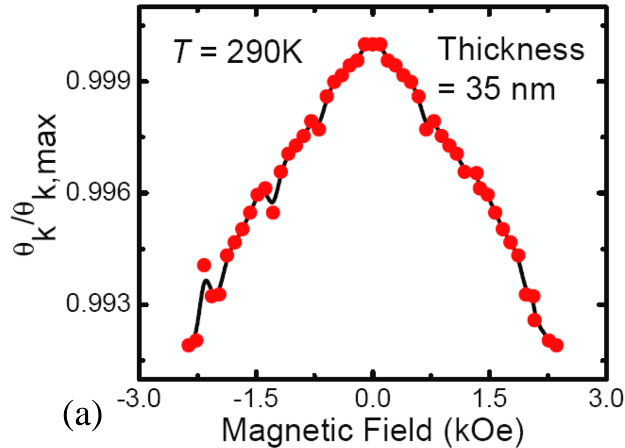

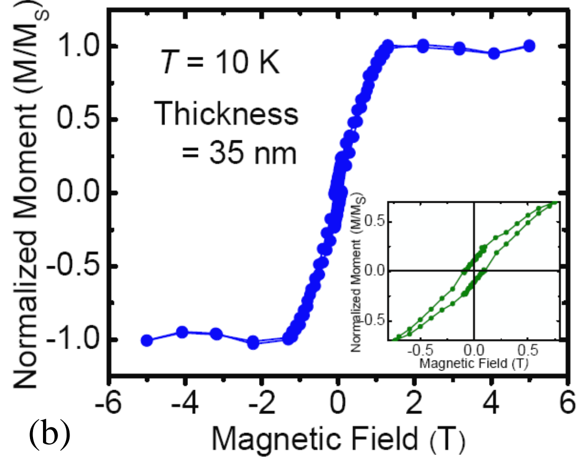

Figure 2.7: (a) Normalized values of the longitudinal Kerr magneto-optic effect versus in-plane applied field *H* for the MnAs sample at room temperature; (b) Magnetic hysteresis measured for a 35 nm MnAs/InP(001) layer recorded at 10 K in the out-of-plane direction using a SQUID magnetometer. Inset shows variation of the normalized moment at low applied fields, indicating small remanence and coercivity.

film magnetization **M,** is such that the sum of external field energy, demagnetizing energy and anisotropy energy is minimized. The uniaxial magnetocrystalline anisotropy constants K_{u1} and K_{u2} [63,64] associated with the anisotropy energy are calculated from this energy minimization criteria for different orientations of **M**. Figure 2.7(a) shows the variation of the Kerr magneto-optic signal with increasing H applied along the in-plane hard axis of magnetization for a 35 nm MnAs film on (001)InP. Here the normalized Kerr rotation $\theta_k / \theta_{k,max}$ is a direct measure of the orientation of **M**.

The values of K_{u1} and K_{u2} calculated at room temperature, are 2.747×10^{6} erg/cc and 7.086×10^{6} erg/cc, respectively. Similar values were also obtained for MnAs on lattice matched $In_{0.53}Ga_{0.47}As$. It is seen that the anisotropy constants are lower than that for bulk MnAs [65]. The magneto-crystalline anisotropy arises due to spin orbit coupling with contributions from the heterointerface and the crystalline structure of the thin

film. The presence of dangling bonds and stress at the semiconductor-ferromagnet interface results in reduced orbital symmetries which may contribute to the lower values of the anisotropy constants [66] compared to bulk. Figure 2.7(b) shows the out-of-plane magnetization characteristics for a 35 nm MnAs film grown on InP, measured using a SQUID magnetometer and recorded at 10 K. The saturation magnetic field (M_S) was measured to be at 1.2 T. The inset to Fig. 2.7(b) shows that the sample has a small remanence ($0.11\times M_S$) with a coercivity of 1600 Oe. Similar out-of-plane remanence was also observed for epitaxially grown MnAs films on $In_{0.53}Ga_{0.47}As$ and GaAs [67] .

2.4. Electrical injection and detection of spin in $In_{0.52}Al_{0.48}As$

In order to electrically characterize the quality of the MnAs thin film spin-valve heterostructures were grown by molecular-beam epitaxy on semi-insulating InP(001) substrates. A 500 nm Si-doped n-$In_{0.52}Al_{0.48}As$ channel layer was grown at 535°C, followed by a 30 nm graded doping n^+- $In_{0.52}Al_{0.48}As$ contact layer grown at the same temperature, after which the substrate temperature was ramped down for MnAs growth. The narrow heavily doped region beneath MnAs creates a triangular tunnel contact, increasing the spin-injection efficiency. The channel doping (N_D=5 x 10^{16} cm^{-3}) was optimized to ensure a large spin-relaxation time at low temperatures. Lateral spin valves of both conventional and non-local geometry with channel lengths L_{chan}=0.5, 0.6, 0.7, and 0.8 µm with polarizer (P) and analyzer (A) contact length-to-width aspect ratios (L/W) of 10 and 1.5 respectively, were fabricated using conventional wet and dry etching, photolithography, and metallization techniques. The

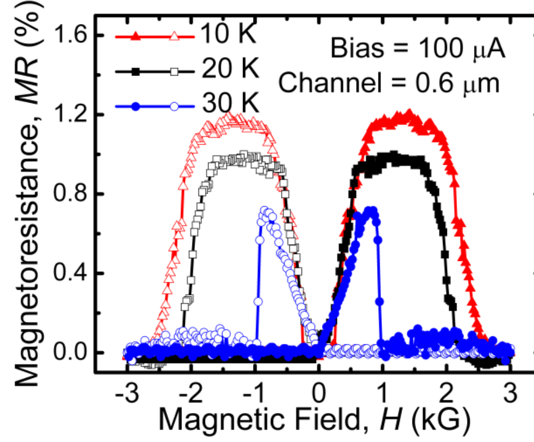

(a)

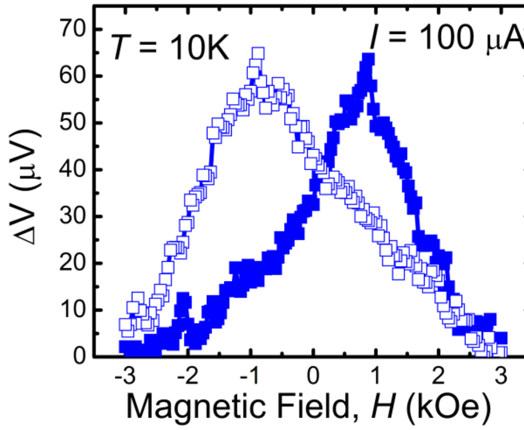

(b)

Figure 2.8: (a) The spin valve shows two MR peaks corresponding to the case when the polarizer and the analyzer are magnetized in opposite directions. The MR decreases with increasing temperature due to decreasing spin-relaxation time; (b) ΔV change as a function of applied magnetic field for a 0.8 μm channel length nonlocal spin valve. Open and closed symbols represent the cases of descending and ascending magnetic fields, respectively.

magnetoresistance, defined as $MR(H) = [R_{\uparrow\uparrow}(H_{sat}) - R_{\uparrow\downarrow}(H)] / R_{\uparrow\uparrow}(H_{sat})$, of the spin valves and control devices were measured for various L_{chan}, temperatures (T), and bias conditions (I_B) using a standard four-probe technique. Figure 2.8(a) shows MR for the spin valves with L_{chan}=0.6 μm at T=10 K and I_B =100 μA. The MR for the device peaks at 1.2% for |H| ~1200 Oe in both directions of the magnetic field sweep. The MR peaks

correspond to antiparallel magnetization of the MnAs pads arising from their coercive field difference. The measured non-local voltage variation of the nonlocal spin valve as a function of magnetic field is shown in Fig. 2.8(b). The nonlocal spin valve removes the AMR contribution and the Hall effects of the ferromagnetic electrodes.

Figure 2.9(a) shows that the peak MR for the conventional spin valve varies exponentially with L_{chan}, which indicates that spin transport is diffusive in the channel. As L_{chan} is decreased, the number of spin-polarized electrons that reach the analyzer before spin relaxation increases, yielding a larger peak MR. Figure 2.9(b) shows the temperature dependence of the peak MR under different bias voltages. Spin valves

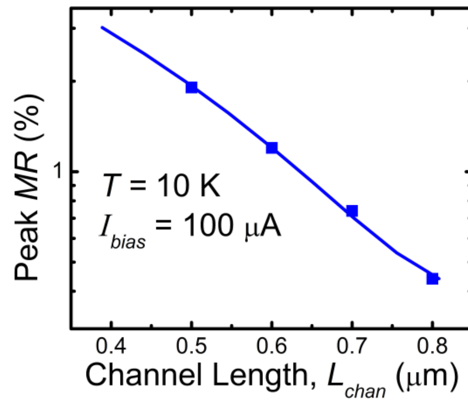

(a)

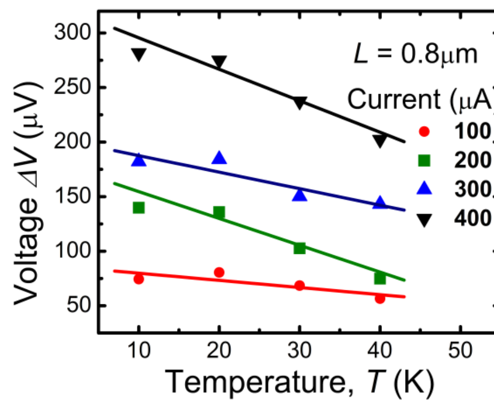

(b)

Figure 2.9: (a) Peak magnetoresistance vs channel length measured at 10 K. (b) Peak ΔV (= $V_{\uparrow\uparrow}$-$V_{\uparrow\downarrow}$) vs

temperature for a 0.8 μm spin valve with applied biases of I_B=100, 200, 300, and 400 μA. The lines represent a linear least squares fit to the data.

across various grown and processed samples with L_{chan} = 0.8 μm were measured under identical experimental conditions, and the results are highly reproducible.

The peak MR increases with decreasing temperature for a fixed bias voltage due to increase in average spin-relaxation time and hence decrease of spin-flip length. The increase in ΔV ($V_{\uparrow\downarrow}$-$V_{\uparrow\uparrow}$) with bias can be explained by considering the effect of spin injection through a tunnel barrier at higher bias values. The depletion region width for the electrons to tunnel through decreases with increasing bias, leading to efficient spin injection from the polarizer. In contrast the analyzer efficiency does not change much with bias. This leads to the overall increase in ΔV at high bias. The analysis of the magnetoresistance characteristics can be done by a simple two channel resistive network model. The maximum spin polarization obtained from this resistive network model is 28.8 %. The spin diffusion length of 1.55 μm is estimated from the magnetoresistance versus L_{chan} measurement.

The simplest manifestation of spin precession between the polarizer and analyzer electrodes is the Hanle effect, in which the magnetic field dependence of the non-local voltage is due to precession and dephasing of the spins in the semiconductor. The precession is induced by applying a small transverse magnetic field that does not change the magnetizations of the electrodes. To test for the Hanle effect in our devices, the magnetizations of contacts were set in the antiparallel state. The magnetic field perpendicular to the plane was then swept, resulting in the black data points shown in the top panel of Fig. 2.10. This procedure was repeated after setting contacts into the

parallel state, yielding the red data points in Fig. 6. These data show a peak at B_z =0 rather than the minimum observed in the parallel state. As can be seen, the two Hanle curves merge at large B_z , because in this limit the spins in the $In_{0.53}Al_{0.47}As$ channel are completely dephased. The difference in the two Hanle signals at B = 0 is 47±1 μV, differing from the spin splitting induced ΔV in the conventional spin-valve by 13 μV.

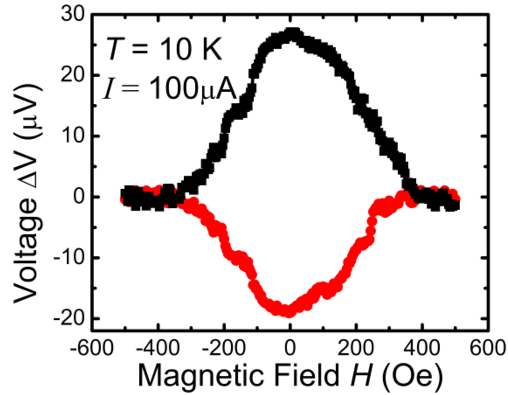

Figure 2.10 : Spin precession measurement in presence of perpendicular magnetic field.

2.5. Summary:

To summarize, type-B MnAs epitaxial layers have been grown on (001)InP substrate and on lattice matched $In_{0.53}Ga_{0.47}As$/InP. The RHEED surface reconstructions were distinctly different even under the same growth conditions indicating that the surface phase diagrams for these heterostructure systems are different. The peak Kerr rotation measured for the type-B MnAs film decreases with increasing temperature and provides an estimate of the Curie temperature (315 K) along the in-plane easy axis. The coercivity of the film was found to decrease by 39% over the temperature range of 10 – 290 K. The magnetocrystalline anisotropy constants in the MnAs layer determined from MOKE measurements were found to be lower than those in bulk MnAs or epitaxially grown type-A MnAs layers on GaAs. The out-of-

plane saturation magnetization measured by a SQUID magnetometer at 10 K was found to be at 1.2 T with a coercivity of 1600 Oe for a 35 nm MnAs layer. These growth conditions were used to demonstrate spin injection and detection using type-B ferromagnetic MnAs in $In_{0.52}Al_{0.48}As$ lattice matched to InP. A peak magnetoresistance value of ~1.2 % was found in a 0.5 μm channel length conventional spin valve. The calculated spin diffusion length was 1.55 μm and spin injection efficiency below the injector contact was 28.8 %.

CHAPTER III

Electric Field Control of Magnetoresistance in a Lateral InAs Quantum Well Spin Valve

3.1 Introduction

Electrical spin injection, manipulation, transport and detection in non-magnetic semiconductors have been demonstrated in several spin based electronic and optoelectronic devices.[10,11,68-70] While we have recently demonstrated the amplification of spin polarization in a 3-terminal spin valve [71], the electrical control of spin transport with a gate-like electrode [72] in a spin valve or lateral magnetoresistance device has proven to be more difficult. This is mainly because of the difficulty in bringing together a channel material with optimal spin-related characteristics with efficient analyzer, polarizer and gate electrodes. In the present study we have investigated the modulation of lateral spin transport in an InAs/$In_{0.53}Ga_{0.47}As$ modulation doped heterostructure [73] lattice-matched to InP with a gate electrode. The electrical control of the magnetoresistance in conventional spin valves is unambiguously observed. We have intentionally placed the modulating gate terminal *outside* the channel region (Fig. 3.1(b)) as opposed to a very recent report in which the gate modulates the non-local spin accumulation.[74] This will allow us to eventually fabricate devices having nanometer scale channel lengths. Since the spin diffusion length in an InAs quantum well is smaller than in GaAs,[75] the small channel length will allow: (a) high-temperature

operation and (b) a higher noise margin in terms of modulation of magnetoresistance. We have also compared our results with those obtained from an identical GaAs channel spin valve, for which no modulation of the magnetoresistance with gate voltage is observed. This confirms that the observed effects in the InAs quantum well spin valves arise from Rashba spin-orbit coupling.

3.2 Design, growth and fabrication of modulation doped $InAs/In_{0.53}Ga_{0.47}As/In_{0.52}Al_{0.48}As$ heterostucture

The device heterostructure, grown on semi-insulating (001) InP substrate, is shown in Fig. 3.1(a). A modulation-doped $InAs/In_{0.53}Ga_{0.47}As/In_{0.52}Al_{0.48}As$ heterostructure is chosen as the active channel of the spin valve since the reported modulation of the Rashba coefficient by a gate bias in an $InAs/In_{0.53}Ga_{0.47}As/In_{0.52}Al_{0.48}As$ heterostructure is relatively large [73] compared to that in bulk GaAs. The measured electron mobility and sheet density in the two-dimensional electron gas (2-DEG) formed in the InAs channel are 5500 $cm^2/V\cdot s$ and 6.2×10^{12} cm^{-2}, respectively, at room temperature. The ferromagnetic polarizer and analyzer contacts are realized with 35 nm type-B MnAs grown at 250^oC (Ref. 77) on 30 nm n-doped (graded) $In_{0.52}Al_{0.48}As$ to form Schottky tunnel barriers. The devices are fabricated by using standard optical lithography, metallization, plasma enhanced chemical vapor deposition (PECVD) and e-beam evaporation techniques. The fabrication steps are as follows. First, MnAs ferromagnetic contacts are wet etched into pads of different aspect ratios [$(L/W)_A$=1.5; $(L/W)_P$=6] with a channel length of 0.6 μm, followed by the definition of a mesa by etching. Then, the insulated gate (100 Å Ti/300 Å Au), situated 0.6 μm from the analyzer, is recessed down as close as possible to the InAs channel for maximum gate action, with a thin layer of 50

nm of SiN deposited between the gate and the channel to minimize leakage current during biasing. Fabrication of the gate electrode is extremely critical for an optimum performance of these devices.

An important aspect of our experiment was the orientation of the MnAs and gate contact pads. Type B MnAs films grown on $In_{0.52}Al_{0.48}As$ are found to have an in-plane easy axis along the $[1\bar{1}0]$ crystallographic direction and the magnetization exhibits strong anisotropy between the [110] and $[1\bar{1}0]$ directions. [11] Therefore two sets of devices were fabricated: one with direction of current flow perpendicular to the magnetization direction (device A) and the other with the current flow parallel to the direction of

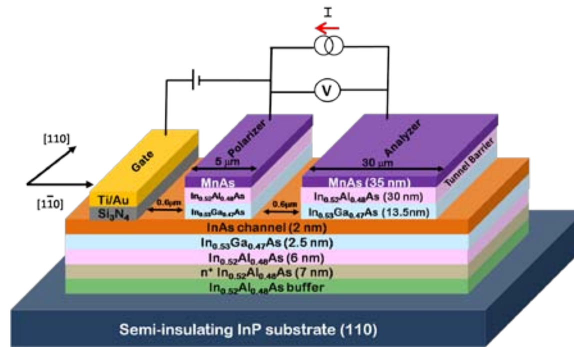

(a)

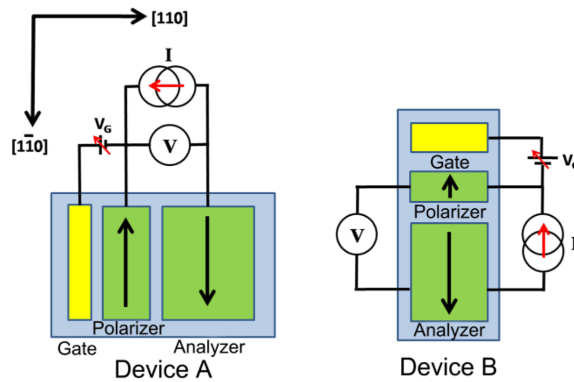

(b)

Figure. 3.1: Schematic representation of: (a) heterostructure of $InAs/In_{0.53}Ga_{0.47}As$ QW spin modulator with ferromagnetic MnAs as spin injector. The entire heterostructure is grown by molecular beam epitaxy;

(b) biasing arrangement for the measurements which are done by applying a constant current bias across the MnAs polarizer and analyzer contacts of the spin valve and varying the gate bias V_G between the gate and polarizer terminals. The variation of magnetoresistance with V_G is determined by measuring the difference in voltage V for parallel and antiparallel magnetization of the polarizer and analyzer.

magnetization (device B). The direction of magnetization of the contact pads was along the $[1\bar{1}0]$ direction (easy axis) for both. The different aspect ratios of the analyzer (A) and polarizer (P) contacts result in a difference in their coercivity which is essential for the operation of a spin valve. The schematic of a fabricated device having a non-local gate electrode is shown in Fig. 3.1(b). Several other control devices were also fabricated. These will be described in the proper context in the following.

3.3 Device measurement and characterization

The devices were mounted in a liquid helium cryostat for measurements, with provision for the application of a magnetic field along the easy axis of the MnAs contacts. Figure 3.2 shows measured magnetoresistance at 10 K as a function of applied magnetic field for device A with zero bias applied to the insulating gate electrode. The device therefore operates as a conventional lateral spin valve and the measured magnetoresistance $MR(H) = [R_{\uparrow\downarrow}(H)-R_{\uparrow\uparrow}(H_{sat})]/R_{\uparrow\uparrow}(H_{sat})$ is a manifestation of the polarizer and analyzer efficiencies changing by different amounts with changing magnetic field, by virtue of their different coercivities. The inset to the figure shows a variation of peak magnetoresistance versus bias current for the same device at different temperatures. The data indicate an almost negligible decrease of magnetoresistance with bias current. The observed behavior is the result of two competing effects: increased spin dephasing due to Dresselhaus and enhanced Rashba spin orbit coupling terms at high electron densities, which will lead to a decrease in injected spin polarization,[76] and a decrease in the polarizer depletion region width with increasing current bias, which will

lead to more efficient tunneling and injection of spin polarized carriers. [11]

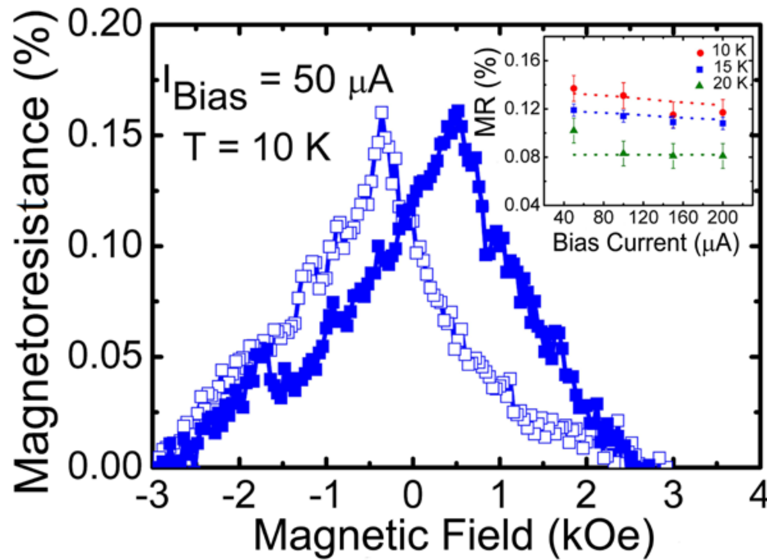

Figure 3.2 : Magnetoresistance measured at 10 K in a conventional spin valve fabricated with an identical heterostructure (figure 1(a)), without gate bias. The channel length for the device is 0.6 μm. The inset shows peak magnetoresistance vs. bias current measured in the same device at different temperatures. The dashed lines are guides to the eye.

Next, the voltage V between the polarizer and analyzer terminals is measured at 10K and 20K for device A as a function of bias applied to the insulated gate, V_G, for both parallel and antiparallel magnetization of the MnAs pads. The measurement is done at a constant injection current of 100 μA and with no externally applied magnetic field. The variation of magnetoresistance with gate bias is shown in Fig. 3.3(a). The oscillation is a result of the crossover in the parallel and anti-parallel voltages, shown in the inset, which is due to the spin precession of injected carriers. Identical data were recorded with a constant injection current of 150 μA between the polarizer and analyzer (Fig. 3.4(a)). [79] The experiment was repeated with two control devices, in both of which the channel length is

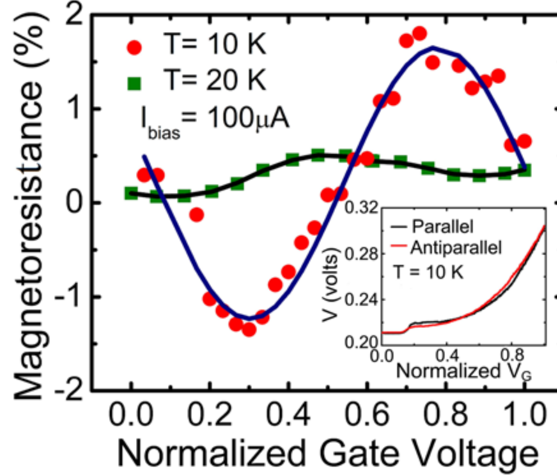

(a)

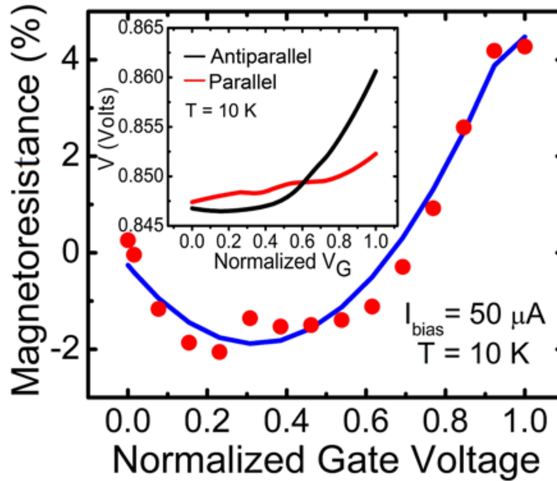

(b)

Figure 3.3: Measured modulation of magnetoresistance with gate bias at 10 and 20K in an $InAs/In_{0.53}Ga_{0.47}As$ QW spin valve for (a) spin transport normal to direction of magnetization; and (b) spin transport parallel to direction of magnetization. The direction of magnetization is always along the [$1\bar{1}0$] direction, which is the easy axis of magnetization of type B MnAs contacts. The insets show the measured output voltage V as a function of normalized V_G for parallel and antiparallel magnetization (maximum actual gate voltage applied for this measurement is 8V).

150 μm and in one of them the analyzer is a non-magnetic Ti/Au contact (Fig. 3.4). All other dimensions are maintained the same. For both of these devices, the variation of V with V_G for parallel and antiparallel magnetization of the polarizer and analyzer does not exhibit any cross over. As a consequence no oscillation of the magnetoresistance as a

function of gate voltage is recorded. These experiments strongly suggest that the data of

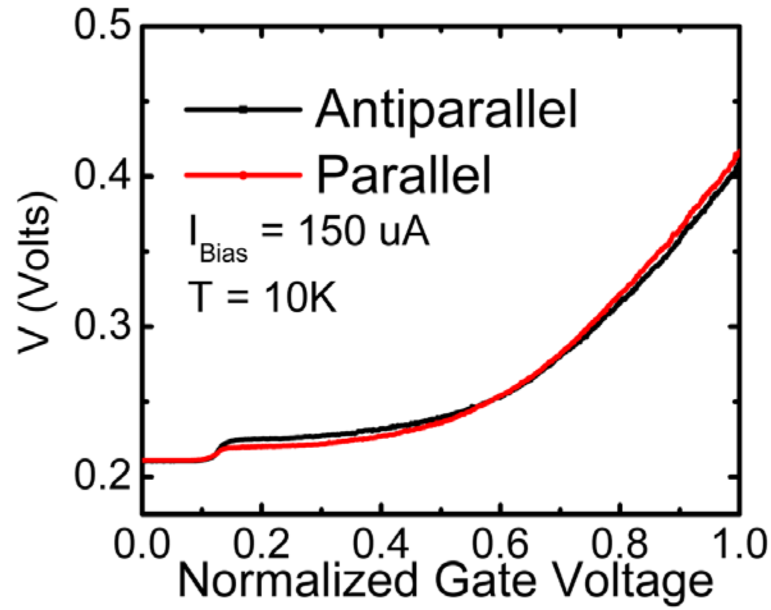

(a)

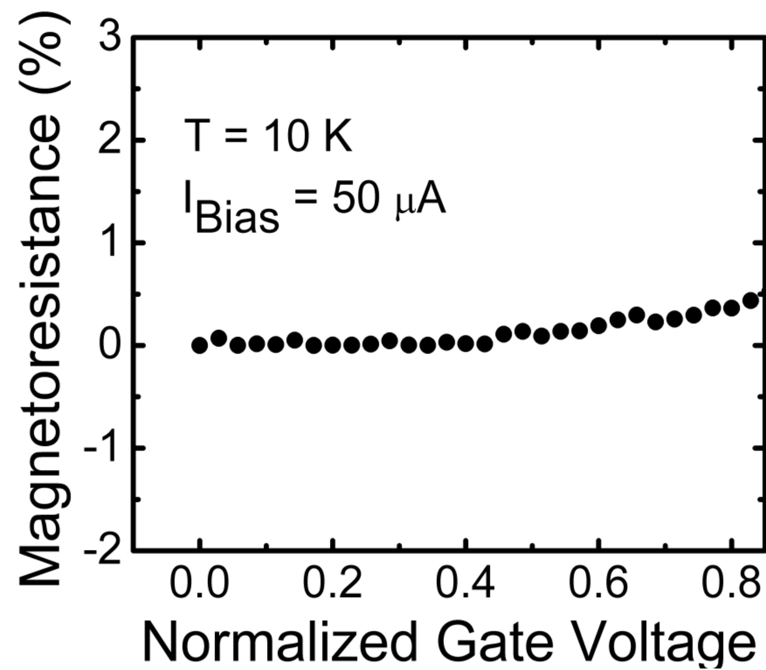

(b)

Figure 3.4: **(a)** Measured output voltage versus gate bias for parallel and antiparallel magnetization of the polarizer and analyzer contacts at a constant bias current of 150 uA.**(b)** The magnetoresistance vs. gate bias measured for a control device with non-magnetic analyzer.

Fig. 3.3(a) are not related to spurious magnetic effects in the contact or channel regions. The oscillation in the magnetoresistance is a manifestation of spin dephasing of the injected electrons and is an indication of the modulation of spin transport by an applied electric field. The response of device A is not entirely understood in the framework of Rashba spin-orbit coupling. The observed effect is probably operative under the large (5 μm) polarizer contact, rather than in the channel region between the polarizer and analyzer. In this case the variation can be simulated by a function $\cos(\Delta\theta)$, where $\Delta\theta$ is not $2m^*\alpha_{so}L/\hbar^2$, [72] but simply $C\alpha_{so}$, where C is a constant dependent on the polarizer characteristics and α_{so} is the spin-orbit coupling constant dependent on the gate bias. The data obtained at 20K show that the effect is reduced.

Measurements were repeated for device B in which the spin current flow is in the same direction as the magnetization of the polarizer and analyzer. In other words they are both along the $[1\bar{1}0]$ crystallographic direction. The measured output voltage (inset) and the magnetoresistance as a function of gate bias are shown in Fig. 3.3(b). In this case a very clear difference and crossing of the output voltage between parallel and antiparallel magnetization directions are observed. Also, the difference becomes very large at higher gate biases. Compared to Fig. 3.3(a), the change in magnetoresistance is a factor of two larger for this device. Therefore, the modulation of spin transport is more significant in this case. Nonetheless, our results are comparable to those for a device with the gate placed in the non-local channel.[74]

3.4 Control experiments

As a final control experiment (Fig. 3.5), measurements were made on a GaAs-based spin valve with a gate terminal adjacent to the polarizer. The geometry is identical to those shown in Fig. 3.1(b). The channel is formed in a 0.5μm thick layer of Si-doped GaAs with $n = 1x10^{17}$ cm^{-3}. The Schottky tunnel polarizer and analyzer contacts are formed by a graded heavily doped 30 nm GaAs layer atop the channel layer and 35 nm MnAs. The direction of magnetization of the polarizer and analyzer is the same as the direction of the spin current. Good spin valve magnetoresistance characteristics are recorded with $V_G = 0$. With an application of gate bias, the magnetoresistance in this device remains

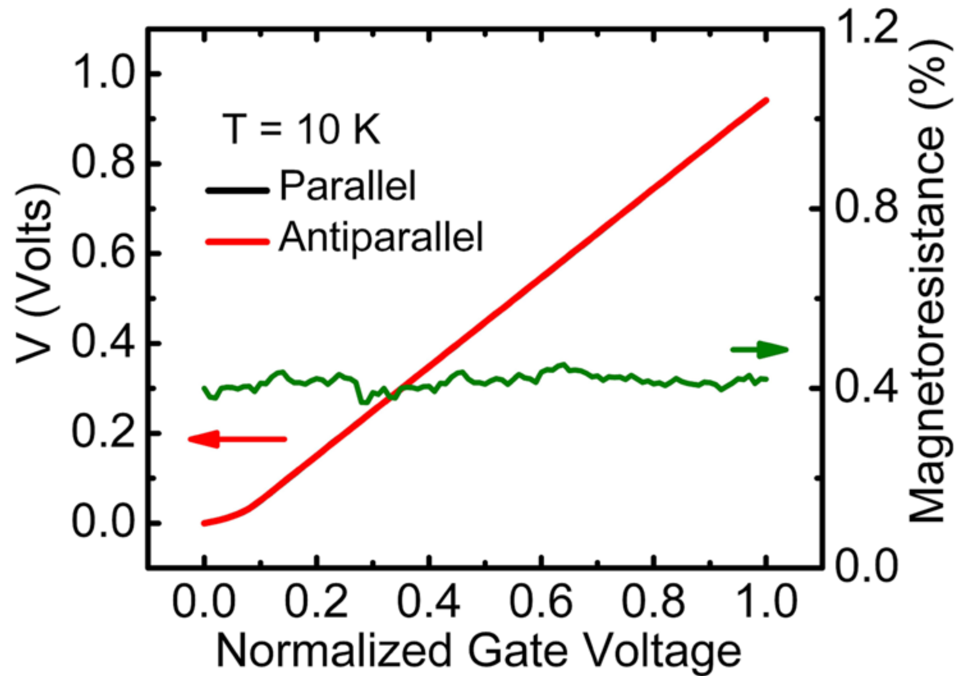

Figure 3.5: Measured output voltage V for parallel and antiparallel magnetizations of the polarizer/analyzer, and magnetoresistance as a function of gate bias V_G for a GaAs spin valve with a gate terminal as shown in Fig. 1(b) (maximum actual gate voltage applied for this measurement is 5V).

constant. This is expected, since spin-orbit coupling is much smaller in GaAs compared

to that in InAs. This result also provides additional evidence that the observed effect in the InAs quantum well device B is due to Rashba spin-orbit coupling induced by the gate voltage. The larger effect in device B may be partially due to modulation of spin transport in the channel region also, but it is not possible to ascertain the exact degree of this contribution. It is unlikely that the in-plane anisotropy of spin orbit coupling and spin relaxation time play any role in determining the difference in response between device A and B. The fact that the magnetoresistance can be modulated even in a device with large polarizer/analyzer contact dimensions and channel length is very encouraging. [78,79] By shrinking these dimensions considerably to submicron and nanometer scales, the adjacent gate can easily induce an electric field in the channel region and these devices can be operated at higher temperatures and higher frequencies.

3.4 Summary

In conclusion, we have demonstrated the modulation of magnetoresistance of an $InAs/In_{0.53}Ga_{0.47}As/In_{0.52}Al_{0.48}As$ lateral spin valve with a gate electrode placed alongside the MnAs polarizer contact and outside the channel. The results indicate that the change in magnetoresistance is caused, in part, by Rashba spin-orbit coupling due to the gate bias. While this demonstration together with the recently reported work [73] are very encouraging, further work is necessary before any claims to practical room-temperature applications can be made.

CHAPTER IV

Characteristics of a High Temperature Vertical Spin Valve: The Role of Defect Free P-doped GaAs

4.1 Introduction

Spintronic devices essentially involve the process of injection, transport, manipulation, and detection of spin-polarized carriers. Two and three terminal vertical semiconductor based electrical spin devices have been successfully demonstrated with dilute magnetic semiconductors as the spin contacts [80-82]. In this work, we report room temperature operation of a vertical spin valve by using MnAs as the spin injector/detector on a GaAs substrate, where spin polarized electrons tunnel in and out of the valence band of a heavily p-doped GaAs:Mn layer. Realization of this device is made possible with the molecular beam epitaxial (MBE) growth of device quality MnAs/GaAs:Mn/MnAs heterostructures at very low temperatures. The device exhibits a peak magnetoresistance of 25 % at 10 K which reduces to ~ 1% at room temperature. The results are analyzed with a model incorporating valence band electron tunneling of spin polarized carriers in a degenerately Mn-doped semiconductor.

4.2 Design, epitaxial growth and fabrication of a vertical spin valve

The spin relaxation mechanism in p-doped semiconductors is relatively insensitive to temperature and therefore naturally lends to high temperature operation. Contrary to hole

injection in the valence band, where experimental realization of vertical heterostructures with high operating temperatures is restricted by the Curie temperature of the spin polarized hole injector, we demonstrate that VBET can be key to the realization of high temperature semiconductor spintronic devices. It is worth noting here that electron injection in the conduction band for a similar structure would require a degenerately n-doped GaAs intermediate layer, which is not realizable from the perspective of epitaxial growth.[83] High Curie temperature of MnAs spin injector/detector [84] enables room temperature spin injection and detection in these vertical heterostructures using this VBET phenomenon. We have shown that the spin dependent response in these devices can be further enhanced by improving the quality of ferromagnet/semiconductor interface. Finally, a key feature is the ability to successfully grow epitaxial and device quality GaAs on half-metallic MnAs. In VBET, spin polarized electron from the Fermi level of a ferromagnetic metal tunnels into an empty state in the valence band of a p-doped semiconductor, and subsequently tunnels out into an empty conduction band state of another ferromagnet. The process is schematically illustrated in Fig. 4.1(a). The requirement for VBET is that a heavily doped p-type semiconductor is sandwiched between two ferromagnets with appropriate tunnels barriers on both sides. A schematic of the heterostructure used in this study and grown by low temperature molecular beam epitaxy (MBE) is shown in Fig. 4.1(b) We have used MnAs as the ferromagnetic contact which has a Curie temperature above 300 K. Mn (~0.9%) doped GaAs grown at 250°C has been used as the p-doped layer. MnAs atoms allow low temperature p-doping of GaAs without effecting the MnAs/GaAs interface, which is otherwise difficult to achieve. The samples, grown by molecular beam epitaxy (MBE), consist of MnAs (35

nm) / GaAs (1 nm) / AlAs (1.5 nm) / GaAs:Mn (7 nm) / AlAs (1.5 nm) / GaAs(1 nm) / MnAs (35 nm) on a semi insulating GaAs (001) substrate. The entire heterostructure is grown at a low substrate temperature of 250°C to avoid inter layer diffusion of Mn atoms and formation of Mn-Mn clusters. The growth of the GaAs layer (1 nm) on the bottom layer of MnAs is the most critical step in this heterostructure. The MnAs layer is annealed at 350°C under an arsenic flux of 7 x 10^{-6} torr in order to reduce surface roughness to <0.7 nm, which facilitates the subsequent epitaxial growth of the GaAs and subsequent layers. The reduction in the surface roughness and the improved quality of the GaAs layer were verified by atomic force microscopy measurements. It may be noted that besides acting as a tunnel barrier for efficient spin injection and detection, the AlAs layers also prevent segregation of Mn atoms at the MnAs/GaAs:Mn interfaces. [85]. Spin

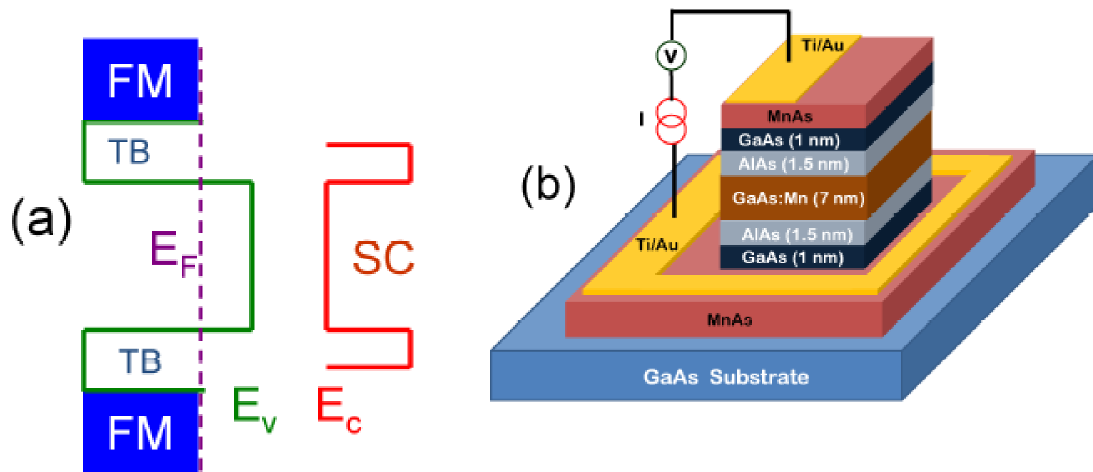

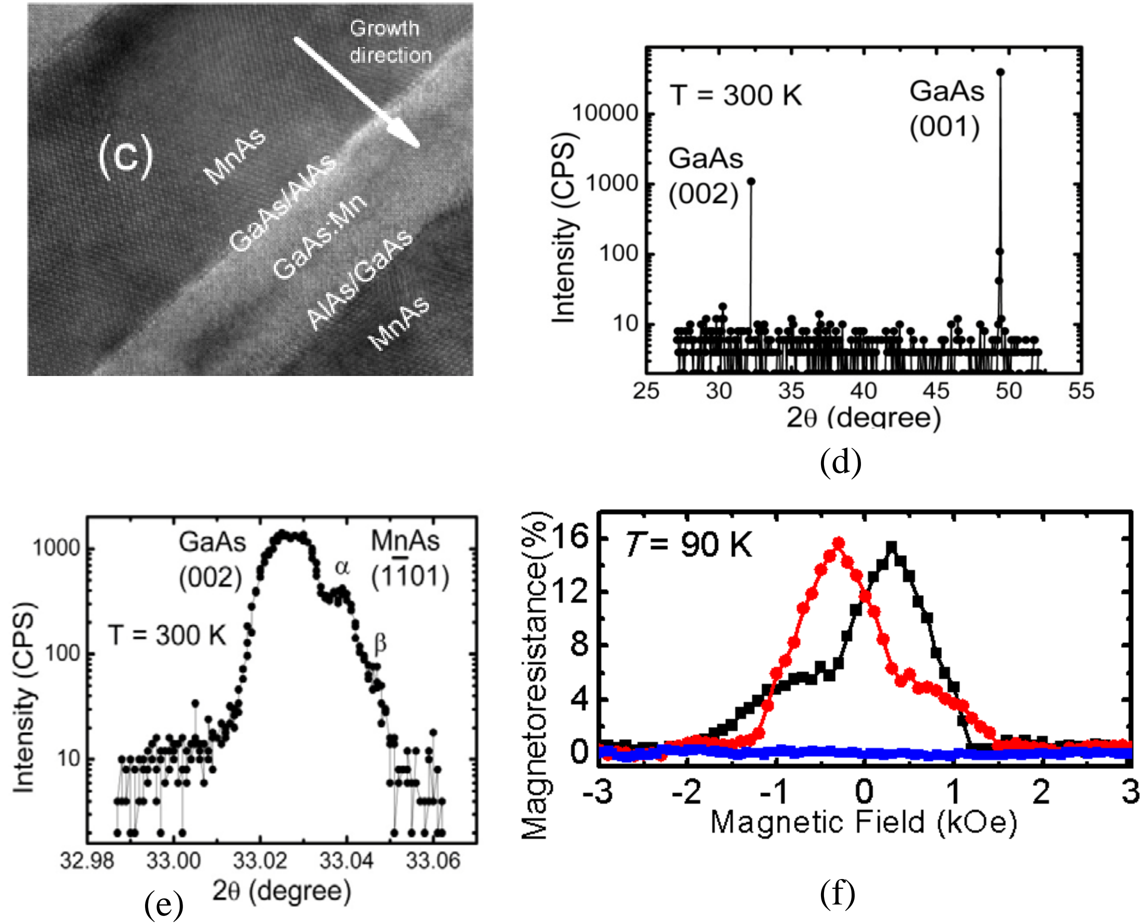

Figure 4.1: (a) Schematic band diagram to illustrate valence band electron tunneling from ferromagnet (FM) Fermi level to the empty valence band states of semiconductor (SC) through insulating tunnel barrier (TB); (b) semiconductor heterostructure and two terminal vertical spin valve for electrical spin injection and detection; (c) TEM image showing ferromagnet/semiconductor sharp interfaces; (d) x-ray diffraction measurements indicate absence of Mn segregation in the fully grown heterostructure;(e)α-phase MnAs peak seen as a shoulder to the (002)GaAs secondary peak at 33.03°;and (f) magnetoresistance as a function of magnetic field in vertical spin-valves. Spin polarized electrons tunnel from MnAs Fermi level into the empty valence band states of p-doped GaAs. The carriers then drift and diffuse through GaAs. Finally, the spin polarized electrons tunnel out to the empty conduction band states of the second MnAs contact.

polarized electrons tunnel from MnAs (source) through the undoped insulating barrier of AlAs into the empty states in the valence band of p-doped GaAs and are transported through this layer by drift and diffusion before tunneling out into the conduction band states of the second MnAs (drain) layer. A cross-sectional transmission electron microscope (TEM) image of the heterostructure is shown in Fig. 4.1(c). X-ray diffraction measurements (XRD) performed on the fully grown heterostructure do not show any

signs of Mn segregation (Fig. 4.1(d)). XRD peaks present at 33.04 ^{o}, shown in fig. 4.1(e), correspond to the MnAs (1-101) planes of the α-phase (ferromagnetic NiAs-type hexagonal structure) .

4.3 Energy band diagrams and valence band electron tunneling

The energy band diagrams of the heterostructure for different bias voltages and doping concentration of the p-GaAs layer are determined by self-consistently solving Schrodinger and Poisson equations and using appropriate values for the material parameters. Figure 4.2 shows conduction (E_c) and valence band (E_v) edges and hole density as a function of position. Figures 4.2(a) and (b) show the band alignment for degenerately ($p = 9 \times 10^{19}$ cm^{-3}) and non-degenerately ($p = 2 \times 10^{19}$ cm^{-3}) doped GaAs under equilibrium ($V_b = 0$) condition. It can be seen that the Fermi level (E_f) is inside the valence band for the degenerately doped case, whereas it lies in the bandgap for the non-degenerate case. Under a bias, spin polarized electrons from the Fermi level of the ferromagnet can directly tunnel into the valence band state in the case of degenerately doped GaAs (Fig. 4.2(c)). However there is no such available state for the non-degenerate case. Electrons can only tunnel from an energy level much below the Fermi

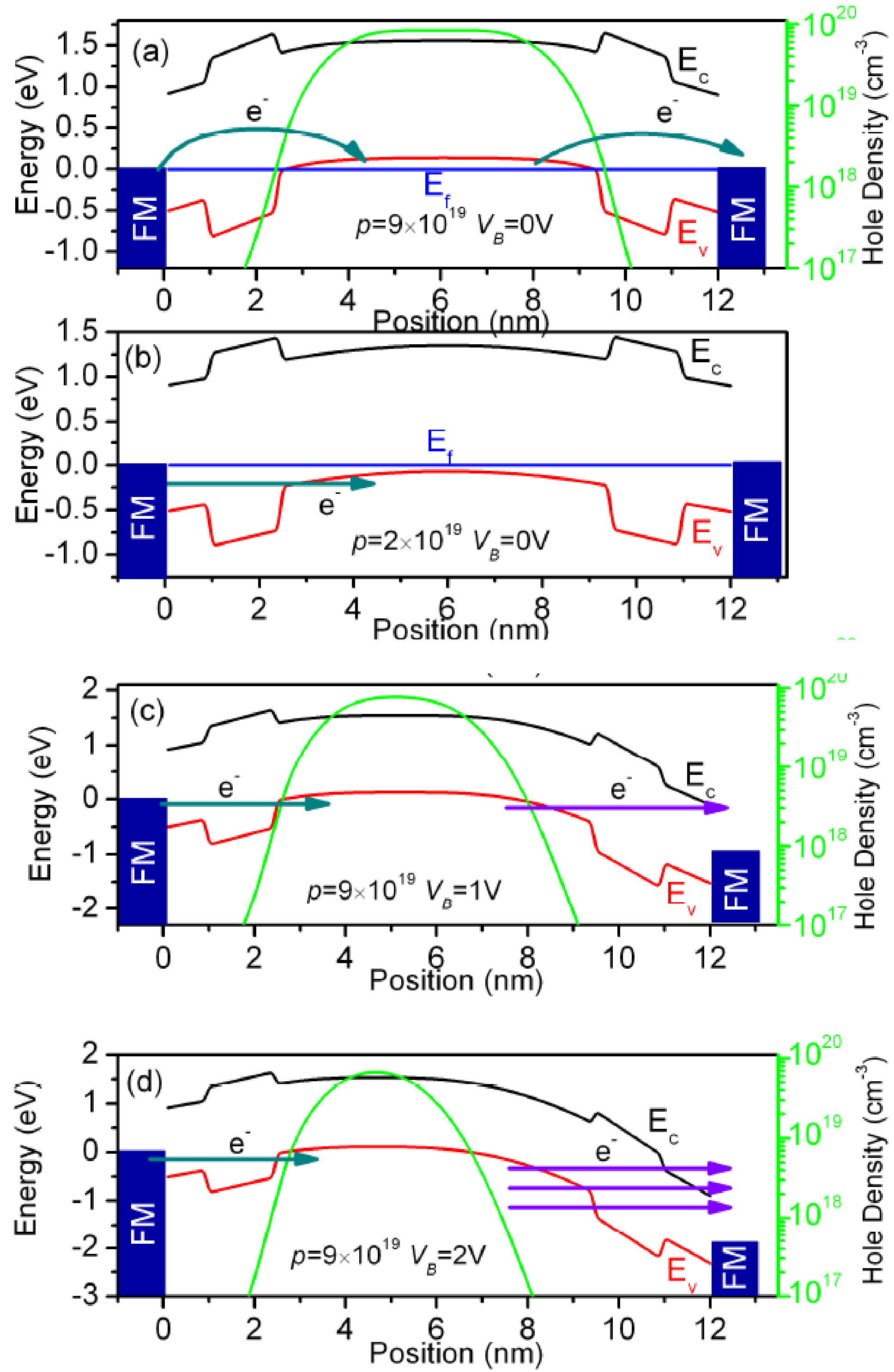
(a)
Energy (eV)
Hole Density (cm^-3)
E_c
e^-
e^-
E_f
FM
FM
p=9×10^19 V_B=0V
E_v
Position (nm)
(b)
E_c
E_f
e^-
FM
FM
p=2×10^19 V_B=0V
E_v
Position (nm)
(c)
E_c
e^-
e^-
FM
FM
p=9×10^19 V_B=1V
E_v
Position (nm)
(d)
E_c
e^-
e^-
FM
FM
p=9×10^19 V_B=2V
E_v
Position (nm)

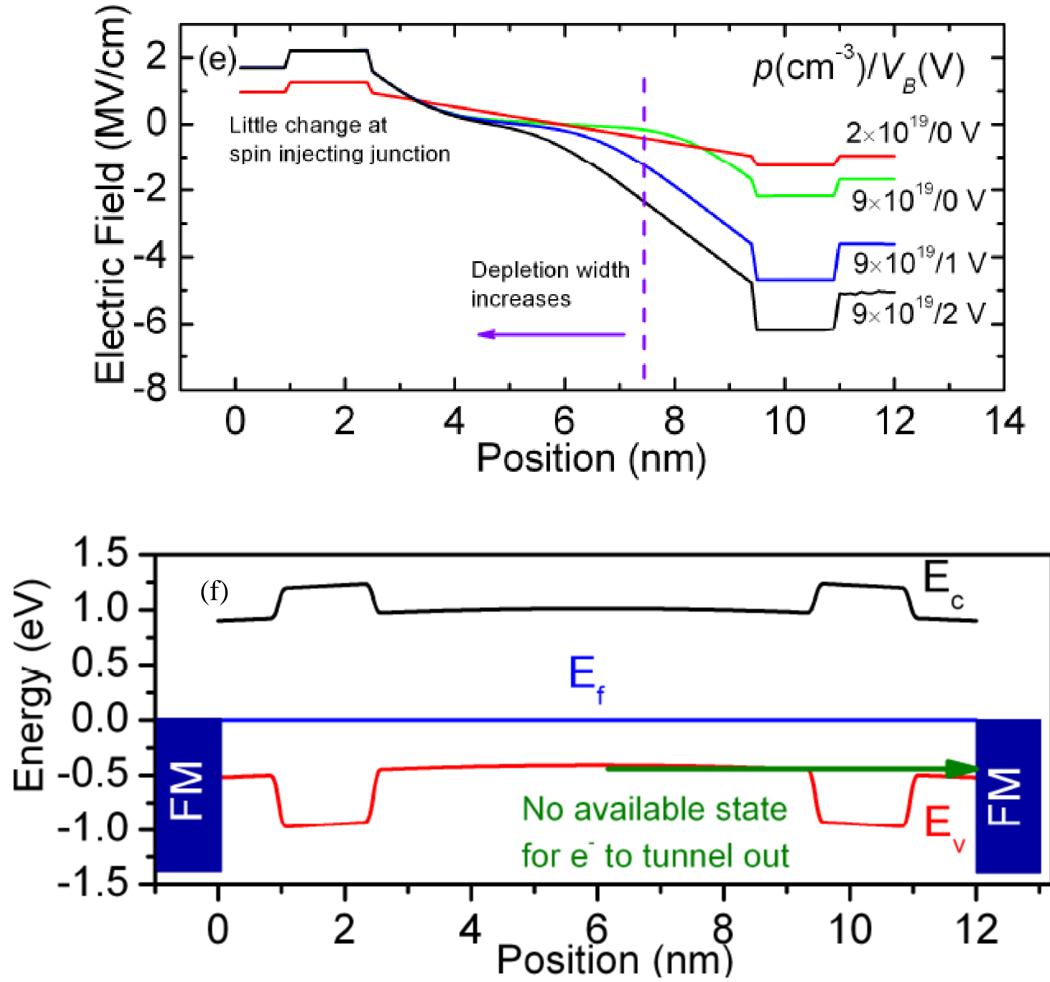

Figure 4.2 Energy band diagrams and electric field profile for different bias conditions and doping concentrations. Band diagrams for (a) p = 9 x 10^{19}cm^{-3} (degenerately doped) and V_B = 0, (b) p = 2 x 10^{19} cm^{-3} (non-degenerately doped) and V_B = 0, (c) p = 9 x 10^{19} cm^{-3} and V_B = 1V (low bias), and (d) p = 9 x 10^{19} cm^{-3} and V_B = 2V (high bias); (e) electric field profile under various operating conditions and doping densities. Electrons can directly tunnel from ferromagnet Fermi level to the empty valence band states of degenerately doped GaAs. Unpolarized electrons may tunnel out at large bias, which do not contribute to the spin polarized current. The electric field increases rapidly with bias at the drain end; (f) Energy band diagram for lightly *p*-doped (p = 10^{17} cm^{-3}) GaAs:Mn layer. Under equilibrium condition, there is no available state for electrons to tunnel out into the second ferromagnetic (FM) contact.

level as shown in Fig. 4.2(b). The spin-polarization in a ferromagnet is a strong function of energy and has a complex dependence on the detailed band-structure. [86] It can even become very small at certain energy levels below E_F. Hence, degenerate doping of the GaAs layer helps to alleviate this ambiguity as the spin polarization at the Fermi level is

always non-zero for MnAs and also for other well known ferromagnets e.g. Fe, Co, and Ni below the Curie temperature. However, it may be noted that a selective combination of ferromagnet, ferromagnet/semiconductor interface and doping of semiconductor can preferentially inject carriers from an energy level where the polarization is much higher than that of at the Fermi level, which can lead to much higher spin injection efficiency. Since the tunnel barrier is triangular in shape, the tunneling being here is similar to Fowler-Nordheim tunneling [87]. Spin injection and detection will be inefficient for low p-doping concentration in the GaAs layer as there will not be any available state for tunneling out electrons under small bias conditions (Fig. 4.2(f)).

Figure 4.2(c) and (d) show band diagrams for applied bias V_b = 1V and 2V, respectively. The change in band bending is mostly restricted to the drain end and there is little change at the source end. The source tunnel barrier thickness and height remain the same and almost all voltage appears across the reverse bias drain terminal. This is further confirmed from the electric field profile shown in Fig. 4.2(e). Degenerate doping therefore also helps in the electrostatic decoupling of source and drain junctions. The hole concentration profiles indicate that the drain end depletion width and electric field increases with increasing bias, which leads to the change in spin detection efficiency. It may be noted that the electrons tunnel at an energy level which is higher than the Fermi energy at the drain end and the density of states for spin-up and spin-down electrons will change with bias. This effect is also present in tunneling magnetoresistance (TMR) devices [88]. At high enough bias, electrons from the filled valence band states below the Fermi level can tunnel to the empty states of the drain contact (as shown in Fig. 4.2(d)). These unpolarized electrons will not contribute to the spin polarized current. The

increasing depletion region width, high electric field, change in ferromagnetic contact polarization and increase in unpolarized current tend to decrease the spin detection efficiency at higher bias values. In the extreme case, electrons may gain enough energy from the high electric field, leading to avalanche multiplication, and they will be completely depolarized at the drain end.

4.4 Experimental characterization and device modeling

To measure electrical spin injection and detection, vertical spin-valves are fabricated in these heterostructures using conventional fabrication techniques (Fig. 4.1(b)). The devices are measured in a cryostat placed between the poles of an electromagnet. Figure 4.1(d) shows the magnetoresistance of the vertical spin-valve as function of magnetic field. The two peaks in the magnetoresistance correspond to the anti-parallel alignment of source and drain MnAs pads [68,86]. No magnetoresistance was observed in control devices where the top MnAs contact was replaced with non-magnetic Ti/Au metal contact (Fig. 4.1(d)). It is important to note that the concentration of Mn (0.9%) in the GaAs layer is low and superconducting quantum interference device magnetometry (SQUID) indicates that the Curie temperature is well below 50 K. Figures 4.3(a) and (b) show the measured peak magnetoresistance as a function of temperature and bias, respectively. It is observed that the magnetoresistance decreases with increasing temperature and a peak magnetoresistance of 1% is measured at room temperature. The decrease in magnetoresistance is primarily due to three effects: (1) the contact polarization of MnAs decreases with increasing temperature due to spin-wave (SW) excitation; (2) spin independent tunneling (SIT), which does not contribute to

magnetoresistance, increases with increasing temperature, and (3) spin-relaxation (SR) in the degenerately doped semiconductor. [89] To determine the degree of contribution from each of these factors and also to estimate the spin diffusion length in p-doped GaAs, we have analyzed the results with the Tsu-Esaki model using Wentzel-Kramers-Brillion (WKB) approximation for spin injection and detection through tunnel barriers and spin drift-diffusion for spin transport in GaAs [90,91]. Figure 4.3(c) shows the effective polarization of MnAs with varying temperature as determined by SQUID magnetometry of MnAs and polarization measurements on spin-valves [68] and spin lasers [82]. The polarization goes to zero at ~320 K which is the Curie temperature of MnAs. The estimated decrease in magnetoresistance due to decrease in contact polarization (labeled SW) is shown in Fig. 4.3(a). It is observed that almost 50% of the reduction in magnetoresistance is due to the decrease in contact polarization; however, it does not account for the entire reduction. To account for the effect of thermally activated spin independent transport we have considered a parallel leakage path by hopping conduction in the tunnel barrier. The GaAs/AlAs layer is grown at a much lower temperature and therefore the local defect states can act as hopping sites for electron transport. The temperature (T) dependence of hopping conductance through a series of N localized states is given by [92]:

$$G_{hop} = \sum S_N T^{N-2/N+1}, N = 1,2, \dots . \tag{4.1}$$

where S_n are determined by the density and nature of localized states. The temperature exponent, $\gamma = N - 2/(N+1)$ increases with increasing number of hopping sites and the spin independent hopping conductance goes up. The number of hopping sites is determined to be N = 2 from the exponent ($\gamma \approx 1.3$) of temperature dependent current-

voltage characteristics of control devices with only one tunnel barrier. The decrease in magnetoresistance due to the combination of decreasing contact polarization and hopping conductance is also shown (labeled SW + SIT) in Fig. 4.3(a). There is some mismatch between the experimental and the predicted values, which can be account for by considering spin relaxation in the p-doped GaAs. Figure 4.3(a) also shows (labeled SW+SIT+SR) the additional contribution to the decrease in magnetoresistance due to enhanced spin relaxation in the GaAs layer with increasing temperature. The spin diffusion length (λ) is estimated from the reduction in magnetoresistance due to spin relaxation and spin drift-diffusion model. The spin relaxation time ($\tau = \lambda^2/D$) is determined by using the generalized Einstein relation between diffusion coefficient (D) and mobility (μ) as:

$$\frac{D}{\mu} = \frac{1}{q}\int_0^\infty S(E)F(E)dE \Big/ \int_0^\infty S(E)\frac{\partial F}{\partial E}dE \qquad (4.2)$$

where S is the density of states, F is the Fermi-Dirac distribution, and q is the electronic charge. Figure 4.3(d) shows the spin relaxation time as a function of temperature. τ decreases very rapidly at low temperature and the long tail indicates that τ is relatively insensitive at higher temperatures. These characteristics match well with the Bir-Aranov-Pikus (BAP) mechanism for spin relaxation in p-doped semiconductors [93] and confirm that the D'yakonov-Perel (DP) mechanism for spin relaxation is not dominant in p-doped semiconductors at high doping concentrations. Therefore, room temperature operation of these devices is not limited by the spin relaxation time in GaAs, as the BAP mechanism dominates only at low temperature. It is interesting to note from Fig. 4.3(a) that defect states in the tunnel barrier are the most detrimental to spin polarized carrier injection and

detection, particularly at high temperatures. Though the decrease in ferromagnetic

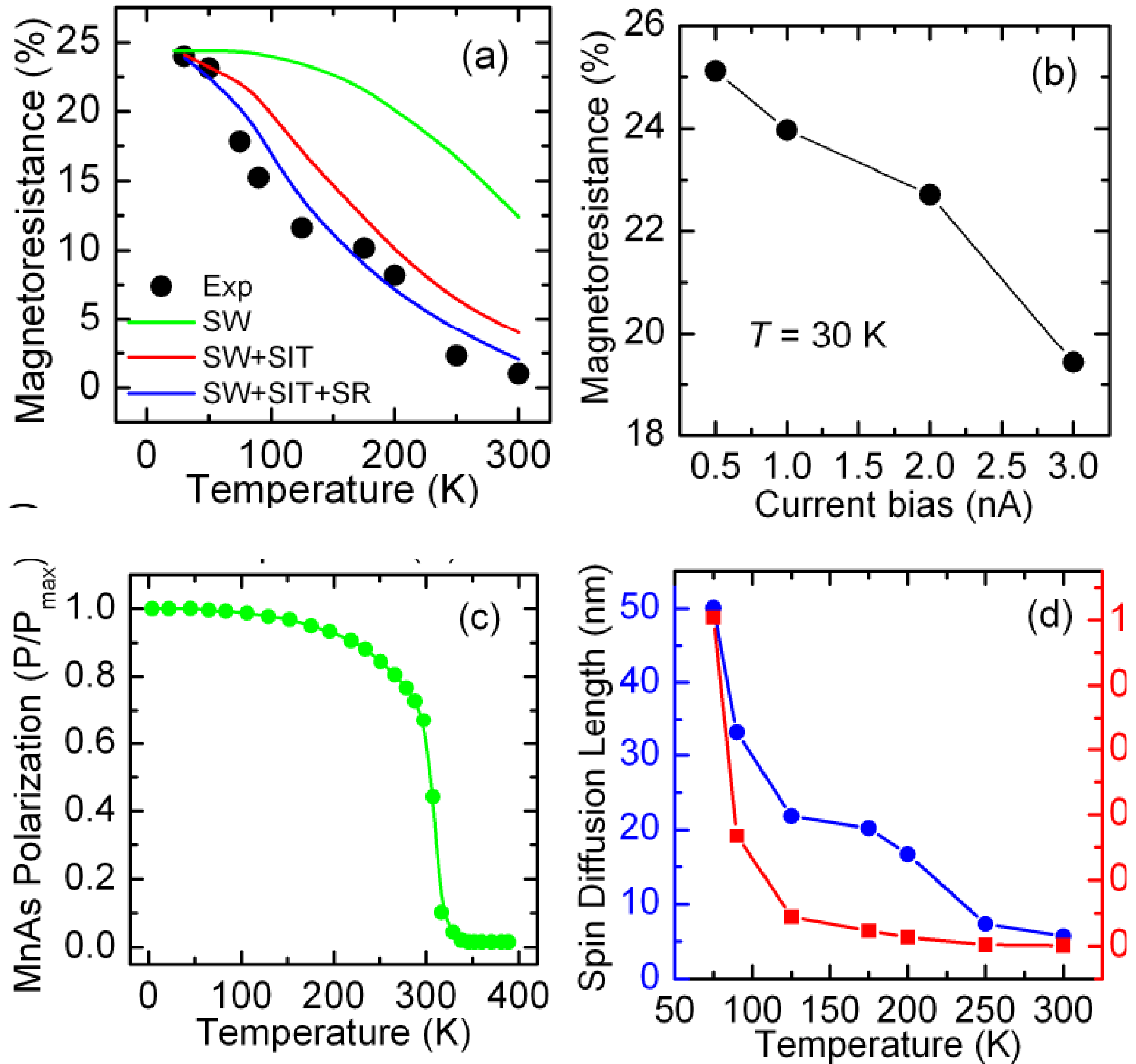

Fig. 4.3: Measured and calculated characteristics of vertical spin valves with p-doped GaAs channel. Measured peak magnetoresistance is shown as a function of (a) temperature and (b) bias. (c) MnAs polarization and (d) spin diffusion length and spin relaxation time as a function of temperature are shown. Reduced ferromagnetic contact polarization due to spin wave excitation (SW), spin independent tunneling (SIT) conduction due to the hopping transport at the ferromagnet/semiconductor interface, and spin relaxation (SR) in the GaAs channel can explain the observed dependency (also shown in (a)). The spin relaxation in the p-doped GaAs is dominated by the BAP mechanism which is found to be relatively insensitive to temperature for T > 125 K.

contact polarization with increasing temperature is unavoidable, spin dependent effects can be increased considerably by improving the interface quality and minimizing the hopping transport. The decrease in magnetoresistance with increasing bias, as observed

in Fig. 4.3(b) has been explained earlier.

4.5 Control devices

Several control devices were realized with different compositions of Mn in the GaAs layers as well as different thickness of the GaAs layer. For the first set of control devices shown in fig. 4.4 the GaAs:Mn thickness was same as the that shown in fig. 4.1(b). The Mn doping in the layer was however increased by 1.5 times. It was observed that the measured magnetoresistance of these devices were higher compared to those shown in fig. 4.1. This was attributed to higher concentration of Mn lead to more available states for the spin polarized electron tunneling. This reduced the contribution of SIT at low temperatures. However, at higher temperatures the higher doping in the GaAs layer leads to higher contribution to spin relaxation. This effect together with spin independent tunneling start dominating at higher temperatures and magnetoresistance decreases rapidly at higher temperatures. The HRTEM image of this device shown in fig. 4.4(b) confirms non-ideal characteristics in terms of Mn clustering and stacking faults, either or both of which could lead to increased SIT.

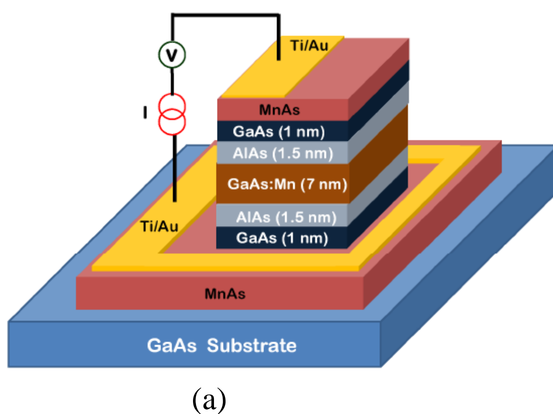

(a)

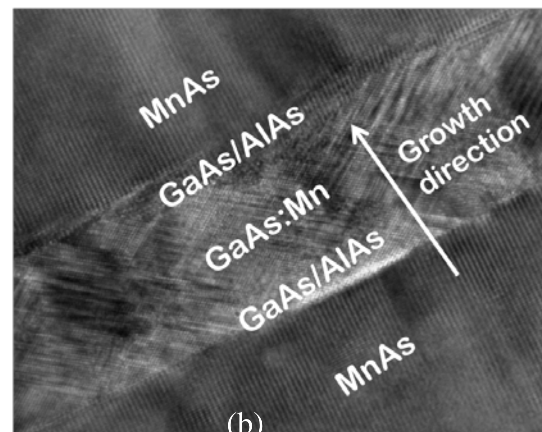

(b)

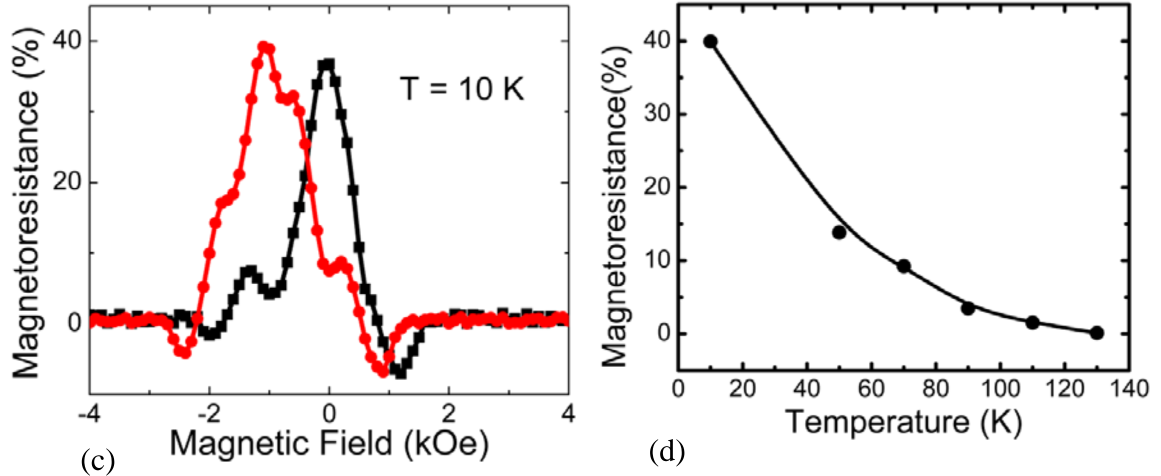

Fig. 4.4: (a) Semiconductor heterostructure of the two terminal vertical spin valve for electrical spin injection and detection. In this device the manganese doping concentration was also increased to 1.5 %; (b) TEM image showing ferromagnet/semiconductor stacking faults and unclear interfaces. There is also significant segregration of manganese in the GaAs layer; and (c) magnetoresistance as a function of magnetic field in vertical spin-valves. (d) Measured and calculated characteristics of vertical spin valves with p-doped GaAs channel.

In the second set of control devices the concentration of Mn dopant was constant but the thickness of the GaAs:Mn layer was reduced to ~1 μm (Fig. 4.5(a)). A peak magnetoresistance of 2 % was measured at 10 K. the thin GaAs:Mn layer leads to increased confinement, resulting in a reduced number of available states in the valence

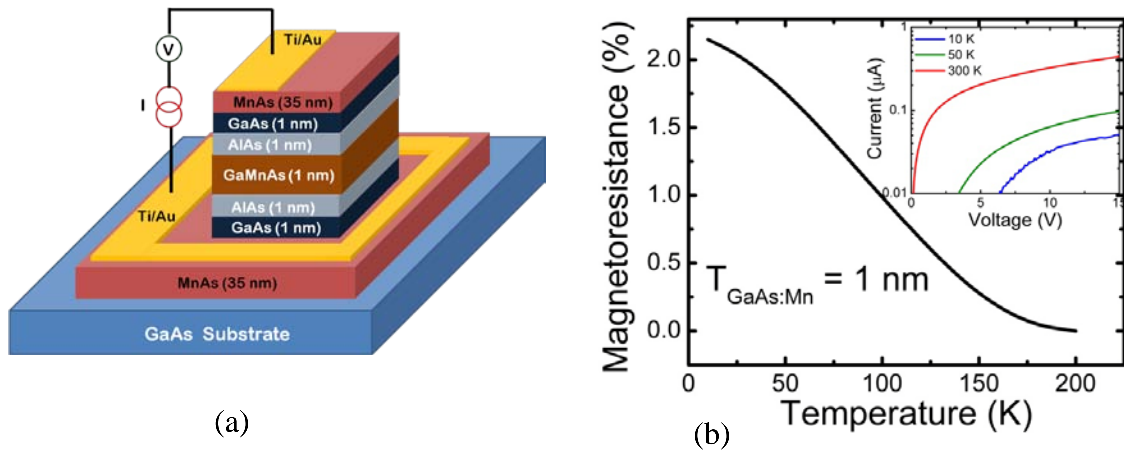

Fig. 4.5: (a) Semiconductor heterostructure of the two terminal vertical spin valve for electrical spin injection and detection. In this device the thickness of the GaAs layer was reduced to 1 nm; (b) Measured characteristics of vertical spin valves with p-doped GaAs channel.

band. Thus, spin independent tunneling through defect states dominate, causing a decrease in magnetoresistance measured at low temperatures, as seen in Fig. 4.5(b). The MR values of this device are similar to those reported by Sugahara *et.al.* on tunneling magnetoresistance devices.

4.6 Conclusion

To summarize, we have demonstrated that valence band electron tunneling in a vertical structure can play a crucial role in the realization of room temperature spintronic devices. Vertical structures allow precise control of spin transport length in semiconductors. Electrical spin injection and detection efficiency depend on ferromagnet/semiconductor interface and p-doping concentration of the semiconductor region. Spin independent hopping conductance at the tunnel interface reduces spin injection and detection efficiency considerably, which needs to be improved to increase the magnitude response. We find that the BAP mechanism is the dominant spin relaxation process in these devices. Though the spin relaxation time constant is relatively smaller for the BAP mechanism than the DP mechanism, the former is relatively insensitive to temperature. Hence, p-doped semiconductors can be a natural choice as the channel material for temperature insensitive spintronic devices. The vertical heterostructure described here can be used for a host for three terminal magnetoresistance devices. These devices can also be used for energy resolved spectroscopy studies of spin dependent density of states in ferromagnets.

CHAPTER V

High Temperature InAs/GaAs Quantum Dot Spin Laser: Design and Fabrication

5.1 Introduction

The ability to control and/or modulate the output polarization of lasers [94] to electrically switch between orthogonal polarization states [95] would be useful for a host of applications including coherent detection systems, optical communications with enhanced bandwidth, secure communication and cryptography, and optical switching. The output polarization of semiconductor lasers is determined by the polarization properties of the active (gain) region and optical cavity. Vertical cavity surface emitting lasers (VCSELs) exhibit very poor polarization selectivity, stability and control. The in-plane fundamental transverse mode of these devices is randomly oriented [96], and polarization stability is usually obtained by introducing anisotropy in the gain curve of different competing polarization modes (gain anisotropy) [70] or by various schemes of mirror or cavity asymmetry [97]. Additionally, the polarization can be manipulated by changing the injected spin polarization without altering the carrier density. A constant carrier density eliminates temperature fluctuation and wavelength chirp. Hence information can be encoded onto both intensity as well as the polarization of the light thus effectively doubling of the bandwidth of communication channels. Besides finding

applications in lightwave communication network, these light sources can be used for the study of fibrous proteins, collagens and asymmetric photochemical reactions which are sensitive to circularly polarized light. Spin polarized coherent light sources also have lower power requirements as lasing is attained at lower carrier densities compared to conventional unpolarized lasers. Consequently, these advantages make it clear that spin lasers can be used for a wide range of applications including optical communications, biomedical research, low power optical switches and interconnects.

Polarization control in lasers may be obtained with injection and recombination of spin polarized carriers and the output polarization is related to the spin polarization of carriers in accordance with the relevant selection rules for the conservation of angular momentum in the gain medium [98]. Recombination of spin-up and spin-down electrons yields two coherently-coupled lasing modes, producing left- and right-circularly polarized light, respectively. In a non-magnetic laser, these two modes are pumped equally, producing two equal and in-phase circularly polarized modes which combine to form linearly polarized light. For 100% spin polarization of the injection current, a pure circularly polarized output is theoretically estimated, while for spin injection less than 100%, the circularly polarized light is superimposed on the linearly polarized emission to yield an elliptically polarized output. Additionally, the threshold current is reduced with injection of spin-polarized carriers, and for 100% spin polarized injection, the threshold is ideally reduced by a factor of 2. The first demonstration of an optically pumped spin-polarized vertical-cavity surface-emitting-laser (spin-VCSEL) was made by Rudolph et al. [48].The laser active region consisted of pseudomorphic InGaAs/GaAs quantum wells. The devices were operated at 6 K and both polarized light output and threshold

reduction were demonstrated. The same group have subsequently demonstrated a room temperature spin-VCSEL with GaAs/AlGaAs quantum wells [8]. *The first electrically injected spin-VCSEL, with InGaAs/GaAs quantum well gain medium, was demonstrated by Holub et al.* [70].The lasers were operated at 50 K and a maximum threshold current reduction of 11% and output degree of circular polarization of 23% were observed. Spin injection of electrons were accomplished with a Fe/AlGaAs Schottky tunnel diode.

For application of spin-polarized lasers, it is imperative that they are operated at high temperatures. At these temperatures, the electron spin relaxation time ts is determined by the D'yakonov-Perel' (DP) spin scattering process [100]. In InGaAs quantum wells, τ_s = 6 ps at room temperature [101], which is much lower than the radiative lifetime of 100 ps [102]. On the other hand, the discrete density of states and the spatial localization of carriers in quantum dots (QDs) inhibit both the DP and phonon scattering processes, which reduce the spin relaxation time and a weak temperature dependence of τ_s is expected [103]. The characteristics of an InAs/GaAs self-organized QD VCSEL is described here. The VCSEL is operated at 200 K. A maximum threshold current reduction of 14% and output optical polarization of 8% are measured in these devices.

5.2 Epitaxial Growth and Fabrication

Circular post spin-VCSELs, schematically shown in Fig. 5.1, were grown by MBE and fabricated using standard optical lithography, wet chemical etching, polymide planarization and passivation, contact and interconnect metallization, and dielectric electron beam evaporation techniques [70]. The InAs QDs density in the active region is 3×10^{10} cm^{-2}. The device mesa diameters varied from 15 µm to 30 µm. To form the spin

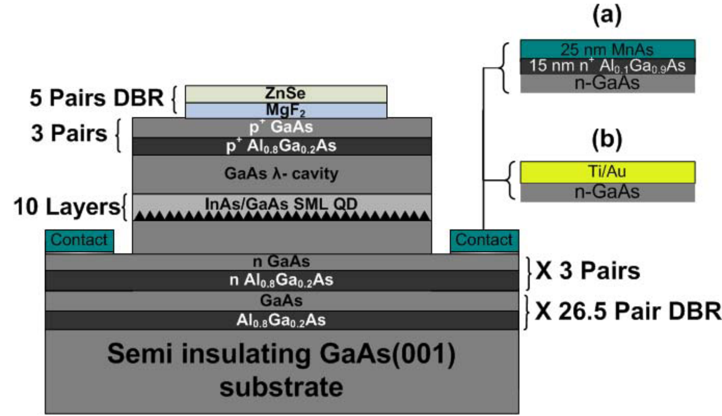

Fig. 5.1: Schematic cross section of an InAs QD spin-VCSEL heterostructure with (a) magnetic and (b) nonmagnetic n-contact grown by MBE.

polarized electron injector contact, MnAs/n^+-$Al_{0.1}Ga_{0.9}As$ Schottky barrier heterostructure was selectively regrown by MBE after a mesa definition. The mesa top surface and side walls were protected during re-growth by a ~2 μm thick SiO_2 layer which was formed by PECVD and subsequently patterned to reveal the annular n^+-GaAs contact layer. After a high temperature annealing for oxide removal from the GaAs surface, 15 nm n^+-$Al_{0.1}Ga_{0.9}As$ (N_D = 10^{19} cm^{-3}) and 25 nm MnAs were epitaxially grown at 630 and 250°C, respectively. Non-magnetic control VCSELs were also fabricated with the same mesa dimensions, but with a Ti/Au bilayer serving as the n-contact. The top DBR mirror was formed with 5 pairs of $ZnSe/MgF_2$ deposited by electron beam evaporation. A more detailed treatment on the fabrication aspects is presented in the appendix D.

5.3 Threshold Current Reduction and Output Circular Polarization

The quantum dot spin-VCSELs were mounted in a magneto-optical cryostat equipped with a 7T superconducting magnet. The devices were characterized at T = 200 K under continuous wave (CW) bias operation and in the Faraday geometry. Hence the

MnAs spin injector was magnetized along the hard axis. The chosen operating temperature of 200 K is low enough such that enough spin-polarized electrons would reach the QD active region and create a gain anisotropy. The lasing wavelength and the linewidth of the lasers were 983 nm and 0.28 nm, respectively. These values are consistent with the interband transition energy as determined from the low temperature photoluminescence measurements. The degree of circular polarization of the output, Π_c was analyzed using a photoelastic modulator (PEM) operating at 50 kHz and a Glan-Thompson linear polarizer, and the signal was detected and recorded with a silicon avalanche photodiode, low-noise preamplifier and by using lock-in techniques.

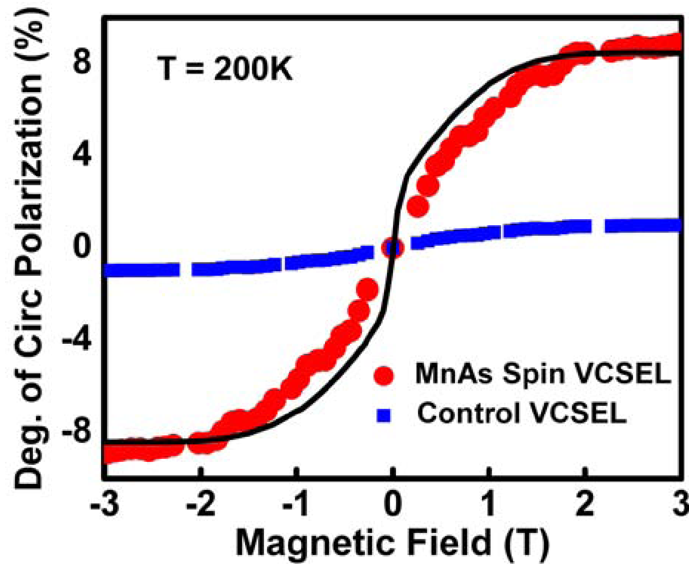

Fig. 5.2: Measured degree of output circular polarization vs magnetic field for a 15 μm mesa diameter MnAs spin-VCSEL (circle) and control VCSEL (square) measured at 200 K are shown. The spin-VCSEL polarization closely follows the out-of-plane magnetization curve for MnAs.

The measured values of Π_c as a function of magnetic field, for a device with mesa diameter 15 μm and biased at $1.05\times I_{th,0}$ (the threshold current for this device at zero magnetic field, $I_{th,0}$, is 13.8 mA), are shown in Fig. 5.2. The value of Π_c saturates at 8% at a magnetic field of ~2 T. On the other hand, Π_c for the control VCSEL, shown in the

Fig. 2, is $< 0.5\%$. Also shown in the figure is the room temperature out-of-plane magnetization of MnAs film epitaxially grown on GaAs. It is evident that Π_c closely tracks the magnetization of the MnAs layer and provides evidence of electron spin injection at the MnAs Schottky tunnel diode as the source of the observed output polarization.

In order to eliminate the possibility of the observed output polarization being attributed to stray field effects directly from the MnAs contact layer and Zeeman effect, we had previously characterized an identically designed VCSEL with an Fe contact layer formed on top of a ~0.45 μm non-magnetic ohmic contact metallization [4]. The measured Π_c was $< 1.5\%$. We also performed magneto-photoluminescence measurements on the same device with linearly polarized laser excitation and observed a negligible value of Π_c, which indicates that a parasitic contribution from magnetic circular dichorism is absent in these devices.

To measure the reduction in threshold current ΔI_{th}, due to injection of spin polarized carriers, magnetic field dependent optical power measurements were performed at 200 K in the Faraday geometry using a silicon photodiode and current pre-amplifier, with the devices under the CW operation. The measured light current characteristics and the reduction in I_{th} as a function of applied magnetic field are shown in Fig. 5.3. Again, the reduction saturates at ~2 T corresponding to the magnetization saturation of the MnAs contacts. No reduction in threshold current is observed for the non-magnetic quantum dot spin-VCSELs.

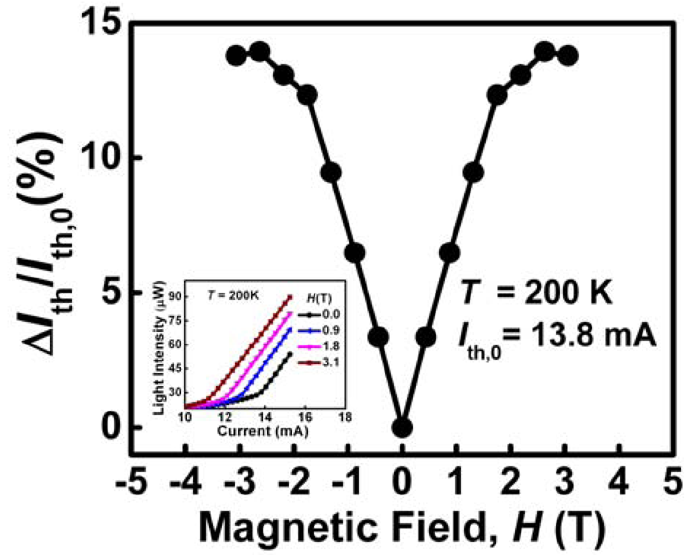

Fig. 5.3: Threshold current reduction vs magnetic field for a 15 μm mesa diameter MnAs spin-VCSEL measured at 200 K. Inset shows the measured light-current characteristics.

The reduction in the threshold current in the presence of a magnetic field is accompanied by an enhancement in light emission, $\Delta L = \eta_D \Delta I_{th}$, where ΔL is the differential quantum efficiency and ΔD is the slope efficiency. The measured emission enhancement as a function of injection current, for different values of magnetic field, is shown in Fig. 4(a).

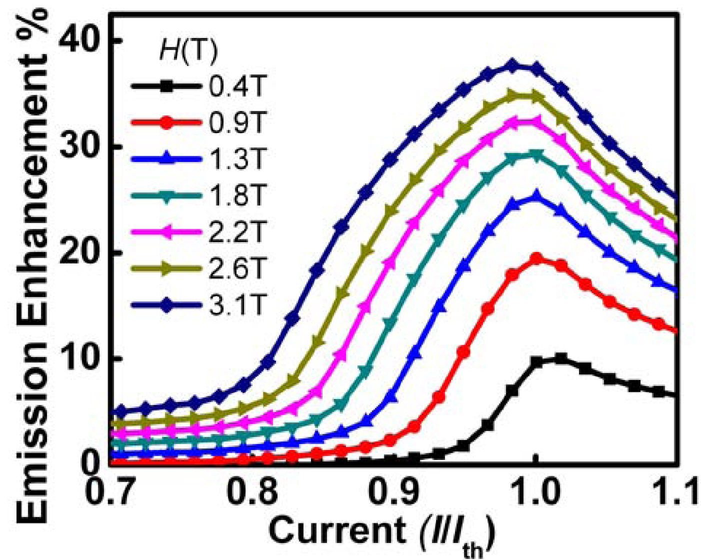

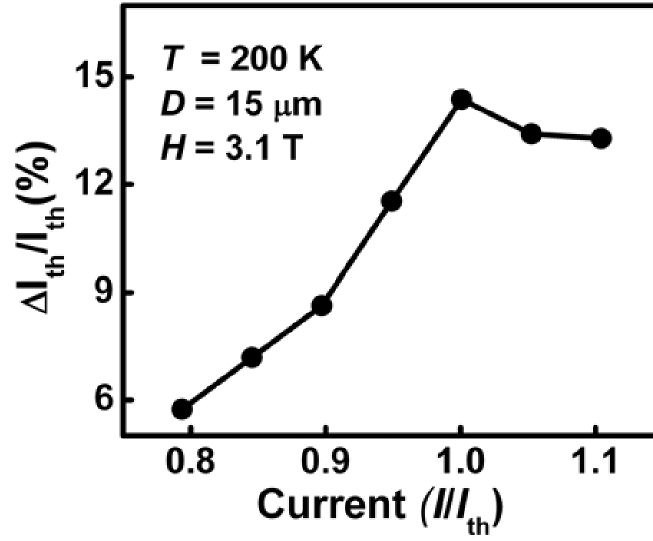

Fig. 5.4: (a) Emission intensity enhancement vs normalized current (I/I_{th}) measured for different magnetic fields; (b) variation in threshold current reduction ($\Delta I_{th}/I_{th}$) vs normalizedcurrent (I/I_{th}) measured at a magnetic field of 3.1T.

A peak emission enhancement of 37% is recorded at 3.1 T. When biased near threshold, a small difference in spin polarization of the injected carriers can result in a large difference in the intensities of the two circular polarizations due to gain anisotropy, provided the spin relaxation time is greater than the carrier lifetime. The gain anisotropy and the resulting polarization anisotropy will decrease with increasing injection and eventually disappear with the onset of gain saturation. This explains the observed peaking of the emission enhancement at $I/I_{th} \approx 1$ in Fig. 5.4(a) and an identical trend of the threshold current reduction shown in Fig. 5.4(b). Due to gain anisotropy, the threshold current of the favored mode is reduced at the expense of the mode with opposite polarization whose threshold increases.

5.4 Modeling of Quantum Dot spin-VCSEL

The dynamic properties of the QD spin-VCSEL were analyzed with the spin po-larized carrier-photon coupled rate equations including non-linear gain compression effects [48,

104]. The device and material parameters used, for operation at 200 K, are given in

Parameter	Symbol	Value
Differential gain	$\partial g/\partial n$	4.5×10^{-14} cm^2
Gain compression factor	ϵ	4.5×10^{-17} cm^{-3}
Rad. recombination coeff	B_{sp}	9.4×10^{-10} cm^{3}s^{-1}
Auger recombination coeff	C	1.5×10^{-27} cm^{6}s^{-1}
Carrier capture time	τ_{cap}	45 ps
Spin-flip time in barrier	$\tau_{s,b}$	50 ps
Spin-flip time in QD	τ_{sf}	75 ps
Photon group velocity	v_g	8.7×10^9 cm s^{-1}
Optical confinement factor	Γ	0.024
Spontaneous emission factor	β	6×10^{-4}
Photon lifetime	τ_{ph}	1.25 ps

Table 5.1: Quantum dot parameters at 200 K used to analyze spin laser performance characteristics[105-108]

Table 5.1. The transparency current density in the cavity is varied to fit the measured threshold currents. The calculated variation of threshold current reduction with injection current spin polarization is shown in Fig. 5.5(a). Thus for the measured I/I_{th} = 14% the required P_{spin} = 15%, corresponding to which the spin polarization in the QD active region and barriers at $I = I_{th}$ are calculated to be 5.8% and 8.5%, respectively. This is the point of maximum gain anisotropy and it may be noted that the output polarization of 8% is larger than the QD spin polarization of 5.8%. As the spin injection current is increased, the density of both spin polarizations approaches n_{th}, the gain anisotropy is reduced, and the QD spin polarization approaches zero and the measured output polarization of the laser is determined by the barrier polarization of 8.5% (Fig. 5.5(b)). It is to be noted that the dominant depolarization for the spin-polarized carriers occur during the transport process,when the spin polarization decreases from 31% [11] at the spin injector to 5.8%

at the QDs.

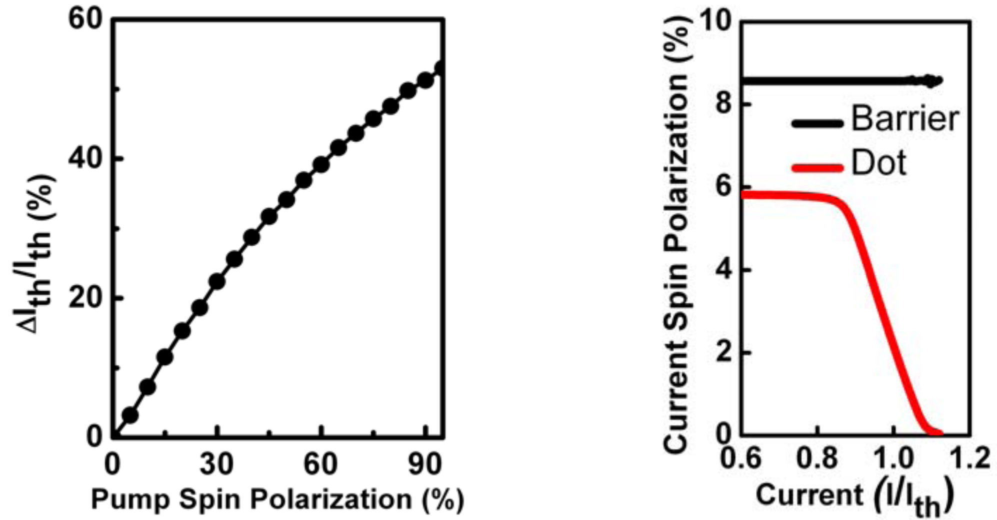

Fig. 5.5: (a) Calculated threshold current reduction vs pump-current spin polarization for spin relaxation time τ_{sf} = 75 ps; (b) calculated variation of the spin polarization values in the barrier and in the QDs vs normalized current.

5.5 Conclusion

We have demonstrated a QD spin-VCSEL for the first time. The device can be operated at 200 K. To operate the device at room temperature, the mesa diameter of the devices need to be reduced to 2-3 μm in order to decrease the effects of spin relaxation due to transport from the contacts to active region, which is perfectly feasible. It would also be desirable to increase P_{spin}. The latter is primarily determined by the spin polarization in the ferromagnetic spin injector. For MnAs the spin polarization is ~31% [11] and for Fe, the value is 45% . With these values it would be difficult to attain the theoretical maximum current reduction of 50%.

CHAPTER VI

Electrical Modulation of Polarization and Gain Anisotropy of a Spin Laser

6.1 Introduction

The selection rules for the conservation of angular momentum directly relate the spin orientation of the carriers transported to the active region to the polarization of photons emitted upon their radiative recombination [109]. While these relations hold for spontaneous emission, such as in a spin light-emitting diode (LED), they do not reflect the output polarization in a spin laser [99] due to the non-linear dynamics and the spin polarization in the gain medium (active region), which gives rise to a large gain anisotropy at biases near threshold. As a result, the output polarization can be much larger than the spin polarization of the injected carriers. This is intuitively understood and has also been observed by us in quantum well spin lasers [70], but the exact magnitude of the output polarization and the parameters and dynamics upon which it depends have been hitherto unknown. In the present project we have derived the analytical form of the output polarization Π_C , threshold current $I_{th}(H)$, and the threshold current reduction $\Delta I_{th} / I_{th,0}$, as determined by gain anisotropy. In particular, we have highlighted the role of the diffusive transport of spin-polarized electrons from the ferromagnetic contact to the active region. The calculated values of these parameters are in excellent agreement with values obtained from the first measurement of electrical

modulation of a InAs/GaAs QD spin-VCSEL with MnAs ferromagnetic contacts, schematically shown in Fig. 6.1. The QD active region allows high temperature operation since the spin relaxation time in the dots, limited by the DP spin scattering process [15], is enhanced due to carrier confinement. The present study provides a comprehensive insight to the operation and characteristics of an electrically injected spin-polarized semiconductor laser.

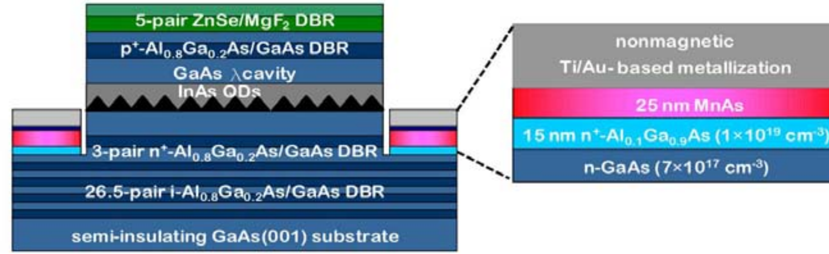

Fig. 6.1: Heterostructure of GaAs-based spin-VCSEL grown by molecular beam epitaxy. The active (gain) region consists of 10 periods of self-organized InAs/GaAs quantum dotsplaced in a GaAs - λcavity. The top DBR mirror consists of 5 pairs of $ZnSe/MgF_2$ deposited by PVD. The ferromagnetic $MnAs/Al_{0.1}Ga_{0.9}As$ tunnel injector contact is regrown selectively on GaAs after a mesa-etch stop, as shown in the figure.

5.2 Analysis of laser characteristics from spin polarized laser rate equations:

An important aspect which has to be taken into account in any spin laser, edge-or surface-emitting, is the diffusive spin transport from the ferromagnetic contact to the active region. Spin polarization at a distance x from the ferromagnetic contact at x = 0 (see Fig. 6.2) is governed by [91],

$$\frac{\partial^2 \left(N^+ - N^-\right)}{\partial x^2} = \frac{N^+ - N^-}{\lambda_{sf}^2} \tag{6.1}$$

where λ_{sf} is the spin diffusion length in the transport medium and $N^+(x)$ and $N^-(x)$ are the spin-up and spin-down carrier densities at any point x. Drift of spin-polarized carriers is neglected since the doping densities in the transport region is relatively high

(5×10^{17} cm^{-3}) [91]. These functions are valid from the contact up to the barrier (cavity) region i.e. $x = x_1$. For x>x1 the polarization is governed by the laser parameters. Also, we know that the ferromagnetic contact polarization is given by,

$$P_{contact} = \Pi(x=0) = \frac{N^+(x=0) - N^-(x=0)}{N^+(x=0) + N^-(x=0)} \tag{6.2}$$

The value of $P_{contact}$ is known from a measurement of the out-of-plane magnetization of the MnAs contact as a function of H [110], the spin dependent density of states of MnAs [86] and the spin injection efficiency at the MnAs/GaAs tunnel barrier [11].

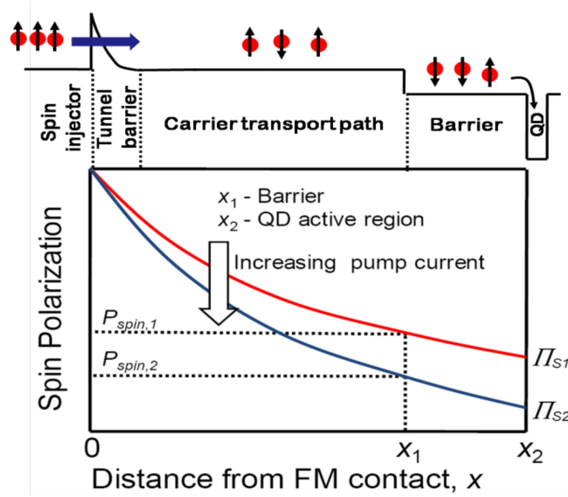

Fig. 6.2: Schematic representation of the variation of carriers spin polarization with distance from ferromagnetic contact (MnAs) in VCSEL in accordance with the spin diffusion equation. The barrier (cavity) is at distance x_1 and the quantum dot region is at distance x_2. The spin polarization decreases with increasing pump current. In the barrier and quantum dots the polarization decreases from $P_{spin,1}$ to $P_{spin,2}$ and Π_{S1} to Π_{S2}, respectively.

The dynamics of carrier and photon densities in semiconductor lasers are governed by the coupled rate equations as outlined in Ref. [99, 112] and also in appendix B. The non-linear gain in the active region is generally expressed in terms of the gain compression factor ϵ as $g(n,S) = dg/dn\,(n-n_{tr})/(1+\epsilon S)$, where n $(=n^+ + n^-)$ is the total (sum of spin-up and spin-down electrons) carrier density in the active region.

Since the laser is operated very close to threshold where the gain anisotropy is a maximum, $\epsilon S << 1$, hence $g(n,S) \cong g(n)$.

The laser rate equations and the spin diffusion equation are solved with the objective of obtaining analytical forms of the threshold current and output polarization as a function of applied magnetic field. In solving these equations, we define a set of intermediate parameters. These are the spin polarization at any point $x(0 \leq x \leq x_1)$, $\Pi(x)$, the quantum dot spin polarization, $\Pi_s = (n^+ - n^-)/(n^+ - n^-)$, and the average barrier polarization, $\Pi_{s,b} = (n_b^+ - n_b^-)/(n_b^+ - n_b^-)$, where $n_b^{\pm}$ is the spin-up (spin-down) carrier density at the barrier. On the other hand the degree of circular polarization of the output, $\Pi_c = (S^+ - S^-)/(S^+ + S^-)$, and the light output $L = S^+ + S^-$ are measurable quantities, where $S^{\pm}$ are the density of the right- and left-circularly polarized photons. By solving the steady state laser rate equations [105] it can be easily shown that the barrier polarization and the output circular polarization are related to the carrier density through,

$$\frac{V_b}{V_{QD}} \frac{n_b}{\tau_{cap}} = v_g \left[g\left(n^+\right)S^- + g\left(n^-\right)S^+ \right] + B_{sp} n^2 + C n^3 \tag{6.3}$$

$$\frac{V_b}{V_{QD}} \frac{n_b^+ - n_b^-}{\tau_{cap}} = v_g \left[g\left(n^+\right)S^- - g\left(n^-\right)S^+ \right] + \left(n^+ - n^-\right)\left(B_{sp} n + C n^2 + \frac{2}{\tau_s} \right) \tag{6.4}$$

Similarly the output circular polarization is related to the carrier density through,

$$v_g \left[g\left(n^+\right)S^- + g\left(n^-\right)S^+ \right] = \frac{S}{\Gamma \tau_{ph}} - \beta B_{sp} n^2 \tag{6.5}$$

$$v_g \left[g\left(n^+\right)S^- - g\left(n^-\right)S^+ \right] = -\frac{S^+ - S^-}{\Gamma \tau_{ph}} - \beta B_{sp} n \left(n^+ - n^-\right) \tag{6.6}$$

Where $S^{\pm}$ are given by,

$$S^{\pm} = \frac{\Gamma \beta B_{sp} n^{\mp} n}{1/\tau_{ph} - \Gamma v_g g\left(n^{\mp}\right)} \tag{6.7}$$

Combining Eqns. 6.3 and 6.5, and noting that the pump current $I_{pump}=I_{th}$ when $n=n_{th}/(1 + \Pi_S)$ we get,

$$I_{th}(H) = qV_{QD}\left[\frac{1}{\Gamma}\frac{S_{th}}{\tau_{ph}} + \frac{B_{sp} n_{th}^2 (1-\beta)}{\left(1+\Pi_s(H)\right)^2} + \frac{C n_{th}^3}{\left(1+\Pi_s(H)\right)^3}\right] \tag{6.8}$$

where S_{th} is the photon density at threshold. It is found that the cumulative contribution from the terms containing threshold photon density (S_{th}) and the Auger recombination coefficient (C) in Eqn. (6.8) are less than 10 % of the contribution from the term having radiative recombination coefficient (B_{sp}), under all possible operating conditions of a spin laser. Hence, knowing $I_{th,0}$, the percentage threshold current reduction, $\Delta I_{th}(H)/I_{th,0}$ is reduced to a simplified form given by,

$$\frac{\Delta I_{th}(H)}{I_{th,0}} \cong \frac{\Pi_s(\Pi_s + 2)}{(1+\Pi_s)^2} \tag{6.9}$$

It is of interest to note that this parameter is determined exclusively by Π_S.

Similarly, the output polarization (as obtained by using Eqn. 6.7 and Eqns. 6.5 and 6.6) is given by,

$$\frac{\Pi_c\left(H, I_{pump}\right)}{\Pi_s} = -\frac{1+\Gamma v_g \tau_{ph}\frac{dg}{dn} n_{tr}}{1+\Gamma v_g \tau_{ph}\frac{dg}{dn} n_{tr} - \Gamma v_g \tau_{ph}\frac{dg}{dn} n_{th}(1-\Pi_s)} \tag{6.10}$$

We also define a gain anisotropy parameter,

$$g_A\left(H, I_{pump}\right) = \frac{g\left(n^+\right)}{g\left(n^-\right)} \cong \frac{1+\Pi_s}{1-\Pi_s} \tag{6.11}$$

The parameters ($\Delta I_{th}/I_{th,0}$), g_A, Π_c, and $d\Pi_c/d(I_{th}/I_{th,0})$ are plotted against injection current and applied magnetic field and are depicted in Figs. 6.3 and 6.4. The device and material parameters used and obtained from our own work and from recent reports [17,108,113].

6.3 Device characterization and modeling

Measurements have been carried out on spin-polarized quantum dot VCSELs. In particular we have measured the reduction in the threshold current due to spin injection of electrons and the electrical modulation of the output polarization. We also choose an operating temperature of 200 K, which is low enough to allow enough spin polarized electrons to reach the QD active region from the MnAs Schottky tunnel contact. The laser heterostructure shown in Fig. 6.1 is grown by MBE.

The lasers were mounted in a magneto-optical cryostat for measurements, which were done in the Faraday geometry. All measurements reported here were carried out on 15 μm diameter VCSELs at the design temperature of 200 K where no offset exists between the photoluminescence gain peak and the distributed Bragg reflector (DBR) reflectivity peak and hence lasing with the minimum threshold current is obtained. This

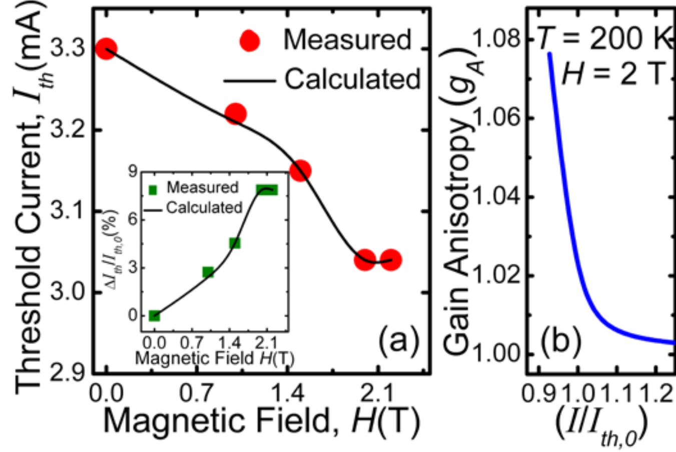

Fig. 6.3 : Data from 15 μm diameter InAs/GaAs QD spin VCSEL at 200 K: (a) calculated and measured reduction of threshold current with magnetic field applied perpendicular (hard axis) to the plane of the MnAs contact. The inset shows the calculated and measured percentage reduction of threshold current with field; (b) calculated variation of gain anisotropy parameter, as defined in Eqn. (6.9) with normalized pump current.

temperature is carefully chosen such that a large number of spin-polarized carriers can still reach the QD active region. The current biasing to the lasers was in the continuous wave mode. The measured reduction and percentage reduction ($\Delta I_{th}/I_{th,0}$) of the threshold current with application of magnetic field are plotted in Fig. 6.3(a) and its inset and there is good agreement with the calculated values of the respective parameters. A maximum threshold current reduction ($\Delta I_{th}/I_{th,0}$) of ~8% is measured at H = 2.1 T, at which field the saturation of the out-of-plane magnetization of MnAs contact also occurs. No threshold reduction is observed for the non-magnetic VCSEL. The calculated variation of gain anisotropy with current (Fig. 6.3(b)) indicates that spin related phenomena are operative only for lasers biased near threshold, $I_{th,0}$. It may be noted that the gain anisotropy (g_A) is largest just below threshold. This is easily understood by considering injection of spin polarized carriers in a laser biased slightly below threshold, $I_{th,0}$. An application of magnetic field results in injection of spin polarized carriers which can preferentially enhance the gain of one polarization mode

above threshold gain, while the gain of the other polarization mode still remains sub-threshold, resulting in a large gain anisotropy and reduction in the threshold current. As the injection is increased, the difference in peak gain of the two polarization modes will decrease and the gain anisotropy will also steadily decrease. The maximum value of g_A attainable with ferromagnetic MnAs spin injector is ~ 2, under the ideal conditions of negligible spin flip during transport of spin-polarized carriers to the active region. An increase in spin injection efficiency will lead to higher gain anisotropy (Eq. 6.11) and hence enhanced threshold reduction and output circular polarization.

6.4 Polarization modulation in a spin laser under continuous wave excitation

The output polarization characteristics of the spin laser are discussed next. For a fixed bias current, the measured value of Π_c as a function of the applied magnetic field follows the measured out-of-plane magnetization of the MnAs contact very closely. In comparison the observed polarization of the non-magnetic VCSEL is negligible. The modulation of the output polarization Π_c with bias current was measured at different saturation magnetic fields and the data are shown in Fig. 6.4(a). As the pump current reaches threshold, the carrier concentration of the polarized lasing mode with higher gain (say S^+) becomes clamped at n_{th}. Further increase in pump current will increase the carrier concentration of the mode with lower gain (S^-), till n_{th} is reached for this mode also and the mode will lase. It is easily seen that the spin polarization in the QD active region will steadily decrease as the injection increases beyond the point where

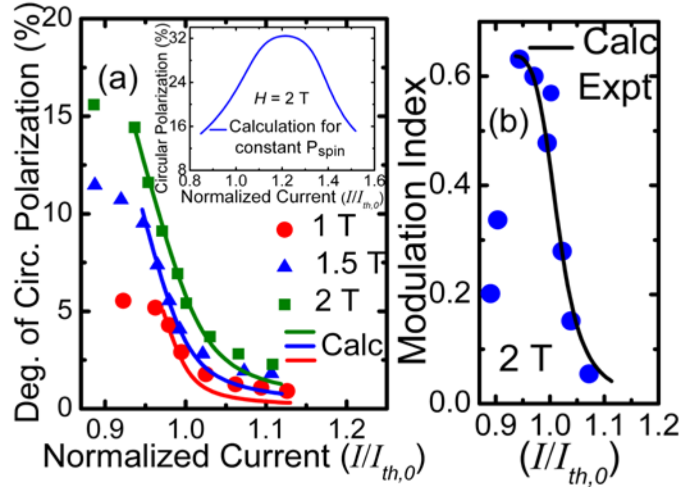

Fig. 6.4: (a) Calculated and measured modulation of output circular polarization of InAs/GaAs QD spin VCSEL as a function of normalized pump current at different magnetic fields. The inset shows calculated polarization for *constant* pump current spin polarization, instead of the variation of P_{spin} shown in Fig. 5.2; (b) measured modulation index versus pump current. The calculated values are shown for currents at and above threshold.

the first threshold (for S^+) is reached. Intuitively, it is expected that in the injection regime between the thresholds for S^+ and S^-, the output polarization will steadily increase and then decrease after the threshold for S^- is crossed. However, considering the transport of injected spin-polarized carriers from the ferromagnetic contact to the active region by spin diffusion, and the steady decrease of the spin polarization in the active (gain) region after the threshold of S^+ is reached, the pump spin polarization P_{spin} also decreases, as illustrated in Fig. 6.2. This leads to a decrease in output circular polarization as soon as the pump current increases beyond the threshold (for S^+). Thus the intuitive picture of the variation of output polarization would be valid only if diffusive transport of injected carriers is neglected and P_{spin} is held constant (inset to Fig. 6.4(a)). This is the first demonstration of electrical modulation of the output polarization of a semiconductor laser. We define a modulation index as $\Delta\Pi_c/\Delta(I/I_{th})$ and this parameter is plotted in Fig. 6.4(b) as a function of normalized current along with

the calculated data. The index goes through a maximum value of 0.6 at $I/I_{th,0} \cong 1$ and decreases rapidly for high bias currents due to significant reduction of gain anisotropy in this range.

6.5 Conclusion

In conclusion, we have studied the effects of spin induced gain anisotropy in spin-polarized lasers. Analytic expressions have been derived for threshold current reduction, output polarization, and the gain anisotropy parameter, taking into account the diffusion of spin-polarized carriers from the ferromagnetic contact to the active region and the spin-coupled laser rate equations. The validity of the derivations is endorsed by excellent agreement of calculated values with those obtained from measurements made with spin VCSELs having InAs/GaAs self-organized QDs.

CHAPTER VII

Transient Characteristics of an Electrically Injected Quantum Dot Spin Laser: The Case for 100 % Output Polarization

7.1 Introduction

There is a dynamic exchange of energy between carriers – electrons and holes – and photons in a resonant cavity whenever the carrier population is perturbed by external means. The latter can be in the form of electrical injection or optical excitation [114]. Thus, in a semiconductor laser cavity a damped oscillatory optical output is observed. This is accompanied by a similar perturbation in the carrier density, usually of smaller amplitude. The system behaves as a tuned circuit and a resonant condition can be achieved in the system transfer function, which is the ratio of the light output to the injected carrier density, at some characteristic oscillation frequency.[115] These relaxation oscillations, which exist for several nanoseconds and are related to the spontaneous emission lifetime, set an upper limit to the modulation frequency of a laser. In fact, the frequency of the relaxation oscillations at the tail end, where small-signal conditions are prevalent, approximates the resonant frequency for small signal modulation of the laser. It is generally understood that a laser restores steady state in the duration of the oscillations. In a semiconductor laser, relaxation oscillations give rise to deleterious effects such as linewidth enhancement and chirp due to the periodic

modification of the refractive index in the active (gain) region by the carrier concentration modulation [114].

The spin polarization of recombining electrons and holes generally do not play a role in the operation of a conventional laser. Radiative recombination of spin-up and spin-down carriers in the active region of any semiconductor light source produces left- and right-circularly polarized light, respectively [50,116,117]. In a conventional laser, these two polarization modes are pumped equally, from equal injection of spin-up and spin-down carriers. The two equal and in-phase circularly polarized modes combine to form linearly polarized emission. Preferential injection of spin polarized carriers lead to emission of circularly of elliptically polarized light via the selection rules [109] for radiative recombination. While the steady–state characteristics of optically and electrically injected spin-polarized laser have been studied in detail, by theory and experiment, [69,70,99,110,118] the effect of a net spin polarization of carriers in the active region on the dynamic or transient, properties have not been fully examined, or exploited. In a recent publication, Lee et.al [119] report a theoretical study of the small signal modulation properties of the dominant or favored circularly polarized mode of a spin laser, from which it is evident that the modulation bandwidth is enhanced. This is easily understood, since a spin laser attains threshold with a smaller density of injected carriers. Of more importance and interest are the large signal modulation characteristics of the spin laser, the temporal evolution of the relaxation oscillations of *both* polarization modes and the temporal evolution of the net output polarization. In this work we have examined the role of injected carriers with a net spin polarization on the large- and small-signal modulation characteristics of a semiconductor laser. In particular, we have

investigated the region of operation near threshold of the laser, where large gain anisotropy of the two polarization modes exists. The calculated transient characteristics clearly show temporally separated relaxation oscillations for the two polarization modes and predict an increase in the small signal modulation bandwidth. *The simulations also predict that an output circular polarization of 100% can be obtained, under certain biasing conditions, irrespective of the spin polarization of the injected carriers.* This fact is of great practical importance since the spin polarization of injected carriers in the active region of a spin laser at high temperatures is usually in the range of 5-6%. Experimental verification is provided by performing measurements on a InAs/GaAs quantum dot VCSEL in which spin polarized electrons are injected into the quantum dots by a MnAs ferromagnetic contact. The spin-VCSEL operates at 230 K and a maximum output polarization of 55 % is measured. These characteristics make a spin laser a very practical and useful device for a host of applications including study of biological structures, fibrous proteins and pharmacological properties of drugs, reconfigurable optical interconnects and secure communication. [120,121]

7.2 Calculated small- and large-signal modulation characteristics of a spin laser

The dynamic characteristics of a spin laser and preferential emission of polarized photons are described by the spin dependent carrier-photon coupled rate equations [99]:

$$\frac{dn^{\pm}}{dt} = J^{\pm} - v_g g^{\pm}(n^{\pm}, S)S^{\mp} - \frac{n^{\pm} - n^{\mp}}{\tau_s} - \frac{n^{\pm}}{\tau_r} \tag{7.1}$$

$$\frac{dS^{\pm}}{dt} = \Gamma v_g g^{\mp}(n^{\mp}, S)S^{\pm} - \frac{S^{\pm}}{\tau_{ph}} + \beta\Gamma\frac{n^{\mp}}{\tau_s} \tag{7.2}$$

Where $J^{\pm}$ is is the current density in the two modes, $g^{\pm}$ is the spin dependent gain, $n^{\pm}$ is

the electron density in the active region, $S^{\pm}$ is the photon carrier density, τ_s is the spin relaxation time in the active region, β is the spontaneous emission factor, Γ is the optical confinement factor, τ_{ph} is the photon lifetime, τ_r is the radiative recombination time constant, and v_g is the photon group velocity. The current densities in the two modes can be expressed as, $J^{\pm} = (J/2)(1 \pm \Pi_J)$, where Π_J is the current spin polarization and J is the total current density. The total carrier density n in the active region and photon density S are given by ($n^+ + n^-$) and ($S^+ + S^-$), respectively. To determine the small signal response, we assume $J = J_0 + \Delta J, n^{\pm} = n_0^{\pm} + \Delta n^{\pm}$, and $S^{\pm} = S_0^{\pm} + \Delta S^{\pm}$ where J_0, $n_0^{\pm}$, and $S_0^{\pm}$ are their corresponding equilibrium values. The large signal response of the laser and the temporal evolution of the photon and carrier densities are obtained from the rate equations by using numerical techniques. [114] The transfer function $\partial S^{\pm}/\partial J$ for the small-signal modulation response and the resonance frequency $f_R^{\pm}$ of the response are also derived. The latter is expressed as:

$$f_R^+ = \frac{1}{2\pi}\left\{\frac{v_g g_0 S^+}{\tau_{ph}}[(1+\Pi_S)(1-\epsilon S^+)] + \frac{1}{\tau_r}\left[\frac{1}{\tau_{ph}} - 2\Gamma(1-\beta)g_0(1-2\epsilon S^+)(n-n_{tr})\right]\right\}^{1/2} \quad (7.3)$$

where g_0 is the differential gain, Π_s is the spin polarization in the active region, n_{tr} is the transparency carrier density and ϵ is the gain compression factor. A simplified analytical form of the resonance frequency is given by:

$$f_R^+ = \frac{1}{2\pi}\left[\frac{v_g g_0 S^+}{\tau_{ph}}(1+\Pi_S)\right]^{\frac{1}{2}} \quad (7.4)$$

under the assumption that the gain compression factor is small and $v_g g_0 S^+ \tau_r \gg 1$ at high injection. Figures 7,1(a), (b), and (c) show the time evolution of photon density (S^-, S^+), electron density (n^+, n^-) and output circular polarization, respectively, when a large-

signal step current bias $(J > J_T^+, J_T^-)$ is applied having Π_J = 0.5 and τ_s = 1 ns. The transient response from a conventional laser is also shown for comparison. An important distinction between the spin laser and the conventional laser is that one of the modes (S^+) starts lasing earlier than the other mode (S^-). This is evident from the relaxation oscillations of the two modes. The transients in the conventional laser lie in between the two modes of the spin laser. The time dependent electron densities show similar trends as shown in Fig. 7.1(b). The time delay between the lasing of the two modes is ~0.5 ns in this case. This delay is due to the fact that injected spin-polarized carriers fill one spin sub-band (n^- in this case) faster than the other sub-band (n^+) and the resultant gain anisotropy facilitates the n^- mode to reach threshold faster. The threshold carrier density for each mode is exactly half ($n_{th}/2$) of that of a conventional laser (n_{th}). Another important aspect that emerges from the dynamic characteristics is that the total carrier density ($n = n^+ + n^-$) continues to increase even after the device has started lasing for $n = n_{th,spin} = n_{th}/(1 + \Pi_s)$ which is the threshold carrier density for a spin laser. In contrast, the carrier density gets clamped at n_{th} in a conventional laser. It is interesting to note in Fig. 1(c) that the output circular polarization gradually reaches a peak value close to 100% when only the favored polarization mode is lasing. Oscillations of the output circular polarization is initiated only after the less-favored mode starts lasing and the output circular polarization eventually reaches the steady state value. This effect is also present for smaller values of τ_s, as will be evident later. The steady state carrier density of a spin laser for $(J > J_T^+, J_T^-)$ is the same as that of a conventional laser (Fig. 7.1(b)), but is smaller than that of conventional laser for $(J_T^+ < J < J_T^-)$.

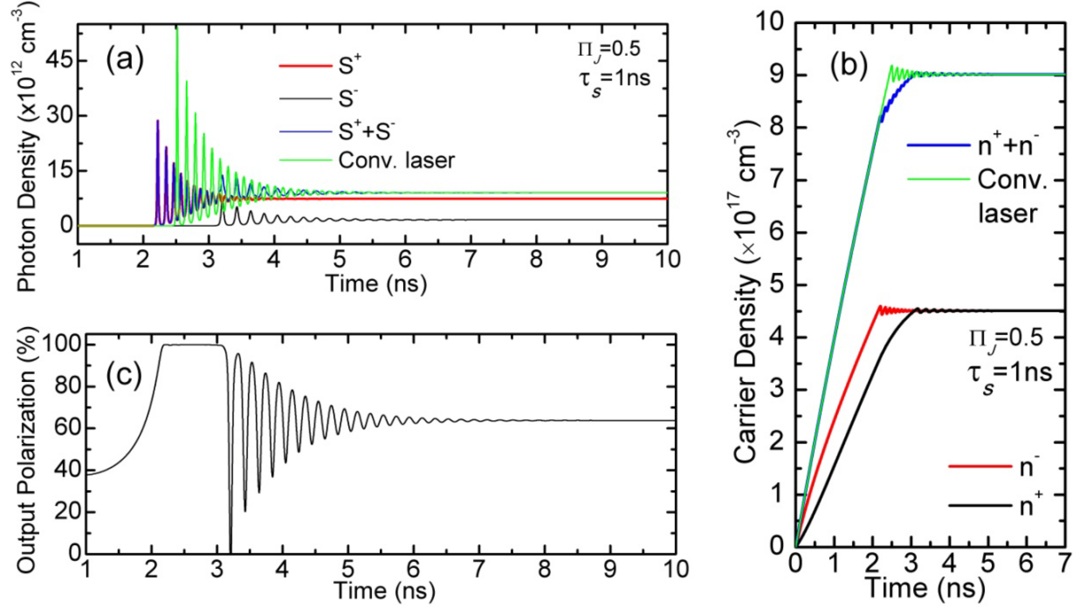

Fig. 7.1: Calculated large-signal modulation characteristics of spin laser showing temporal variation and relaxation oscillations of (a) photon density, (b) electron density, and (c) output polarization. The output polarization of the spin laser reaches a value of 100% when the favored mode only is lasing and the relaxation oscillations are initiated after the less favored mode attains threshold.

The relaxation oscillations gradually decay in a laser. The oscillation frequency at the latter part of the transient approaches the small signal modulation resonance frequency given by Eqn. 7.4, which is approximately the modulation bandwidth of the system. Figure 7.2 shows values of the upper limit of the relaxation oscillation frequency plotted as a function of current bias for the two and S^-. The amplitude for S decreases very rapidly for f > f_R^- as S^- accumulates phase at a much faster rate and the 3 dB frequency f_{-3dB}^{spin} for the spin-laser is reached earlier than all of f_{-3dB}^-,

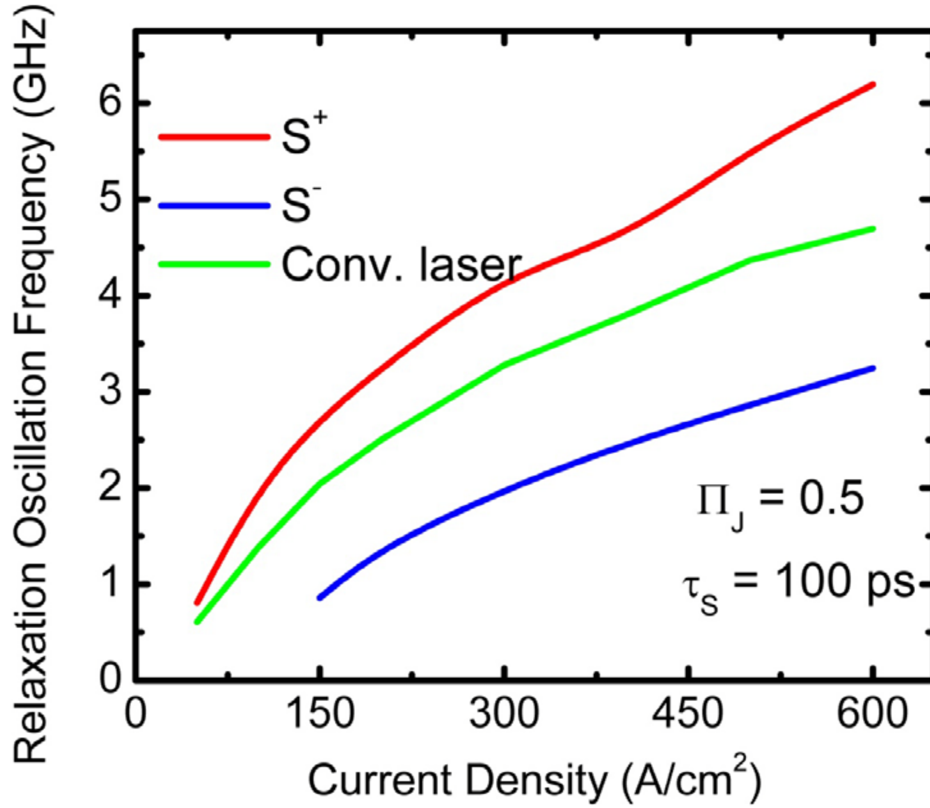

Fig. 7.2 Calculated upper limit of relaxation oscillation frequency as a function of current density for the conventional and spin lasers. The oscillation frequency increases with increasing bias for both the polarization modes. The oscillation frequency of the conventional laser always lies in between the two modes of the spin laser**.**

polarization modes in a spin laser and that in a conventional laser. The value of τ_s is

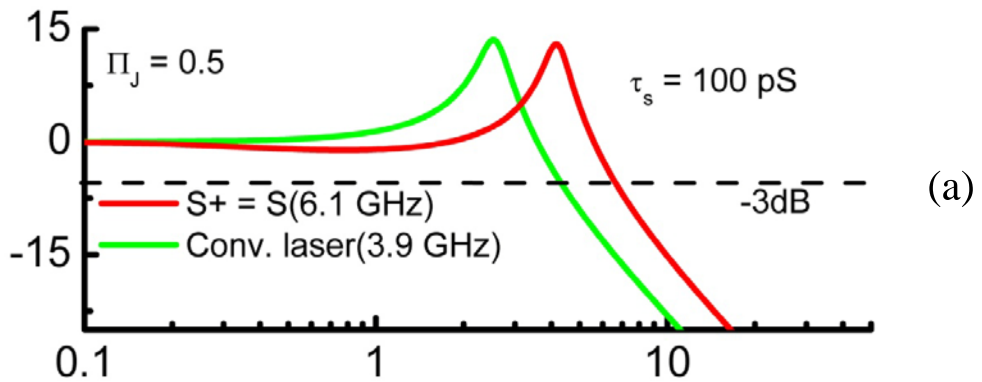

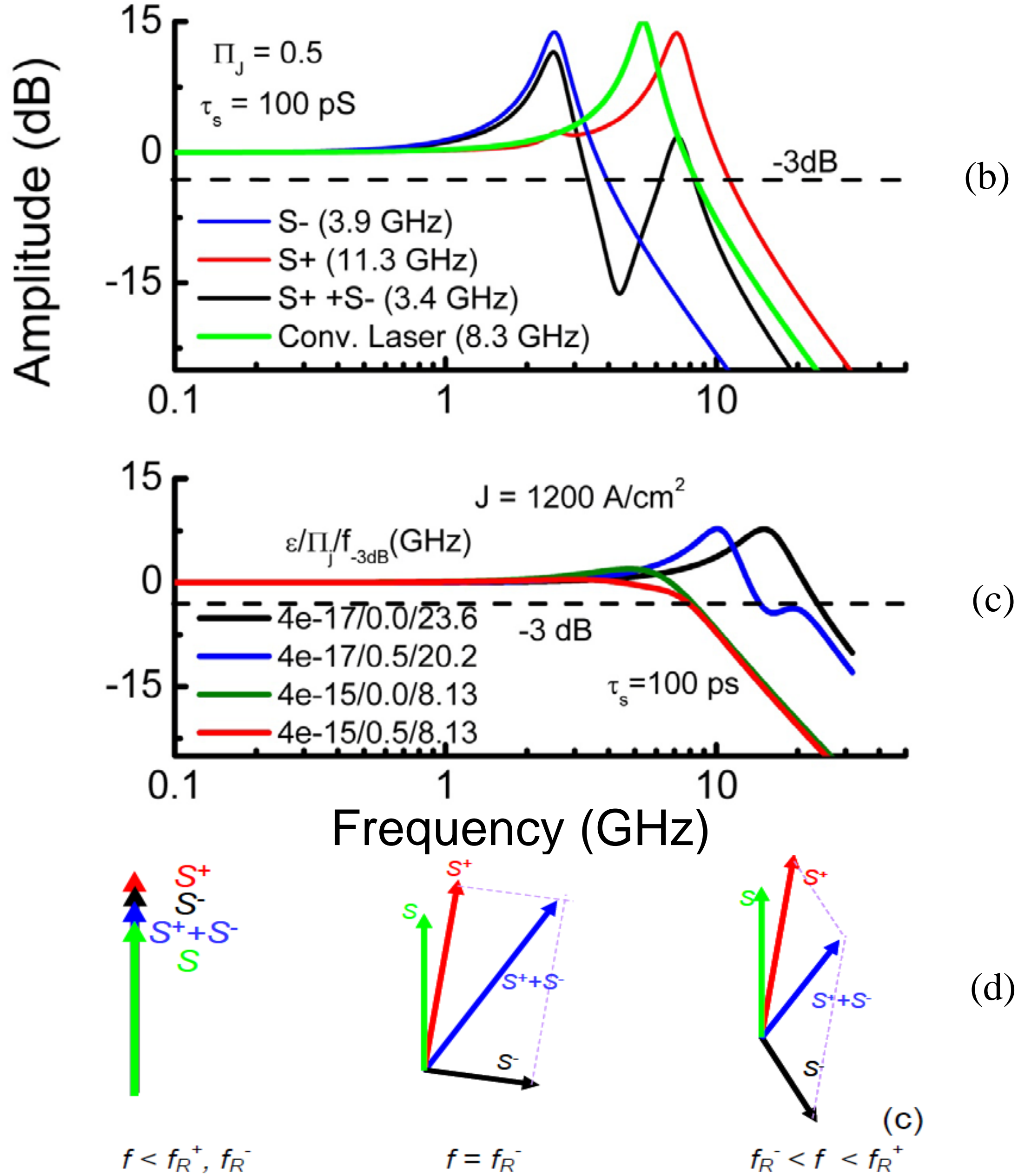

Fig. 7.3 Calculated small-signal frequency response of the spin laser when: (a) the favored polarization mode, and (b) both polarization modes are lasing. The response from a conventional laser is also shown for comparison. The spin laser bandwidth increases when only one mode is lasing and decreases when both the modes are lasing; (c) effect of gain compression (ε) on modulation bandwidth calculated for the spin and conventional lasers; (d) phasor diagram of the polarization modes.

assumed to be 100 ps, which is approximately the value in InAs quantum dots, incorporated in our experimental spin VCSELs, at room temperature. [103] It is interesting to note that the polarization mode with higher gain has a much larger

relaxation oscillation frequency than that of the other mode and also that of the conventional laser. Since a larger relaxation oscillation frequency corresponds to a larger resonance frequency for small-signal modulation given by Eqn. 7.4, spin-lasers are expected to have larger modulation bandwidth (f_{-3dB}) than conventional lasers. This is expected since a spin laser reaches threshold with a smaller density of injected carriers. To determine the impact of the temporal separation of f_R^+ and f_R^- on spin laser bandwidth, we have calculated the small signal frequency response for S^+, S^-, S ($=S^+ + S^-$), and that of a conventional laser for τ_s=100 ps. Figure 3(a) shows the frequency response when only the favored mode S^+ is lasing ($J_T^+ < J < J_T^-$ and $S^- = 0$). It can be seen that the bandwidth is considerably larger for the spin laser. Figure 7.3(b) shows the frequency response when both the modes are lasing ($J > J_T^+, J_T^-$). It is interesting to note that the spin laser bandwidth (f_{-3dB}^{spin}) is smaller than the bandwidth for individual polarization modes (f_{-3dB}^+ and f_{-3dB}^-) and for the conventional laser (f_{-3dB}^{conv}). This can be understood from the phasor diagram in Fig. 3(d). The phase contribution from a mode beyond the resonant frequency is greater than 90°. As the frequency exceeds f_R^- , the phase for S^- is greater than 90°, while the phase for S^+ is still close to zero. The resultant amplitude for S (vector sum of S^- and S^+) is therefore smaller than both S^+ f_{-3dB}^+, and f_{-3dB}. However, it is evident that the spin laser has another passband at a higher frequency (similar to a bandpass filter) where it responds to the signal frequency efficiently. The3 dB frequency of a spin laser is therefore a complex function of both injected current spin polarization and spin relaxation time. Gain compression of a laser generally results from hot carrier effects and carrier leakage from the active region. [122] We have examined the effect of gain compression (ϵ) on the small-signal modulation bandwidth of spin-polarized and

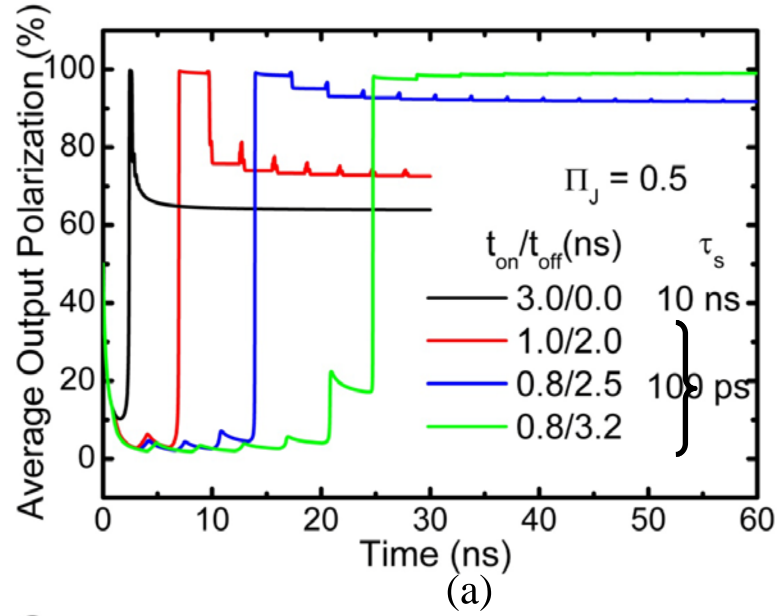

(a)

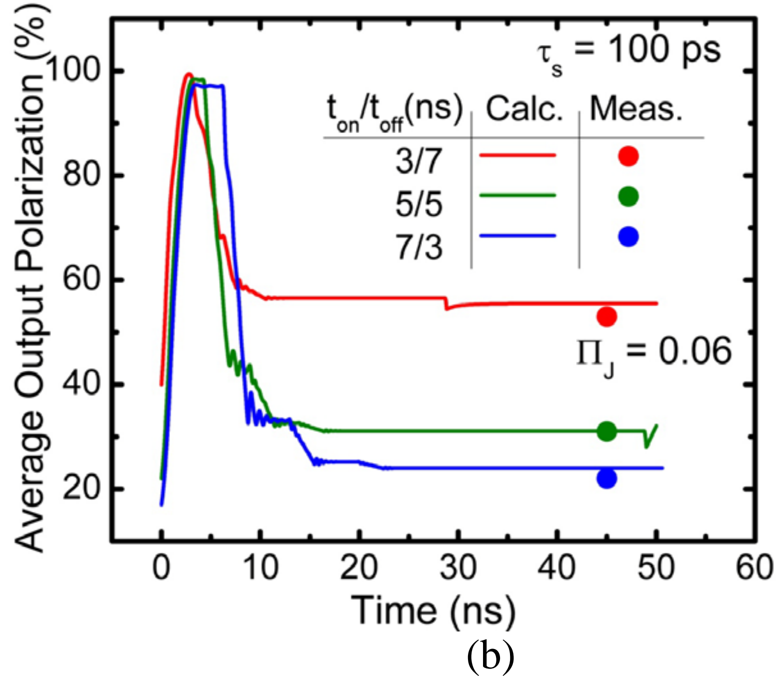

(b)

Fig. 7.4 (a) Time-averaged output circular polarization (Π_c) as a function of time for various t_{on} and t_{off} of an ideal square pulse bias with zero rise and fall times. Π_c can be tuned in a wide range by varying the ON and OFF period. The output circular polarization can be made very high independent of the spin relaxation time in the active region by suitably tuning the pulse width and duty cycle of the bias current; (b) Π_c calculated and measured for a spin laser with a pulse current bias having finite identical rise and fall times (1.5 ns). The simulations correspond to a quantum dot spin polarization of 6 % estimated for a 10 μm diameter VCSEL measured at 230 K. The dotted lines correspond to the time averaged output polarizations measured in these devices.

conventional lasers. The results are shown in Fig. 3(c). The presence of a large gain compression increases the damping of the system and the resonant peak amplitude tends

to decrease and finally disappears. The effect of gain compression may be slightly more adverse in a spin laser compared to that in a conventional laser, as indicated by the calculated bandwidths. This effect is dependent on the spin-relaxation time constant τ_s, current spin-polarization Π_J, and the operating bias.

7.3 Output polarization

Perhaps the most interesting aspect of the present analysis is the fact that the temporal separation in transient characteristics between the two polarization modes (S^+ and S^-) in response to a large-signal input and the corresponding difference in resonance frequencies can be used to generate light with very large output circular polarization. The less favored mode (S^-) in the transient characteristics can be suppressed by pulsing the input signal with appropriate ON (t_{on}) and OFF (t_{off}) periods. Figure 4(a) shows the calculated average output circular polarization (Π_c) as a function of time for various values of t_{on} and t_{off} of a perfect square pulse bias and assuming Π_J = 0.5. Π_c is ~64% for continuous-wave (t_{off} = 0) operation with large τ_s = 10 ns. To emphasize the fact that a large output circular polarization can indeed be obtained even with very small τ_s, the rest of the simulations are done with τ_s = 100 ps. A smaller t_{on} ensures that only the favored mode (S^+) is lasing and all the light is coming from this mode, while the other mode (S^-) is barely excited. Therefore the average output circular polarization is very high. A relatively large t_{off} also ensures that the carriers in the less favored mode (n^+) do not build up to $n_{th}/2$ and therefore facilitates a large value of Π_c. Figure 4(b) shows similar calculated data for Π_J = 0.05, τ_s=100 ps and the input square pulse has a rise and fall time of 1.5 ns. These parameters are chosen for comparison with experimental results to be

described next. The general nature of the temporal evolution of polarization is very similar. The most important point to realize is that it should be possible to achieve very large degrees of output polarization even if the spin polarization Π_s in the active region is small. This can greatly relax the requirements of high spin polarization in the ferromagnet injector, high spin injection efficiency at the ferromagnet-semiconductor junction, and large spin diffusion length in the transport region between the contact and the active region. The results also imply that large output polarization can be obtained at high temperatures where τ_s might be small.

7.4 Experimental results : Characteristics of quantum dot spin VCSELs

In order to verify the predicted transient characteristics and in particular the output polarization, we have made measurements on InAs/GaAs quantum dot (QD) spin VCSELs. The spatial localization of carriers in the QDs inhibit the dominant D'yakonov-Perel (DP) spin scattering process [15] and photon scattering which reduce the spin lifetime. A spin lifetime τ_s= 100 ps is predicted in InAs QDs at 300 K. The growth and fabrication of spin VCSELs have been described by us [110]. Very briefly, circular post spin VCSELs were fabricated by standard lithography, etching and metallization techniques after molecular beam epitaxial growth of the laser heterostructure. The top-emitting device consist of a GaAs/$Al_{0.8}Ga_{0.2}As$ lower distributed Bragg reflector (DBR) mirror, a λ-sized GaAs cavity in the center of which is placed 8 periods of InAs/GaAs QDs and a top DBR consisting of 5 periods of $ZnSe/MgF_2$. The MnAs/$Al_{0.1}Ga_{0.9}As$ Schottky tunnel spin injection contact [86] is selectively regrown and fabricated around the cavity mesa on top of silicon doped GaAs layer of the bottom DBR. The contact

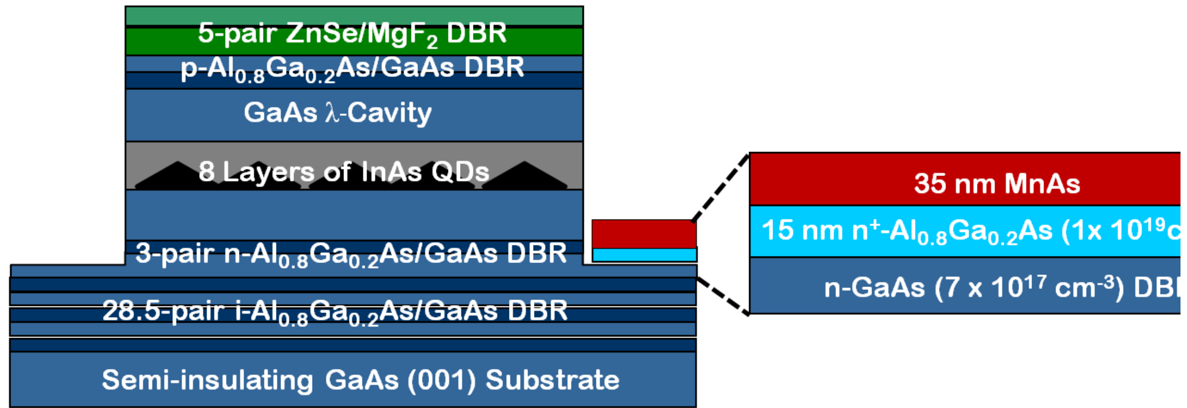

Fig. 7.5 Spin VCSEL heterostructure grown by molecular beam epitaxy. The $MnAs/Al_{0.1}Ga_{0.9}As$ spin injector is formed by epitaxial regrowth.

injects spin polarized electrons which travel to the active region QDs, where they recombine with unpolarized holes injected from a p-ohmic contact placed above the cavity region.[123] The mesa diameter varies from 10 - 30 µm and for a 10 µm diameter device, the average distance travelled by the injected spin polarized electrons is ~ 4 µm. The injected spin polarization at the 25 nm MnAs/ 15 nm $Al_{0.1}Ga_{0.9}As$ contact is 32%, determined from independent measurements on lateral GaAs spin valves. [11] The spin polarization in the active region at or near lasing threshold is estimated to be of the order of 5 - 6%.[69] The laser heterostructure is schematically shown in Fig.5. Control devices with non-magnetic ohmic contacts were also fabricated.

Since the Curie temperature of type A MnAs is ~ 300 K, the spin laser was designed to operate at 230 K, where the magnetization of MnAs is still reasonably large. [124] Also, since the easy axis of MnAs is in the in-plane [110] direction, measurements were made in a magneto-optical cryostat with the applied magnetic field in the Faraday geometry, for which the direction of light output and spin quantization axis are coincident. The spin VCSEL output spectrum exhibits a transition of linewidth 0.31 nm with peak at 1.17 µm for a bias of $I = 1.05\ I_{th,0}$. The light-current characteristics of the spin VCSEL as a

function of B and the corresponding threshold current reduction are shown in Fig. 6(a). The threshold current for no applied magnetic field is $I_{th,0}$ = 10.5 mA for the 10 μm diameter device. Under steady state dc bias conditions, a maximum threshold current reduction of 4.4 % at 2 Tesla is measured as shown in the inset. The reduction saturates at this value of applied magnetic field. The measured output polarization for dc bias tracks the magnetization curve for MnAs and saturates at a value of 12.5 % at 2 Tesla. The control devices and magnetophotoluminesence measurements on the devices show an output polarization of ~1%. These experimental data confirm that the observed output polarization at 230 K is due to spin injection alone.

The output polarization measured under with B = 2 T under pulsed bias conditions are shown in Fig. 7.6(b). Large-signal modulation measurements were made with a square wave input pulse having a rise and fall times of 1.5 ns, the laser being switched from $I < I_{th,0}$ to $I = I_{th,2T}$ during the t_{on} interval. The output polarization was analyzed using a photoelastic modulator operating at 50 kHz and a Glan–Thompson linear polarizer, and the signal was detected and recorded with a silicon avalanche photodiode and low-noise preamplifier using digital lock-in techniques. It is clear that very large output polarization values, up to 55% are measured for small values of t_{on}. It should be noted that the measured value corresponds to the time-averaged output polarization, as the response time of the silicon photodiode and that of the photoelastic modulator are much larger than the values of t_{on}. A larger output polarization (>55%) could not be measured because of the limitation of the pulse generator used. For large values of t_{on} for which both polarization modes are above the threshold, the output polarization tends to a

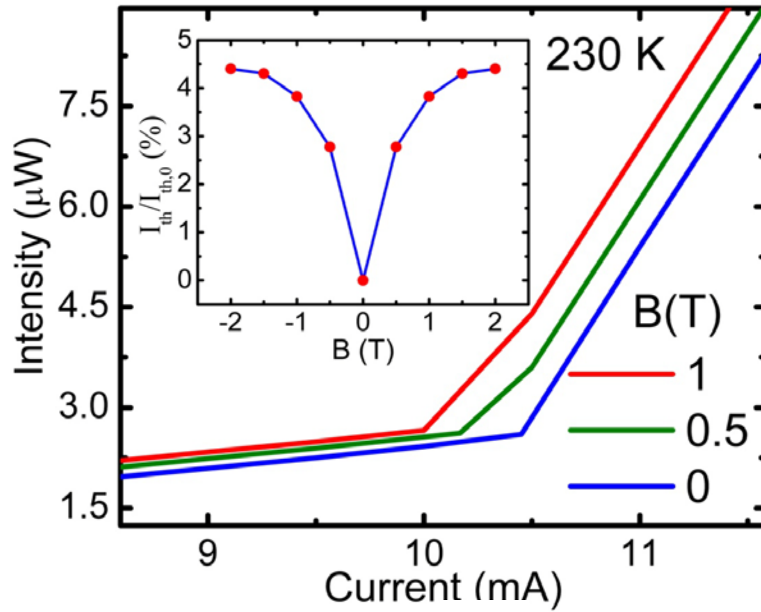

(a)

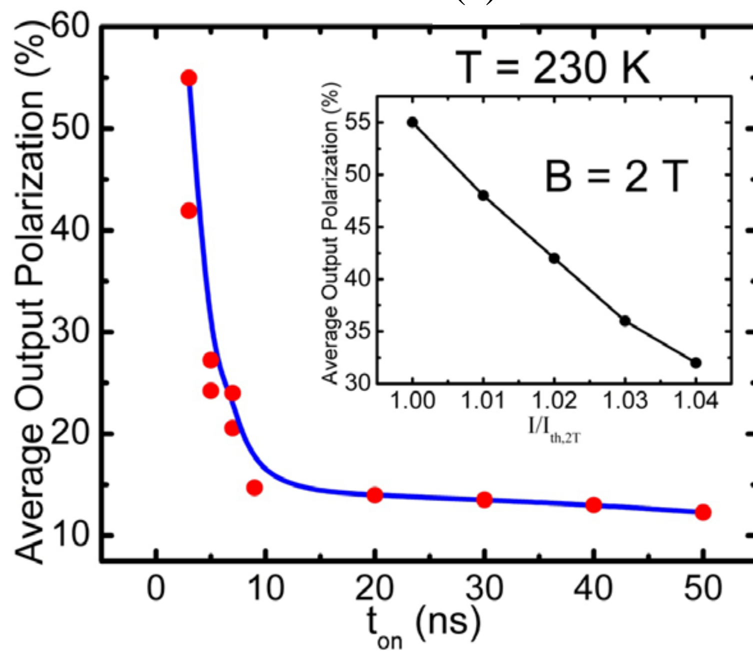

(b)

Fig. 7.6 (a) The measured dc light-current characteristics for a 10 μm mesa diameter spin-VCSEL measured at 230 K in the Faraday geometry. Inset shows threshold current reduction vs applied magnetic field; (b) Measured degree of time-average output circular polarization vs t_{on} of the square pulse bias with rise and fall times of 1.5 ns. The inset shows the value of peak output polarization measured for different values of current bias.

steady-state value of 12.5 %. The inset of Fig. 7.6(b) shows the variation of the output polarization with increasing bias. The decrease in polarization is due to increasing

population of the less favored polarization mode. The experimental data for small t_{on} are plotted with the theoretically calculated polarizations in Fig. 4(b) and there is a very good agreement. It is important to realize that an output polarization of 55 % is measured with a spin polarization of ~6 % in the QDs. Finally it may be noted that operation at room temperature and without an applied magnetic field can be obtained with Fe/Tb-MgO [125] or FeCoB-MgO [126] spin injectors and polarization upto 100% can be measured for small t_{on} and high-speed biasing and circuitry.

7.5 Conclusion

In conclusion, we have studied the transient properties of a spin laser, together with the small- and large-signal modulation properties. It is evident that the spin laser performance is optimized when only one polarization mode (with higher gain) is lasing. The laser responds faster to large-signal inputs, as the relaxation oscillations decay in a shorter period, the small signal modulation bandwidth is larger and the output polarization can be very large (upto 100 %) independent of the spin polarization of cavities in the active region. The latter is verified experimentally with InAs/GaAs quantum dot spin VCSELs operating at 230 K. A maximum polarization of 55 % is measured.

TABLE 7.1: Laser parameters used to study dynamic characteristics of spin laser [17,105,108,113]

Parameter	Symbol	Value
Differential Gain	$\partial g/\partial n$	4×10^{-14} cm^{2}
Gain Compression factor	ϵ	4×10^{-17} cm^{-3}
Rad. recombination time constant	τ_r	10 ns
Photon group velocity	v_g	8.9×10^{9} cm.s^{-1}
Optical confinement factor	Γ	0.024
Spontaneous emission factor	β	6×10^{-4}
Photon lifetime	τ_{ph}	1.15 ps
Current spin polarization	Π_J	0.5
Transparency carrier density	n_{tr}	4×10^{17} cm^{-3}

CHAPTER VIII

Conclusions and Suggestions for Future Work

8.1 Summary of the completed work

In this study we have realized several spin based electronic and optoelectronic devices working at high temperatures. The work done on spin polarized lasers is also potentially technologically important in that it shows how these devices can overcome the limitations of imperfectly polarized electron injection in semiconductors, a well-known problem. Notable results and conclusions from the study are highlighted below.

8.1.1 Spin polarized lasers

A spin-polarized vertical cavity surface emitting laser, with InAs/GaAs self-organized quantum dots as the active gain media, has been fabricated and characterized. Electron spin injection is achieved via a MnAs/GaAs Schottky tunnel contact. The laser is operated at 200 K and, at this temperature, the degree of circular polarization in the output is 8% and the maximum threshold current reduction is 14%. These effects are not observed in identical control devices with nonmagnetic contacts. The effects of spin-induced gain anisotropy on output polarization and threshold current reduction of these lasers have been studied. Analytical forms of laser parameters are derived by considering diffusive transport from the spin injector to the active region. The calculated values of the parameter are in excellent agreement with values obtained from measurements made at 200 K. Electrical modulation of the output polarization of the laser is demonstrated with a

peak modulation index of 0.6. The high frequency dynamics of spin polarized carriers and photons in a spin laser have also been studied. It is seen that the transient response of the device obtained from the rate equations is characterized by two sets of relaxation oscillations in the carrier and photon distributions corresponding to the two polarization modes. Consequently two distinct resonant peaks are observed in the calculated small-signal modulation response. The calculated transient characteristics indicate that the best results are obtained from a spin laser when only the favored polarization mode, with lower threshold, is operational. Under this condition the small-signal modulation bandwidth is higher than that in a conventional laser, the threshold current is lower and the output polarization can be 100% with appropriate bias conditions, independent of the spin polarization of carriers in the active region. A time-averaged output polarization of 55% is measured with an active region spin polarization of 5-6%. The experimental results are in good agreement with calculated data. The results confirm that 100% output polarization can be obtained, independent of the degree of injected spin polarization in a high speed laser with appropriate biasing conditions.

8.1.2 Spin polarized electronic devices

The control of magnetoresistance of a lateral spin valve with bias applied to a gate placed outside the channel region is demonstrated. The spin valve channel consists of an $InAs/In_{0.53}Ga_{0.47}As/In_{0.52}Al_{0.48}As$ two-dimensional electron gas lattice matched to (001) InP. The polarizer and analyzer contacts are made with 35 nm type B $MnAs/In_{0.52}Al_{0.48}As$ Schottky tunnel barriers. The magnetoresistance changes from 0.14% to 4% at 10 K in a device in which the spin transport is in the direction of magnetization of the polarizer and analyzer contacts.

We have demonstrated room temperature electrical spin injection and detection in degenerately p-doped GaAs in a vertical heterostructure using valence band electron tunneling (VBET). Spin relaxation in these devices is dominated by the Bir-Aranov-Pikus mechanism, which is relatively insensitive to temperature. The spin injection and detection efficiencies are mostly determined by the ferromagnetic contact polarization and spin independent hopping transport at the ferromagnet/semiconductor interface. VBET in a p-doped semiconductor embedded in a vertical structure can be an important process for the realization of high temperature semiconductor spintronic devices.

8.2 Suggestions for future work

8.2.1 Spin injectors with out-of-plane easy axis of magnetization

Development of spin injectors with magnetization in the out-of-plane direction with large spin injection efficiencies and then integrating them with VCSELs would be major step towards the realization of a commercial spin polarized coherent light source. Significant research has been done in developing such spin injectors, a few worth mentioning are Fe/Tb-MgO or FeCoB-MgO. Spin polarized light emitting diodes have already been realized at room temperatures using these spin injectors.The next step would be to investigate the possibility of integrating these spin injectors in order to realize quantum dot spin-VCSELs working at temperatures higher than 230 K.

8.2.2 High temperature spin polarized Fabry-Perot lasers

Although significant progress has been achieved in realizing spin polarized surface emitting coherent light sources, spin-based edge emitting lasers have not been reported till date. This genre of devices have a distinct advantage over its surface emitting

counterpart because of the following reasons:

1. Spin transport length can be controlled and can be as small as 500 nm. This would ensure higher working temperatures of these devices compared to the VCSELs as designing and realizing small diameter surface emitting lasers are technologically very challenging.
2. The device would work in the absence of any applied magnetic field with the MnAs based spin injector contacts.

A schematic of InP based wide quantum well spin polarized laser heterostructure is shown in fig. 8.1.

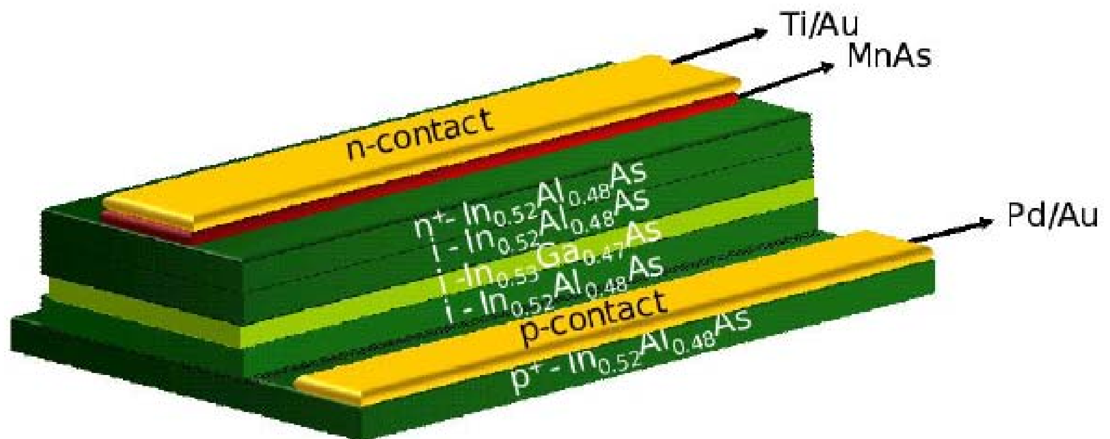

Fig. 8.1: Heterostructure of the proposed InP based wide quantum well edge emitting laser.

Towards this end it is worth mentioning that we have already realized conventional InP based edge emitting lasers with quantum well active region. The L-I characteristics is shown in fig. 8.2.

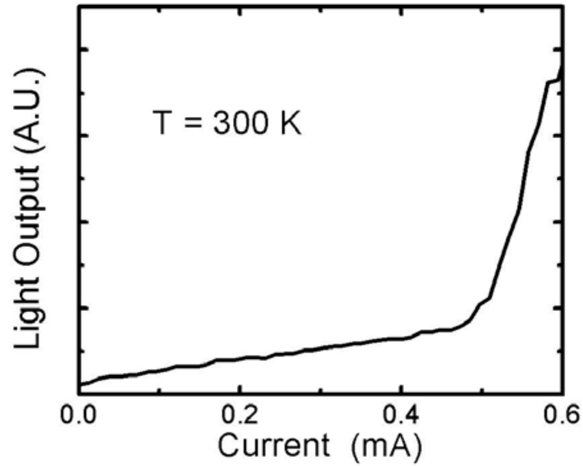

Fig. 8.2: Light-output characteristics of a InP based multi-quantum well conventional edge emitting laser.

In order to realize lasers with fast polarization switching capabilities the spin injector pads can be specially designed as shown in fig 8.3. The different pad sizes would ensure distinctly different coercivities. By building suitable drive circuitry these pads can be excited as required to obtain high speed polarization modulation and switching in these devices in the absence of any externally applied magnetic field.

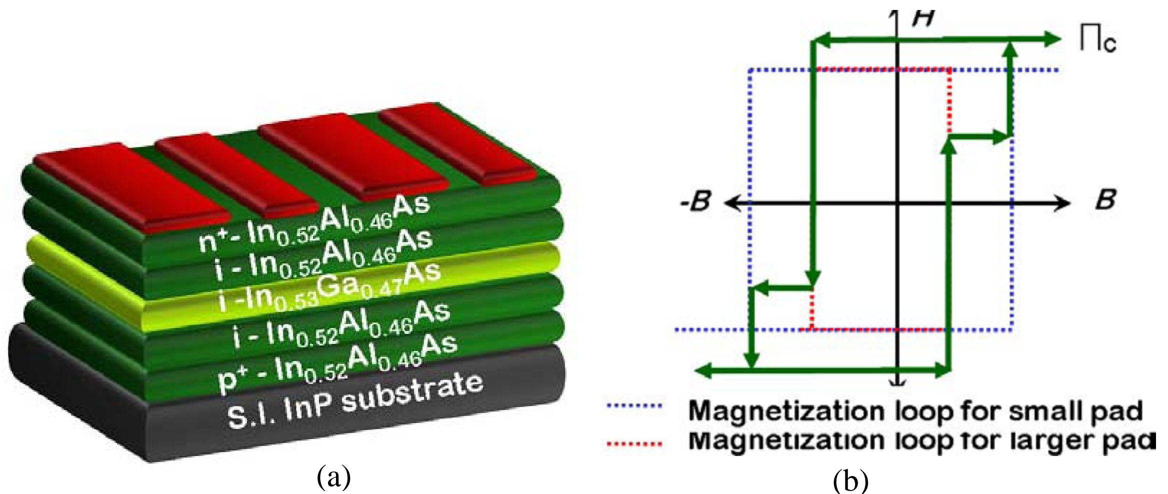

Fig. 8.3: (a) Proposed spin-edge emitting laser with distinct spin injector pad sizes in order to realize fast polarization switching; (b) hysteresis characteristics of the ferromagnetic spin injector pads.

8.2.3 Vertical spin transistors

A three terminal device is a fundamental block in order to realize an all-spin logic device. Since the first proposal of the Datta-Das spin transistor, research in this field has been driven primarily towards its realization. We have seen in chapter 3 that the primary drawback of such a device is its small modulation response and cryogenic working temperature. In order to overcome both these issues we propose a three teminal device in the vertical geometry. A schematic heterostructure of this device is shown in fig.8.4.

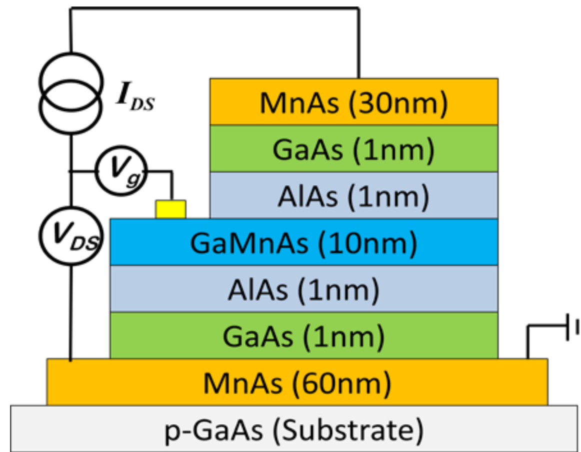

Fig. 8.4: Schematic showing the heterostructure of the proposed spin based three terminal transistor.

The top and the bottom MnAs layers act as the emitter and the collector terminals. The base terminal is a non-magnetic Ti/Au contact sitting on the degenerately p-doped GaAs layer. Some of the preliminary device results from the device are shown in fig 8.5.

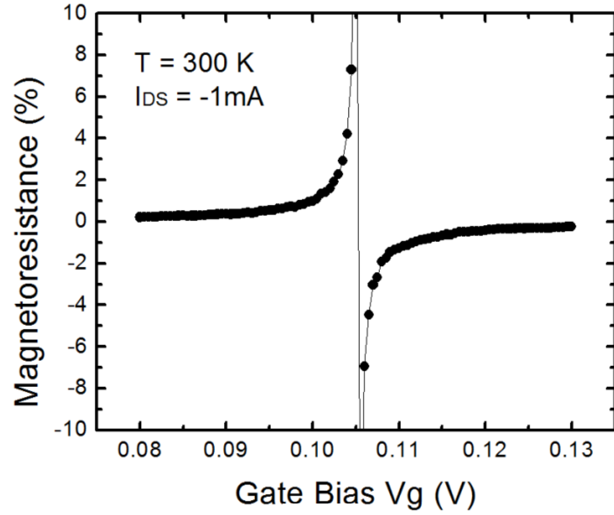

(a)

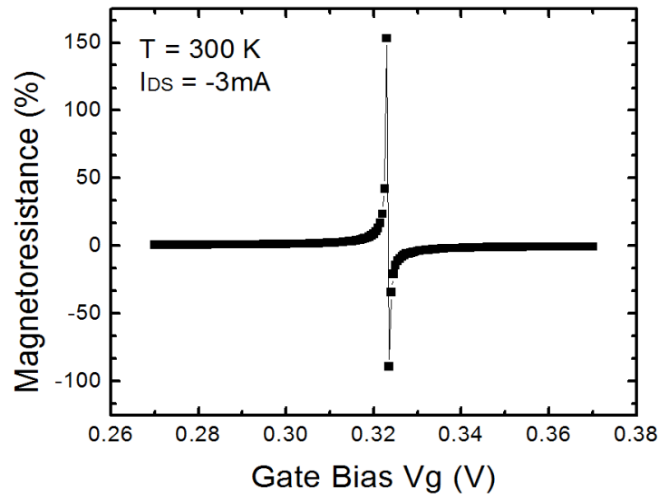

(b)

Fig. 8.5: Magnetoresistance versus gate bias characteristics measured at room temperature for an applied constant drain to source current bias of (a) I_{ds} = -1mA and; (b) I_{ds} = -3mA.

The magnitude of the response obtained in these devices at room temperature is very promising. Currently we are working towards designing a simple logic circuit using this three terminal device. Options for cascading two such devices in series are also being investigated.

APPENDIX A

Calculation of Modulation Bandwidth of a Spin-polarized Laser

Laser rate equations for the carrier density fluctuations in an electrically injected spin polarized laser are given by:

$$\frac{dn^+}{dt} = \frac{J^+}{qd} - v_g g^+(n^+, S^-)S^- - \frac{n^+ - n^-}{\tau_s} - R_{sp}^+ \qquad A.1$$

$$\frac{dn^-}{dt} = \frac{J^-}{qd} - v_g g^-(n^-, S^+)S^+ - \frac{n^- - n^+}{\tau_s} - R_{sp}^- \qquad A.2$$

Upon adding these equations we get:

$$\frac{dn}{dt} = \frac{J}{qd} - v_g(g^+S^- + g^-S^+) - \left(R_{sp}^+ + R_{sp}^-\right) \qquad A.3$$

Laser rate equations for the photon density fluctuations in an electrically injected spin polarized laser are given by:

$$\frac{dS^+}{dt} = \Gamma v_g g^-(n^-, S^+)S^+ - \frac{S^+}{\tau_{ph}} + \beta\Gamma R_{sp}^- \qquad A.4$$

$$\frac{dS^-}{dt} = \Gamma v_g g^+(n^+, S^-)S^- - \frac{S^-}{\tau_{ph}} + \beta\Gamma R_{sp}^+ \qquad A.5$$

Upon adding these equations we obtain

$$\frac{dS}{dt} = \Gamma v_g(g^+S^- + g^-S^+) - \frac{S}{\tau_{ph}} + \beta\Gamma\left(R_{sp}^+ + R_{sp}^-\right) \qquad A.6$$

Here the gain corresponding to the different degrees of circular polarizations can be

expressed as

$$g^{+} = \frac{g_0(n^{+} - n_{tr})}{(1 + \epsilon S)} \; and \; g^{-} = \frac{g_0(n^{-} - n_{tr})}{(1 + \epsilon S)}$$

From these relations upon simplification we obtain

$$g^{+}S^{-} + g^{-}S^{+} = \frac{g_0}{(1 + \epsilon S)}[n^{+}S^{-} + n^{-}S^{+} - n_{tr}S] \qquad A.7$$

In case of a spin laser near threshold, one of the gain modes crosses threshold and starts lasing. In other words $S^{+} \sim 0$ and contribution is entirely due to S^{-}

$$g^{+}S^{-} + g^{-}S^{+} = g^{+}S^{-} = \frac{g_0 S^{-}(n^{-} - n_{tr})}{(1 + \epsilon S)} \qquad A.8$$

Representing the spin polarized carrier density in terms of total carrier density (n) and the spin polarization (Π_S) and spontaneous recombination in terms of the carrier density and recombination lifetime,

$$n^{+} = \frac{n}{2}(1 + \Pi_S);\; n^{-} = \frac{n}{2}(1 - \Pi_S);\; R_{sp}^{\pm} = \frac{n^{\pm}}{\tau_r} \qquad A.9$$

Substituting these in the carrier density and photon density equations we have,

$$\frac{dn}{dt} = \frac{J}{qd} - \frac{v_g g_0 S^{-}}{1 + \epsilon S^{-}}\left[\frac{n}{2}(1 + \Pi_S) - n_{tr}\right] - \frac{n}{\tau_r} \qquad A.10$$

$$\frac{dS^{-}}{dt} = \frac{\Gamma v_g g_0 S^{-}}{1 + \epsilon S^{-}}\left[\frac{n}{2}(1 + \Pi_S) - n_{tr}\right] - \frac{S^{-}}{\tau_{ph}} + \frac{\beta \Gamma n}{\tau_r} \qquad A.11$$

Under steady state conditions

$$\frac{dn}{dt} = 0; \quad \frac{J}{qd} = \frac{v_g g_0 S^{-}}{1 + \epsilon S^{-}}\left[\frac{n}{2}(1 + \Pi_S) - n_{tr}\right] + \frac{n}{\tau_r} \qquad A.12$$

$$\frac{dS^{-}}{dt} = 0; \quad \frac{\Gamma v_g g_0 S^{-}}{1 + \epsilon S^{-}}\left[\frac{n}{2}(1 + \Pi_S) - n_{tr}\right] - \frac{S^{-}}{\tau_{ph}} + \frac{\beta \Gamma n}{\tau_r} (= 0) \qquad A.13$$

$$S^{-} = \frac{1}{\epsilon}\left\{\Gamma v_g g_0 \tau_{ph}\left[\frac{n}{2}(1 + \Pi_S) - n_{tr}\right] - 1\right\} \qquad A.14$$

Substituting S in the equation for current density

$$\frac{J}{qd} = \frac{n}{\tau_r} + \frac{1}{\Gamma \tau_{ph} \epsilon}\left[\Gamma \mathrm{v_g} g_0 \tau_{ph}\left\{\frac{n}{2}(1+\Pi_S) - n_{tr}\right\} - 1\right] \qquad A.15$$

For small signal modulation of the spin laser

$$J = \bar{J} + \Delta J; n = \bar{n} + \Delta n; S^- = \bar{S}^- + \Delta S \qquad A.16$$

We assume

$$a = 1 + \Pi_\mathrm{S};\ \frac{1}{1+\epsilon \mathrm{S}^-} \backsimeq 1 - \epsilon \mathrm{S}^- \qquad A.17$$

Under steady state

$$\frac{d\Delta n}{dt} = \frac{\bar{J} + \Delta J}{qd} - \frac{g_0(\bar{S}^- + \Delta S)\left(a\left(\frac{\bar{n}+\Delta n}{2}\right) - n_{tr}\right)}{1 + \epsilon(\bar{S}^- + \Delta S)} - \frac{\bar{n} + \Delta n}{\tau_r} \qquad A.18$$

$$\frac{d\Delta n}{dt} = \frac{\bar{J} + \Delta J}{qd} - g_0(\bar{S}^- + \Delta S - \epsilon(\bar{S}^- + \Delta S)^2)\left(a\left(\frac{\bar{n}+\Delta n}{2}\right) - n_{tr}\right) - \frac{\bar{n} + \Delta n}{\tau_r} \qquad A.19$$

$$\frac{d\Delta n}{dt} = \frac{\bar{J} + \Delta J}{qd} - g_0\left(\bar{S}^- + \Delta S - \epsilon\left(\bar{S}^{-2} + 2\Delta S\bar{S}^-\right)\right)\left(a\left(\frac{\bar{n}+\Delta n}{2}\right) - n_{tr}\right) - \frac{\bar{n} + \Delta n}{\tau_r} \qquad A.20$$

Neglecting higher order terms of ΔS

$$\frac{d\Delta n}{dt} = \frac{\bar{J} + \Delta J}{qd} - g_0(\bar{S}^- + \Delta S - \epsilon(\bar{S}^2 + 2\Delta S\bar{S}^-))\left(a\left(\frac{\bar{n}+\Delta n}{2}\right) - n_{tr}\right) - \frac{\bar{n} + \Delta n}{\tau_r} \qquad A.21$$

$$\frac{d\Delta n}{dt} = \frac{\bar{J} + \Delta J}{qd} - g_0\left[\left(\frac{a\bar{n}}{2} - n_{tr}\right)\{\bar{S}^-(1 - \epsilon\bar{S}^-) + \Delta S(1 - 2\epsilon\Delta S)\}\right]$$

$$-\frac{g_0 a \Delta n \bar{S}^-}{2}(1 - \epsilon\bar{S}^-) - \frac{\bar{n} + \Delta n}{\tau_r} \qquad A.22$$

Simplifying and taking the steady state condition into account

$$\frac{d\Delta n}{dt} = \frac{\Delta J}{qd} - g_0\left[\left(\frac{a\bar{n}}{2} - n_{tr}\right)\Delta S(1 - 2\epsilon\Delta S)\right] - \Delta n\left[g_0\frac{a}{2}\bar{S}^-(1 - \epsilon\bar{S}) + \frac{1}{\tau_r}\right] \qquad A.23$$

$$\frac{d\Delta n}{dt} = \frac{\Delta J}{qd} - b\Delta S - \left(c + \frac{1}{\tau_r}\right)\Delta n \qquad A.24$$

Where,

$$b = v_g g_0 \left(\frac{a\bar{n}}{2} - n_{tr}\right)(1 - 2\epsilon\Delta S); c = v_g g_0 \frac{a}{2}\bar{S}^-(1 - \epsilon\bar{S}^-)$$

Upon simplification of the photon density equation we get

$$\frac{d(\bar{S}^- + \Delta S)}{dt} = \frac{\Gamma g_0(\bar{S}^- + \Delta S)\left(a\left(\frac{\bar{n} + \Delta n}{2}\right) - n_{tr}\right)}{1 + \epsilon(\bar{S}^- + \Delta S)} - \frac{\bar{S}^- + \Delta S}{\tau_{ph}} + \frac{\beta\Gamma(\bar{n} + \Delta n)}{\tau_r} \qquad A.25$$

$$\frac{d\Delta S}{dt} = \Gamma g_0 \left\{\bar{S}^- + \Delta S - \epsilon\left(\bar{S}^{-2} + 2\Delta S\bar{S}^-\right)\right\}\left(a\left(\frac{\bar{n} + \Delta n}{2}\right) - n_{tr}\right) - \frac{\bar{S}^- + \Delta S}{\tau_{ph}}$$

$$+ \frac{\beta\Gamma(\bar{n} + \Delta n)}{\tau_r} A.26$$

$$\frac{d\Delta S}{dt} = \Gamma g_0 \bar{S}^-(1 - \epsilon\bar{S}^-)\left(\frac{a\bar{n}}{2} - n_{tr}\right) - \frac{\bar{S}^-}{\tau_{ph}} + \frac{\beta\Gamma\bar{n}}{\tau_r} + \Gamma g_0 \bar{S}^-(1 - \epsilon\bar{S}^-)\frac{a\Delta n}{2}$$

$$+ \Gamma g_0 \bar{S}^-(1 - 2\epsilon\bar{S}^-)\left(\frac{a\bar{n}}{2} - n_{tr}\right) - \frac{\Delta S}{\tau_{ph}} + \frac{\beta\Gamma\Delta n}{\tau_r} \qquad A.27$$

Under steady state we have

$$\frac{d\Delta S}{dt} = \Gamma g_0 \bar{S}^-(1 - \epsilon\bar{S}^-)\frac{a\Delta n}{2} + \Gamma g_0 \Delta S(1 - 2\epsilon\bar{S}^-)\left(\frac{a\bar{n}}{2} - n_{tr}\right) - \frac{\Delta S}{\tau_{ph}} + \frac{\beta\Gamma\Delta n}{\tau_r} \quad A.28$$

Substituting for constants b and c we obtain

$$\frac{d\Delta S}{dt} = \Gamma\Delta n\left(c + \frac{\beta}{\tau_r}\right) + \Delta S\left(\mathrm{b}\Gamma - \frac{1}{\tau_{ph}}\right) \qquad A.29$$

Taking the Laplace transform of the eqn.

$$\frac{d\Delta n}{dt} = \frac{\Delta J}{qd} - b\Delta S - \left(c + \frac{1}{\tau_r}\right)\Delta n \qquad A.30$$

$$\tilde{s}\Delta n = \frac{\Delta J}{qd} - b\Delta S - \left(c + \frac{1}{\tau_r}\right)\Delta n \qquad A.31$$

$$\Delta n = \frac{\left(\frac{\Delta J}{qd} - b\Delta S\right)}{\tilde{s} + \left(c + \frac{1}{\tau_r}\right)} \qquad A.32$$

Taking the Laplace transform of the eqn.

$$\frac{d\Delta S}{dt} = \Gamma\Delta n\left(c + \frac{\beta}{\tau_r}\right) + \Delta S\left(\mathrm{b}\Gamma - \frac{1}{\tau_{ph}}\right) \qquad A.33$$

$$\tilde{s}\Delta S = \Delta S\left(\mathrm{b}\Gamma - \frac{1}{\tau_{ph}}\right) + \Gamma\Delta n\left(c + \frac{\beta}{\tau_r}\right) \qquad A.34$$

Substituting for Δn

$$\Delta S\left[\tilde{s} + \left(\frac{1}{\tau_{ph}} - \mathrm{b}\Gamma\right)\right]\left[\tilde{s} + \left(c + \frac{1}{\tau_r}\right)\right] = \Gamma\left(c + \frac{\beta}{\tau_r}\right)\left(\frac{\Delta J}{qd} - b\Delta S\right) \qquad A.35$$

$$\frac{\Delta S}{\Delta J} = \frac{\Gamma\left(c + \frac{\beta}{\tau_r}\right)\frac{1}{qd}}{\left[\tilde{s} + \left(\frac{1}{\tau_{ph}} - \mathrm{b}\Gamma\right)\right]\left[\tilde{s} + \left(c + \frac{1}{\tau_r}\right)\right] + \Gamma\mathrm{b}\left(c + \frac{\beta}{\tau_r}\right)} \qquad A.36$$

For small signal

$$\frac{\Delta S}{\Delta J} = \frac{\Gamma\left(c + \frac{\beta}{\tau_r}\right)\frac{1}{qd}}{\left[j\omega + \left(\frac{1}{\tau_{ph}} - \mathrm{b}\Gamma\right)\right]\left[j\omega + \left(c + \frac{1}{\tau_r}\right)\right] + \Gamma\mathrm{b}\left(c + \frac{\beta}{\tau_r}\right)} \qquad A.37$$

This equation is of the form

$$\frac{\Delta \mathrm{S}}{\Delta \mathrm{J}} = \frac{x}{-\omega^2 + jy\omega + \omega_r^2} \qquad A.38$$

Hence the resonance frequency is given by

$$\omega_r^2 = \frac{1}{\tau_{ph}}\left(c + \frac{1}{\tau_r}\right) - \frac{\Gamma b}{\tau_r}(1 - \beta) \qquad A.39$$

Substituting for c and b in the above equation we get

$$\omega_r^2 = \frac{v_g g_0 \bar{S}^-}{\tau_{ph}}\left[\left(\frac{1 + \Pi_\mathrm{S}}{2}\right)(1 - \epsilon\bar{S}^-)\right] + \frac{1}{\tau_r}\left[\frac{1}{\tau_{ph}} - \Gamma(1 - \beta)g_0(1 - 2\epsilon\bar{S}^-)(n - n_{tr})\right] A.40$$

The second term in this equation is much smaller and hence is neglected. The contribution due to gain compression factor for is also small for devices biased near threshold

$$\omega_r^2 = \frac{2v_g g_0 \bar{S}^-}{\tau_{ph}}\left[\left(\frac{1+\Pi_S}{2}\right)\right] \qquad A.41$$

Comparison of resonance frequency at a fixed light output

In case of a spin laser where $\Pi_S \neq 0$

$$\omega_{r,spin}^2 = \frac{2v_g g_0 \bar{S}^-}{\tau_{ph}}\left[\left(\frac{1+\Pi_S}{2}\right)\right] \qquad A.42$$

In case of a conventional laser where $\Pi_S = 0$. Here the contribution to the light output from each mode is half of the total light output obtained. Hence

$$\frac{\omega_{r,spin}}{\omega_r} = \sqrt{2(1+\Pi_S)} \qquad A.43$$

The frequency response can also be derived alternatively as follows :

To determine the small signal response, we assume $J = J_0 + \Delta J$,$n^\pm = n_0^\pm + \Delta n^\pm$, and $S^\pm = S_0^\pm + \Delta S^\pm$; where $J_0, n_0^\pm$, and $S_0^\pm$are their corresponding equilibrium values. Equations A.1 and A.2 are modified for small signals as,

$$\frac{d}{dt}\begin{bmatrix}\Delta n^+\\ \Delta n^-\\ \Delta S^+\\ \Delta S^-\end{bmatrix} = \begin{bmatrix}-a_1 & a_2 & 0 & -K_1\\ b_2 & -b_1 & -M_1 & 0\\ 0 & c_2 & c_1 & 0\\ d_2 & 0 & 0 & d_1\end{bmatrix}\begin{bmatrix}\Delta n^+\\ \Delta n^-\\ \Delta S^+\\ \Delta S^-\end{bmatrix} + \frac{\Delta J}{2}\begin{bmatrix}1-\Pi_J\\ 1+\Pi_J\\ 0\\ 0\end{bmatrix} \qquad A.44$$

Where $\begin{bmatrix}K_1 & K_2\\ M_2 & M_2\end{bmatrix} = \frac{2g_0}{1+\epsilon S_0}\begin{bmatrix}(n_0^+ - n_{tr}) & S_0^-\\ (n_0^- - n_{tr}) & S_0^+\end{bmatrix}$, and

$$\begin{bmatrix}a_1 & b_1 & c_1 & d_1\\ a_2 & b_2 & c_2 & d_2\end{bmatrix} = \begin{bmatrix}K_2 + 1/\tau_s + 1/\tau_s & M_2 + 1/\tau_s + 1/\tau_s & \Gamma M_1 - 1/\tau_{ph} & \Gamma M_1 - 1/\tau_{ph}\\ 1/\tau_s & 1/\tau_s & \Gamma(M_2 + \beta/\tau_r) & \Gamma(K_2 + \beta/\tau_r)\end{bmatrix}$$

The above equation is solved to obtain the transfer function (in Laplace domain), $\partial S^\pm/\partial J$ and $\partial S\ /\partial J$. The analytical form for $\partial S^\pm/\partial J$ is given by

$$\frac{\partial S^+}{\partial J} = \frac{v_2 s^2 + v_1 s + v_0}{s^4 + \delta_3 s^3 + \delta_2 s^2 + \delta_1 s + \delta_0} \tag{A.45}$$

Where

$$\delta_3 = (b_1 - c_1) + (a_1 - d_1)$$
$$\delta_2 = (M_1 c_2 - b_1 c_1) + (K_1 d_2 - a_1 d_1) + (b_1 - c_1)(a_1 - d_1) - d_2 a_2$$
$$\delta_1 = (a_1 - d_1)(M_1 c_2 - b_1 c_1) + (b_1 - c_1)(K_1 d_2 - a_1 d_1) + a_2 b_2 (c_1 + d_1)$$
$$\delta_0 = (M_1 c_2 - b_1 c_1)(K_1 d_2 - a_1 d_1) + a_2 b_2 c_1 d_1$$
$$v_2 = (1/2)\left(1 + \Pi_J\right) c_2$$
$$v_1 = (1/2)\left[\left(1 + \Pi_J\right)(a_1 - d_1) + \left(1 - \Pi_J\right) b_2\right] c_2$$
$$v_0 = (1/2)\left[\left(1 + \Pi_J\right)\right](K_1 d_2 - a_1 d_1) - \left(1 - \Pi_J\right) b_2 d_1$$

Similar transfer functions are derived for other cases. Equation 1.4 can be further simplified for case when only one mode is lasing using simplifying assumptions $1/(1+\epsilon S) \sim (1-\epsilon S)$, $\Delta n \Delta S \ll min\{n\Delta S, \Delta n S, nS\}, \Delta n^{\pm} \ll n^{\pm}$, and $\Delta S^{\pm} \ll S^{\pm}$ as,

$$f_R^+ = \frac{1}{2\pi}\left\{\frac{v_g g_0 S^+}{\tau_{ph}}\left[(1+\Pi_S)(1-\epsilon S^+)\right] + \frac{1}{\tau_r}\left[\frac{1}{\tau_{ph}} - 2\Gamma(1-\beta) g_0 (1 - 2\epsilon S^+)(n - n_{tr})\right]\right\}^{1/2} \tag{A.46}$$

APPENDIX B

Solution of Drift-Diffusion Equation and Laser Rate Equations at Steady State

Spin diffusion [drift is negligible due to relatively high doping concentration ($N_D \sim 5 \times 10^{17}\ cm^{-3}$) present in the GaAs layer carrying the carriers and therefore neglected] from the ferromagnetic contact to the edge of the barrier region of the laser together with the spin dependent laser carrier-photon rate equations, completely describe the operation of the electrically injected spin laser.

We define the following parameters:

1) Quantum-dot spin polarization, $\Pi_s = (n^+ - n^-)/(n^+ + n^-)$; 2) carrier polarization at any point $x(0 < x < x_1)$, $\Pi(x) = (N^+ - N^-)/(N^+ + N^-)$; and 3) polarization at the barrier, $\Pi_{s,b} = (n_b^+ - n_b^-)/(n_b^+ + n_b^-)$. We also note that the photon density at threshold, $S = S_{th}$.

B.1. Derivation of relation between P_{spin} and $\Pi_{s,b}$

Adding and subtracting Eqn. (1) for spin-up and spin-down electrons we get, $n_b^+ + n_b^- = I_{pump}\tau_{cap}/qV_b$ and $n_b^+ - n_b^- = I_{pump}P_{spin}\tau/qV_b$, respectively. Hence we get,

$$P_{spin} = \Pi_{s,b}\frac{\tau_{cap}}{\tau}. \qquad (B.1)$$

B.2. Field-dependent threshold current

Adding and subtracting Eqn. (2) for spin-up and spin-down electrons we get,

$$\frac{V_b}{V_{QD}}\frac{n_b}{\tau_{cap}} = v_g[g(n^+,S^-)S^- + g(n^-,S^+)S^+] + B_{sp}n^2 + Cn^3\,, \qquad (B.2)$$

$$\frac{V_b}{V_{QD}}\frac{n_b^+ - n_b^-}{\tau_{cap}} = v_g[g(n^+,S^-)S^- - g(n^-,S^+)S^+] + (n^+ - n^-)\left(B_{sp}n^2 + Cn^3 + \frac{2}{\tau_s}\right). \qquad (B.3)$$

Similar operations on Eqn. (B.3) yield,

$$v_g[g(n^+,S^-)S^- + g(n^-,S^+)S^+] = \frac{S}{\Gamma\tau_{ph}} - \beta B_{sp}n^2, \qquad (B.4)$$

$$v_g[g(n^+,S^-)S^- - g(n^-,S^+)S^+] = -\frac{S^+ - S^-}{\Gamma\tau_{ph}} - \beta B_{sp}n(n^+ - n^-) \qquad (B.5)$$

Combining Eqns. (B.1) and (B.3), and using $n_b^+ + n_b^- = I_{pump}\tau_{cap}/qV_b$ we get Eqn. (6.6).

Equation (6.7) is obtained from Eqn. (6.6) by using the fact that $\Pi_S = 0$ when $H = 0$.

B.3. Output polarization

From Eqn. (6.5) we get,

$$S^{\pm} = \frac{\Gamma\beta B_{\mathrm{sp}}n^{\mp}n}{\frac{1}{\tau_{ph}} - \Gamma v_g g(n^{\mp})}\,. \qquad (B.6)$$

Taking the ratio of $(S^+ - S^-)$ to $(S^+ + S^-)$ we get Eqn. (6.8).

B.4. Gain Anisotropy Parameter

Equation (6.9) is derived from the definition of modal gain along with the fact that n_{tr} is much less than n_{th}.

B.5. Determination of quantum dot spin polarization Π_S in terms of laser parameters

Since all the expressions are derived in terms of Π_S, we finally need to express this parameter in terms of more fundamental laser parameters. Solving Eqn. (6.1) and using Eqn. (6.2) and the boundary conditions that the spin carrier densities and the spin-currents are continuous at barrier, we get

$$P_{contact} = P_{spin}\cosh(x_1/\lambda_{sf}) - \lambda_{sf}\left(\frac{\Pi_S - P_{spin}}{x_2 - x_1}\right)\sinh(x_1/\lambda_{sf}). \qquad (B.7)$$

We also have from Eqns. (B.2)-(B.4) and Eqn. (6.8),

$$\frac{\Pi_{s,b}}{\Pi_S} = K_1 + \frac{1}{K_0}(K_2 - \Pi_S K_3). \qquad (B.8)$$

where $K_0 = I_{pump}/qV_{QD}$, $K_1 \approx \left(1 + \Gamma v_g \tau_{ph}\frac{dg}{dn}n_{tr}\right)/\left(1 - \Gamma v_g \tau_{ph}\frac{dg}{dn}n_{th}\right)$, $K_2 = (1-K_1)\left[(1-\beta)B_{sp}n_{th}^2 + Cn_{th}^3\right] + 2n_{th}/\tau_s$, and $K_3 = 2(1-K_1)(1-\beta)B_{sp}n_{th}^2 + 3(1-K_1)Cn_{th}^3 + 2n_{th}/\tau_s$ are constants for a given pump current and applied magnetic field. Combining equations (B.7) and (B.8) we get,

$$\Pi_S^2\left(\frac{b_2K_3}{K_0}\right) + \Pi_S\left(b_3 - b_2K_1 - \frac{b_2K_2}{K_0}\right) - P_{contact} = 0. \qquad (B.9)$$

Where $b_1 = \lambda_{sf}/(x_2 - x_1)$, $b_2 = \left[\cosh(x_1/\lambda_{sf}) + b_1\sinh(x_1/\lambda_{sf})\right]\tau_{cap}/\tau$,

$b_3 = b_1 \sinh(x_1/\lambda_{sf})$. It is assumed that Π_S is small compared to unity as in a spin laser. Solving Eqn. (B.9) we get Π_S, and hence $I_{th}(H)$ and $\Pi_C(H, I_{pump})$.

APPENDIX C

Solution of Drift-Diffusion Equation for a Spin Modulator

C.1 Infinite channel approximation

Drift diffusion equation for spin dynamics.

$$\frac{\partial \vec{s}}{\partial t} = \vec{s} \times \overrightarrow{\omega_0} + \mathrm{D}\nabla^2 \vec{s} + \mu E \nabla \vec{s} - \frac{\vec{s}}{\tau_s} \qquad C.1$$

The first term on the right describes the contribution due to spin precession.

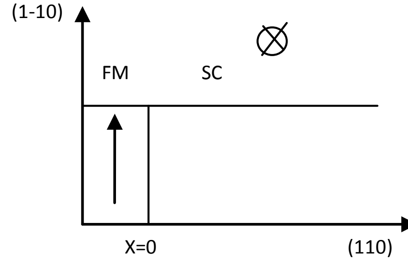

The electric field applied on the gate terminal generates an effective magnetic field in the (110) direction due to the Rashba effect. The type-B MnAs used as the ferromagnetic injector has its easy axis along the (1-10) direction and hence injects spin in the same direction when magnetized. Hence the precession of the injected spin polarized charge carriers is possible in the device. Here we derive the steady state effects observed in the device by equating the time derivate to zero.

$$\dot{s_x} = D s_x^{//} - \dot{v_d} s_x^{/} - {}^{s_x}/_{\tau_s} = 0 \qquad C.2$$

$$\dot{s_y} = s_z\omega_0 + Ds_y^{//} - v_d s_y^{/} - {}^{s_y}/_{\tau_s} = 0 \qquad C.3$$

$$\dot{s_z} = -s_y\omega_0 + Ds_z^{//} - v_d s_z^{/} - {}^{s_z}/_{\tau_s} = 0 \qquad C.4$$

Here we see that the contribution due to the effective magnetic field in the (110) direction does not affect the x-component of the spin vector **s**. The solutions for these equations are of the form

$$s_y = A_y e^{-\alpha x/L_s}, s_z = A_z e^{-\alpha x/L_s}$$

The solution set for α is of the form

$$\alpha = \begin{Bmatrix} 1 - i\omega_0\tau_s \\ 1 + i\omega_0\tau_s \end{Bmatrix}$$

The solution of the differential equation in terms of the carrier density can be expressed as

$$n_{y\uparrow(\downarrow)} = +(-)A_y e^{-x/L_s}\left(cos\frac{\omega_0\tau_s x}{L_s} - isin\frac{\omega_0\tau_s x}{L_s}\right) \qquad C.5$$

$$n_{z\uparrow(\downarrow)} = +(-)A_z e^{-x/L_s}\left(cos\frac{\omega_0\tau_s x}{L_s} + isin\frac{\omega_0\tau_s x}{L_s}\right) \qquad C.6$$

The carrier densities can be expressed in terms of the chemical potential which are written as follows

$$\mu_{y\uparrow(\downarrow)} = +(-)k_B T\frac{2A_y}{n_0}e^{-x/L_s}\left(cos\frac{\omega_0\tau_s x}{L_s} - isin\frac{\omega_0\tau_s x}{L_s}\right) + \frac{ejx}{\sigma_n} + B \qquad C.7$$

$$\mu_{z\uparrow(\downarrow)} = +(-)k_B T\frac{2A_z}{n_0}e^{-x/L_s}\left(cos\frac{\omega_0\tau_s x}{L_s} + isin\frac{\omega_0\tau_s x}{L_s}\right) + \frac{ejx}{\sigma_n} + B \qquad C.8$$

Here the flow of current is in along the (110) and the only the component of the spin polarization in the direction of magnetization of the source pad is considered. The constants are determined by solving the boundary conditions that the spin currents are continuous at x = 0 (assuming there is no spin flip scattering at the interface) as given by

$$j_{\uparrow}(0^-) = G_{\uparrow}\big(\mu_{\uparrow}(0^+) - \mu_{\uparrow}(0^-)\big) \qquad C.9$$

$$j_{\downarrow}(0^-) = G_{\downarrow}\big(\mu_{\downarrow}(0^+) - \mu_{\downarrow}(0^-)\big) \qquad C.10$$

In the ferromagnetic contact

$$\frac{1}{ej}\mu_{\uparrow}^{f} = \frac{x}{\sigma_{\uparrow}^{f} + \sigma_{\downarrow}^{f}} + C\frac{1}{\sigma_{\uparrow}^{f}}e^{x/L_f} \qquad C.11$$

The spin transport length in ferromagnet $L_f << L_s$ hence we ignore the contribution from the second term. The spin dependent current expressed in terms of electrochemical potential is written as

$$j_{\uparrow(\downarrow)} = \frac{\sigma_{\uparrow(\downarrow)}}{e}\frac{\partial\mu_{\uparrow(\downarrow)}}{\partial x} \qquad C.12$$

At the interface of the ferromagnet with the semiconductor the current densities can be expressed as

$$j_{\uparrow}(0^-) = \frac{j}{2}\left(1 + \alpha_f\right); j_{\downarrow}(0^-) = \frac{j}{2}\left(1 - \alpha_f\right);$$

Here $\alpha_f = \frac{\sigma_{\uparrow}^{f} - \sigma_{\downarrow}^{f}}{\sigma_{\uparrow}^{f} + \sigma_{\downarrow}^{f}}$ is the spin polarization of type B MnAs used as the spin injector in our device.

Solving the boundary conditions at the FM/NS interface we get

$$\Delta\mu_y = j\left(\frac{1+\alpha_f}{G_\uparrow} - \frac{1-\alpha_f}{G_\downarrow}\right)e^{-x/L_s}\left(cos\frac{\omega_0\tau_s x}{L_s} - isin\frac{\omega_0\tau_s x}{L_s}\right) \qquad C.13$$

The current spin polarization is given by

$$\frac{\Delta j}{j} = \frac{\sigma_n}{eL_s}\left(\frac{1+\alpha_f}{G_\uparrow} - \frac{1-\alpha_f}{G_\downarrow}\right)e^{-x/L_s}\left(cos\frac{\omega_0\tau_s x}{L_s} + \omega_0\tau_s sin\frac{\omega_0\tau_s x}{L_s}\right) \qquad C.14$$

C.2 Finite channel length

The contribution due to the effective magnetic field in the (110) direction does not affect the x-component of the spin vector **s**. The solutions to these equations C.2-C.4 for a device with finite channel length (L_{chan}) are of the form

$$s_v = A_{y1}e^{-\alpha u/L_s} + A_{y2}e^{-\alpha(L_{chan}-u)/L_s} \qquad C.15$$

$$s_z = A_{z1}e^{-\alpha u/L_s} + A_{z2}e^{-\alpha(L_{chan}-u)/L_s} \qquad C.16$$

The solution set for α is of the form

$$\alpha = \begin{Bmatrix} 1 - i\omega_0\tau_s \\ 1 + i\omega_0\tau_s \end{Bmatrix}$$

Substituting the value of α and expressing the solution in terms of carrier concentration we get

$$n_{y\uparrow(\downarrow)} = +(-)A_{y1}e^{-x/L_s}\left(cos\frac{\omega_0\tau_s x}{L_s} - isin\frac{\omega_0\tau_s x}{L_s}\right) + (-)A_{y1}e^{-(L_{chan}-x)/L_s}\left(cos\frac{\omega_0\tau_s x}{L_s} - isin\frac{\omega_0\tau_s x}{L_s}\right) \quad C.17$$

$$n_{z\uparrow(\downarrow)} = +(-)A_{z1}e^{-x/L_s}\left(cos\frac{\omega_0\tau_s x}{L_s} + isin\frac{\omega_0\tau_s x}{L_s}\right) + (-)A_{z1}e^{-(L_{chan}-x)/L_s}\left(cos\frac{\omega_0\tau_s x}{L_s} + isin\frac{\omega_0\tau_s x}{L_s}\right) \quad C.18$$

The carrier densities can be expressed in terms of the chemical potential which are written as follows

$$\mu_{y\uparrow(\downarrow)} = +(-)k_BT\frac{2A_{y1}}{n_0}e^{-x/L_s}\left(cos\frac{\omega_0\tau_s x}{L_s} - isin\frac{\omega_0\tau_s x}{L_s}\right) + (-)k_BT\frac{2A_{y2}}{n_0}e^{-(L_{chan}-x)/L_s}\left(cos\frac{\omega_0\tau_s x}{L_s} - isin\frac{\omega_0\tau_s x}{L_s}\right) + \frac{ejx}{\sigma_n} + B \qquad C.19$$

$$\mu_{z\uparrow(\downarrow)} = +(-)k_B T \frac{2A_{z1}}{n_0} e^{-x/L_s} \left(cos \frac{\omega_0 \tau_s x}{L_s} + isin \frac{\omega_0 \tau_s x}{L_s} \right) + (-)k_B T \frac{2A_{z2}}{n_0} e^{-(L_{chan}-x)/L_s} \left(cos \frac{\omega_0 \tau_s x}{L_s} + isin \frac{\omega_0 \tau_s x}{L_s} \right) + \frac{ejx}{\sigma_n} + B \qquad C.20$$

Here the flow of current is in along the (110) and the only the component of the spin polarization in the direction of magnetization of the source pad is considered. The constants are determined by solving the boundary conditions that the spin currents are continuous at x = 0 and x=L_{chan} (assuming there is no spin flip scattering at the interface) as given by

$$j_\uparrow(0^-) = G_\uparrow\left(\mu_\uparrow(0^+) - \mu_\uparrow(0^-)\right) \qquad C.21$$

$$j_\downarrow(0^-) = G_\downarrow\left(\mu_\downarrow(0^+) - \mu_\downarrow(0^-)\right) \qquad C.22$$

$$j_\uparrow(0^-) - j_\downarrow(0^-) = j_\uparrow(0^+) - j_\downarrow(0^+) \qquad C.23$$

$$j_\uparrow(L_{chan}^+) = G_\uparrow\left(\mu_\uparrow(L_{chan}^+) - \mu_\uparrow(L_{chan}^-)\right) \qquad C.24$$

$$j_\downarrow(L_{chan}^+) = G_\downarrow\left(\mu_\downarrow(L_{chan}^+) - \mu_\downarrow(L_{chan}^-)\right) \qquad C.25$$

$$j_\uparrow(L_{chan}^+) - j_\downarrow(L_{chan}^+) = j_\uparrow(L_{chan}^-) - j_\downarrow(L_{chan}^-) \qquad C.26$$

The spin current densities can be expressed in terms of electrochemical potential as

$$j_{\uparrow(\downarrow)} = \frac{\sigma_{\uparrow(\downarrow)}}{e} \frac{\partial \mu_{\uparrow(\downarrow)}}{\partial x} \qquad C.27$$

In the ferromagnetic contact

$$\frac{1}{ej}\mu_{\uparrow}^{f} = \frac{x}{\sigma_{\uparrow}^{f} + \sigma_{\downarrow}^{f}} + C\frac{1}{\sigma_{\uparrow}^{f}}e^{x/L_f} \qquad C.28$$

The spin transport length in ferromagnet $L_f << L_s$ hence we ignore the contribution from the second term. At the interface of the ferromagnet with the semiconductor the current densities can be expressed as

$$j_{\uparrow}(0^-) = \frac{j}{2}(1 + \alpha_{fs}); j_{\downarrow}(0^-) = \frac{j}{2}(1 - \alpha_{fs});$$

$$j_{\uparrow}(L_{chan}^{+}) = \frac{j}{2}(1 + \alpha_{fD}); j_{\downarrow}(L_{chan}^{+}) = \frac{j}{2}(1 - \alpha_{fD})$$

Here $\alpha_{fs} = \frac{\sigma_{\uparrow}^{fs} - \sigma_{\downarrow}^{fs}}{\sigma_{\uparrow}^{fs} + \sigma_{\downarrow}^{fs}}$ and $\alpha_{fD} = \frac{\sigma_{\uparrow}^{fD} - \sigma_{\downarrow}^{fD}}{\sigma_{\uparrow}^{fD} + \sigma_{\downarrow}^{fD}}$ are the the spin polarization of type B MnAs at the source and the detector end in our device.

When the source and the drain contacts are magnetized in the same direction (parallel configuration) $\alpha_{fS} = \alpha_{fD}$ we get

$$A_{y1} = A_{y2} = \frac{j}{4}\frac{n_0}{k_B T}\left(\frac{1 + \alpha_{fs}}{G_{\uparrow}} - \frac{1 - \alpha_{fs}}{G_{\downarrow}}\right)\frac{1 - e^{-L_{chan}/L_S}}{1 - e^{-2L_{chan}/L_S}}$$

Substituting these values we get

$$\Delta\mu_y = j\left(\frac{1 + \alpha_f}{G_{\uparrow}} - \frac{1 - \alpha_f}{G_{\downarrow}}\right)\frac{1 - e^{-L_{chan}/L_S}}{1 - e^{-2L_{chan}/L_S}}\left(e^{-x/L_s} + e^{-(L_{chan}-x)/L_s}\right)\left(cos\frac{\omega_0\tau_s x}{L_s} - isin\frac{\omega_0\tau_s x}{L_s}\right) \qquad C.29$$

The spin polarization of the current in the parallel configuration can be expressed as

$$\frac{\Delta j_{\uparrow\uparrow}}{j} = \frac{\sigma_n}{eL_S}\left(\frac{1+\alpha_f}{G_\uparrow} - \frac{1-\alpha_f}{G_\downarrow}\right)\frac{1-e^{-L_{chan}/L_S}}{1-e^{-2L_{chan}/L_S}}\left[\left(-e^{-x/L_s} + e^{-(L_{chan}-x)/L_s}\right)\left(cos\frac{\omega_0\tau_s x}{L_s} - isin\frac{\omega_0\tau_s x}{L_s}\right) - \left(e^{-x/L_s} + e^{-(L_{chan}-x)/L_s}\right)\left(\omega_0\tau_s sin\frac{\omega_0\tau_s x}{L_s} + i\omega_0\tau_s cos\frac{\omega_0\tau_s x}{L_s}\right)\right] \quad C.30$$

Similarly spin polarized current for the drain and the source contact polarized in the anti-parallel configuration the spin polarization of the current is given by

$$\frac{\Delta j_{\uparrow\downarrow}}{j} = -\frac{\sigma_n}{eL_S}\left[\left(\frac{1}{G_\uparrow} - \frac{1}{G_\downarrow}\right)\left(\frac{1-e^{-L_{chan}/L_S}}{1-e^{-2L_{chan}/L_S}}\right) - \left(\frac{\alpha_{fs}}{G_\uparrow} + \frac{\alpha_{fs}}{G_\downarrow}\right)\left(\frac{1+e^{-L_{chan}/L_S}}{1-e^{-2L_{chan}/L_S}}\right)\right]\left[\left(e^{-x/L_s} + e^{-(L_{chan}-x)/L_s}\right)\left(cos\frac{\omega_0\tau_s x}{L_s} - isin\frac{\omega_0\tau_s x}{L_s}\right) + \left(e^{-x/L_s} - e^{-(L_{chan}-x)/L_s}\right)\left(\omega_0\tau_s sin\frac{\omega_0\tau_s x}{L_s} + i\omega_0\tau_s cos\frac{\omega_0\tau_s x}{L_s}\right)\right] \quad C.31$$

The difference in the spin polarization of the current is proportional to the change in the resistance observed from the MR measurement i.e.

$$\frac{\Delta j_{\uparrow\uparrow}}{j} - \frac{\Delta j_{\uparrow\downarrow}}{j} = \frac{R_P - R_{AP}}{R_P + R_{AP}} \quad C.32$$

APPENDIX D

Molecular Beam Epitaxy

Molecular beam epitaxy (MBE) is a technique for epitaxial growth via interaction of one or more molecular or atomic beams that occurs on a surface of a heated crystalline substrate. The solid sources materials are placed in evaporation cells to provide an angular distribution of atoms or molecules in a beam. The substrate is heated to the necessary temperature and, when needed, continuously rotated to improve the growth homogeneity. Fig. D.1 shows a schematic of a typical MBE system.

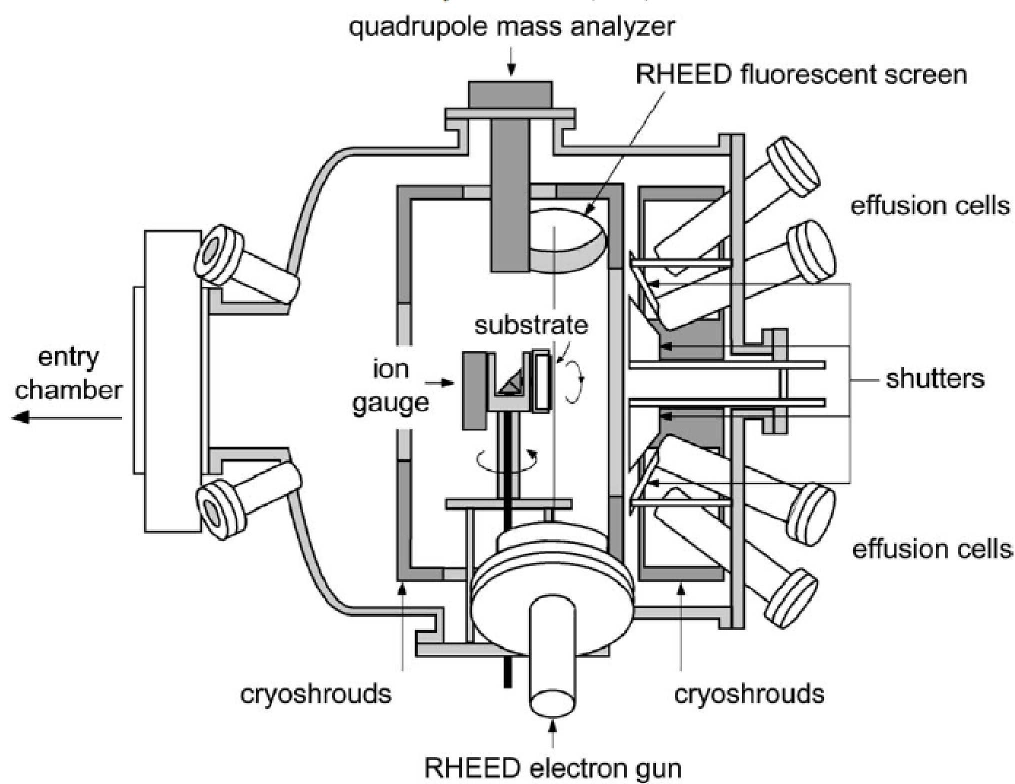

(a)

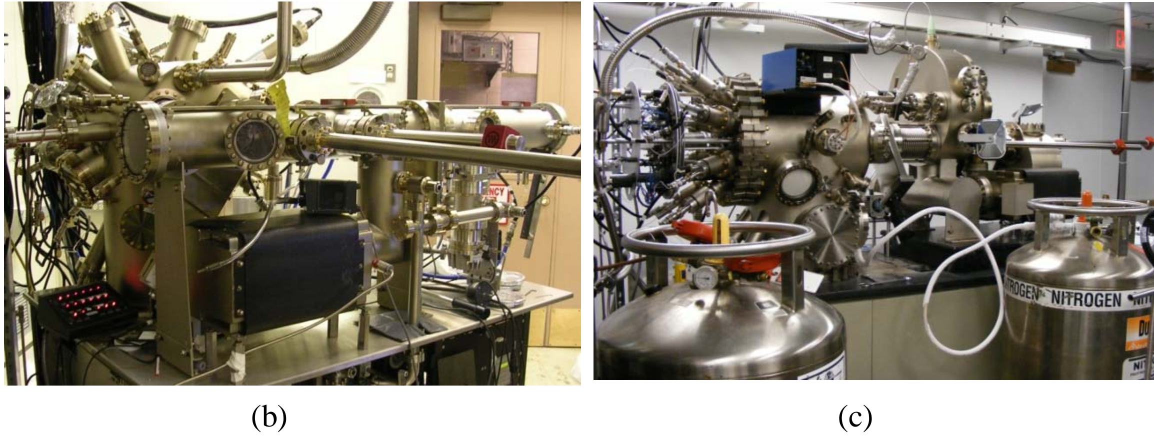

(b) (c)

Fig. D.1: (a) Schematic diagram of MBE growth reactor for growth of doped III-V compounds; (b) Veeco Mod Gen –II molecular beam epitaxy tool for growth of conventional III-V heterostuctures (c) Veeco Gen-II molecular beam epitaxy tool dedicated for heteroepitaxial growths and patterned growth of spin injector contacts.

The growth materials are contained separately in effusion cells as an elemental form. Each cell contains a crucible with an electrical heater which melts the charge of materials (Al, Ga, As, In *etc*). Each material is heated to a unique temperature which is dictated by the vapor pressure characteristics shown in fig. D.2. Molecules evaporate from the crucibles under the ultra high vacuum conditions maintained within the reactor. The flux of molecules is controlled by varying the cell temperatures and operating the cell shutters, which determine the species allowed to pass to the substrate. The growth chamber is kept at very high vacuum, typically 10^{-10} torr. At this pressure the mean free path of a free molecule in the chamber is very long; thus molecules emitted from the effusion cells typically travel directly towards the substrate as a molecular beam without being scattered. The possibility of contaminant species from the chamber being adsorbed onto the surface is also kept very low. Group III and group V molecules arriving on the heated substrate are adsorbed onto the crystal lattice resulting in epitaxial growth. Al, Ga, In, and As_2 or As_4 cells are used for the growth of AlGaAs and InGaAs compounds. Be and Si cells provide p- (accepter) and n- (donor) type dopants. The substrate is

rotated during the growth to reduce the effect of beam non-uniformity. In Fig. D.3 we show the exponential dependence of base equivalent pressure (BEP) of both aluminum and gallium with cell temperature. The BEP characterization of the material sources are done every time before epitaxial growth to ensure growth rate uniformity between samples grown at different times. It is important to realize that, due to material effusion the BEP may change even for successive growth runs. This is very critical for InP based lattice matched growth as a slight change of parameters can lead to large strain appearing in the heterostructure hence resulting in degradation of device performance. Hence BEP characterization was performed every time before any heterostructure was grown.

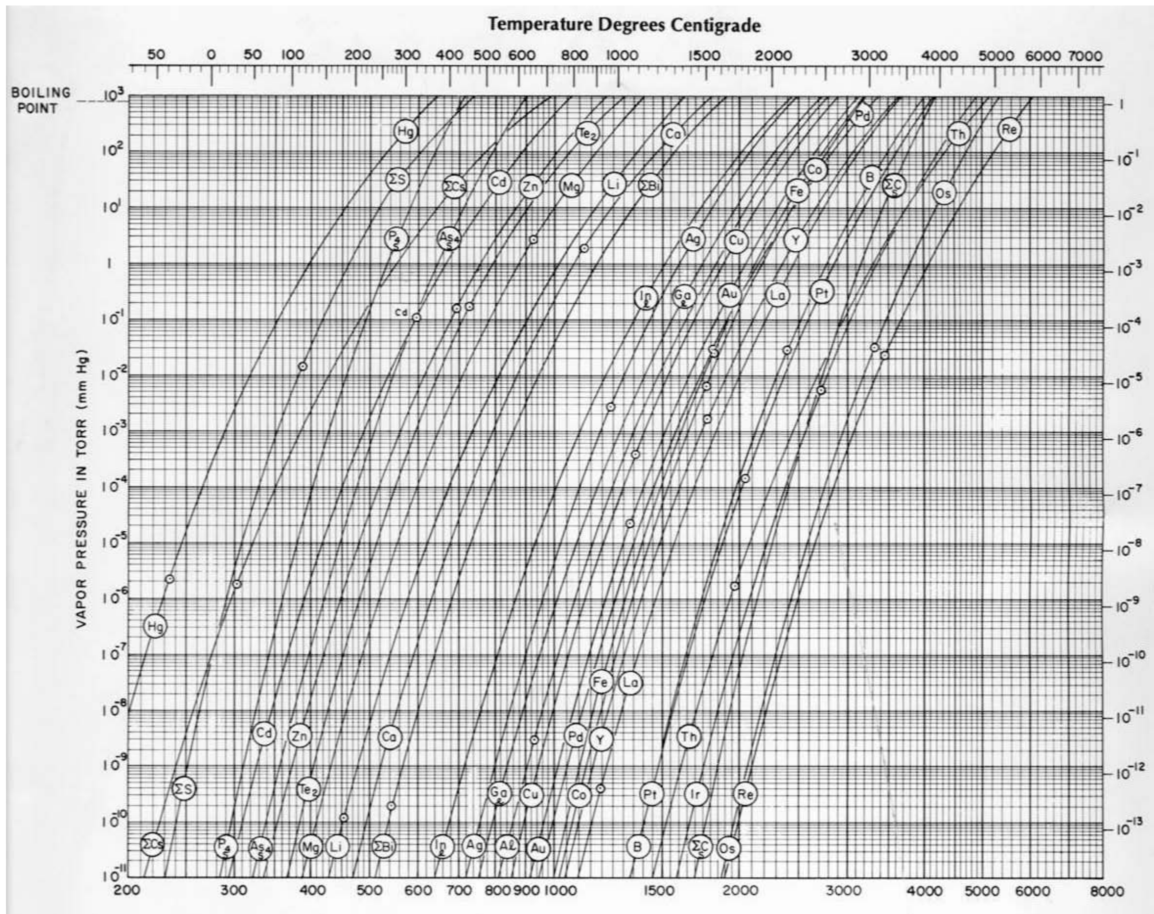

Fig. D.2: Vapor pressure vs temperature characteristics for different elements. This chart is very important in determining the type of effusion cell to be used as well as the temperature at which the material has to be heated in order to achieve an optimum growth rate and quality.

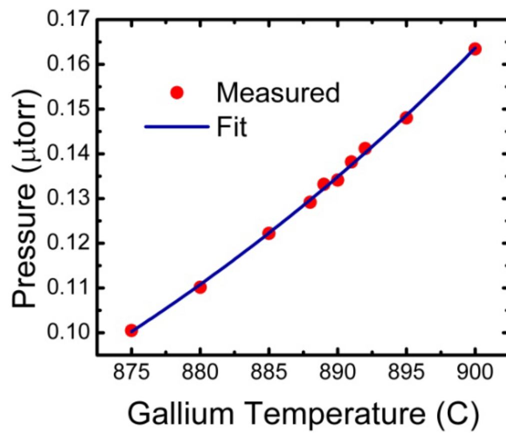

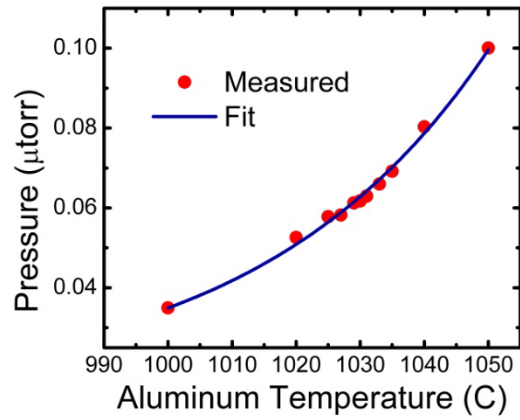

Fig. D.3: Base equivalent pressure vs cell temperature of (a) gallium effusion cell and; (b) aluminum effusion cell respectively in Veeco MOD GEN II used for growth callibration of the GaAs as well as InP based lattice matched compound semiconductors.

APPENDIX E

Fabrication of a Spin Vertical Cavity Surface Emitting Laser

Molecular beam epitaxy is used to grow the device heterostructure on a semi-insulating GaAs(001) substrates. The VCSEL consists of a 29.5-pair bottom $GaAs/Al_{0.8}Ga_{0.2}As$ mirrors including a n-type ($N_D = 5\times10^{18}$ cm^{-3}) 3-pairs of $GaAs/Al_{0.8}Ga_{0.2}As$ for n-contact layers, an undoped λ cavity with 8 to 10 layers of InAs quantum dots embedded in between 35 nm GaAs barriers and a p-type ($N_A = 5\times10^{18}$ m^{-3}) top AlGaAs/GaAs mirror (also working p-contact layers). The doped-AlGaAs layers were grown at 600 ^{o}C. The doped as well as the undoped GaAs layers were all grown at a 585°C. Both the layers were realized under a arsenic BEP of 5 x 10^{-6} torr . The InAs quantum dot layers were grown at 530°C under arsenic BEP of 2.5 x 10^{-6} torr.

The VCSEL process was initiated by wet etching the mesa in H_3PO_4:H_2O_2:H_2O (1:1:20) solution (Fig. D.1). The etch rate for this mixture is ~4.5 nm/sec although they are slightly different for AlGaAs, GaAs and the InAs quantum dots. The mesa definition is done in a GCA auto stepper photolithography tool. This is a I-line photolithography tool which uses a mercury arc lamp for exposure having a wavelength of 385 nm. This limits the minimum feature size realizable.

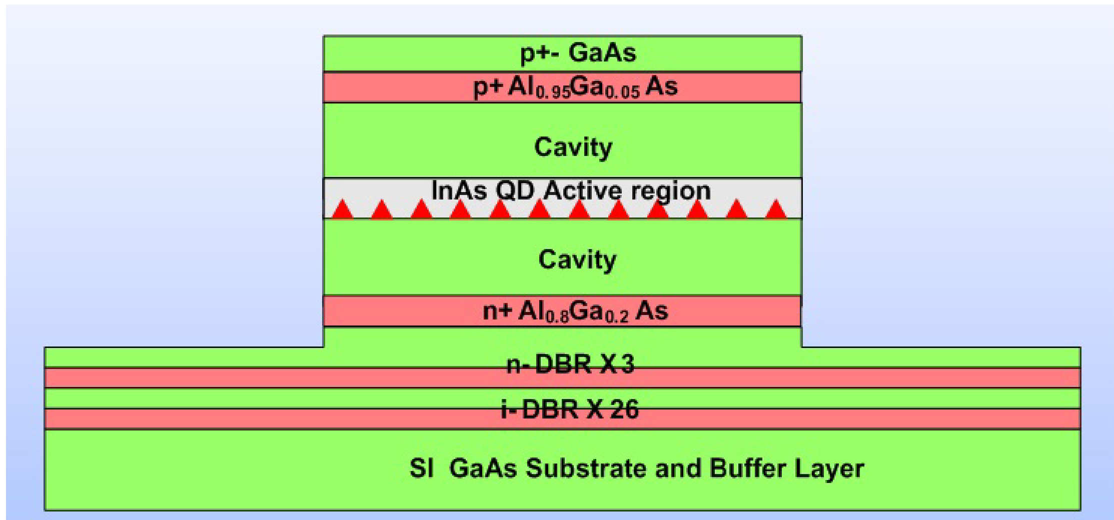

Fig. E.1: Mesa definition done by wet etching the MBE grown heterostructure.

The mesa is then conformally coated with 3000 Å, SiO_2 in a plasma enhanced chemical vapor deposition (PECVD) tool. Deposition proceeds at 200°C in the presence of silane and nitrous oxide. This deposition is carried out in order to protect the mesa sidewalls from damage during the regrowth of MnAs. The SiO_2 is removed from the rest of the sample by dryetching.

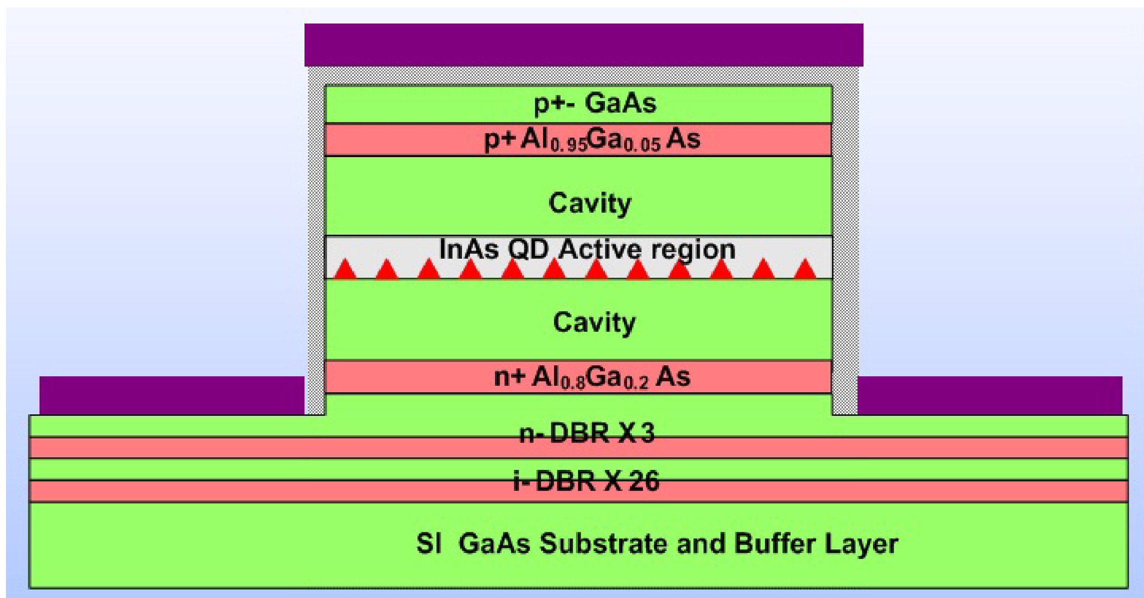

Fig. E.2: Patterned re-growth of spin injector contacts. The sidewalls of the mesa are protected by a conformal coating of SiO_2 during the regrowth step.

After the regrowth step the MnAs (Fig. E.2) a thin layer of Ti/Au is deposited on top in order to protect it from coming in contact with the photoresist developer (MF-319 or AZ-3000). This is followed by removal of the layers on top of the mesa by liftoff process using buffered hydorflouric acid. Here it has to be noted that titanium is etched by BHF and hence gold has to be used together with Ti in order to protect the MnAs.

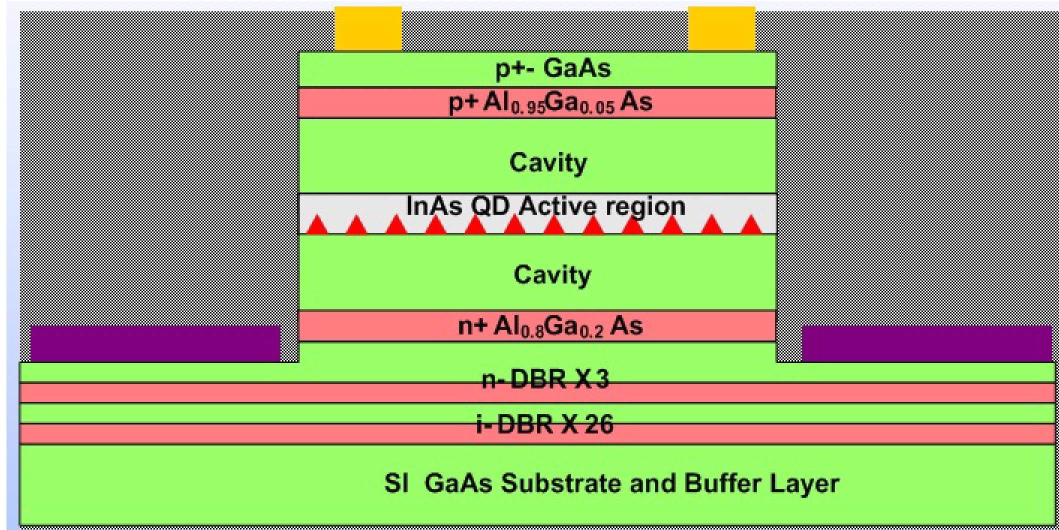

Fig. E.3: The p-ohmic contacts are deposited after conformally coating the device with Si_3N_4 passivating layer.

The structure is now passivated by conformally coating it with 3000 A of SiN. The deposition proceeds at 200 ^{o}C in the presence of silane and ammonia by the plasma enhanced chemical vapor deposition technique. The top p-ohmic contact was then realized by e-beam evaporation (Pd/Zn/Pd/Au = 100/200/200/2500 Å) (Fig. E.3).

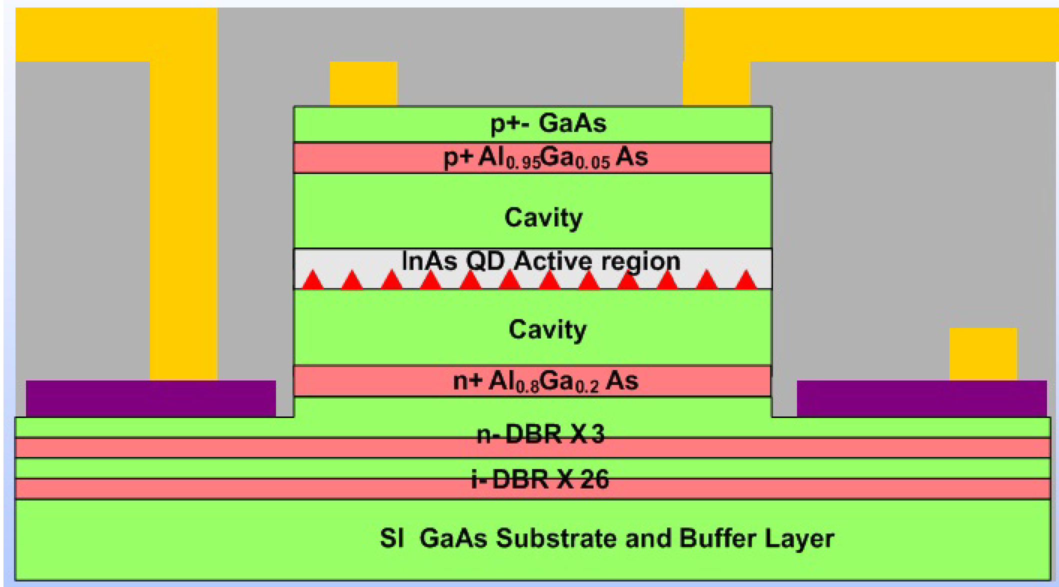

Fig. E.4: Interconnect metal deposition step.

This is followed by interconnect metal (Ti/Al/Ti/Au) metal deposition (Fig. E.4). The fabrication is complete with the selective deposition of 5 pairs of MgF_2/ZnSe top mirror in a SJ-26 e-beam evaporator (Fig. E.5).

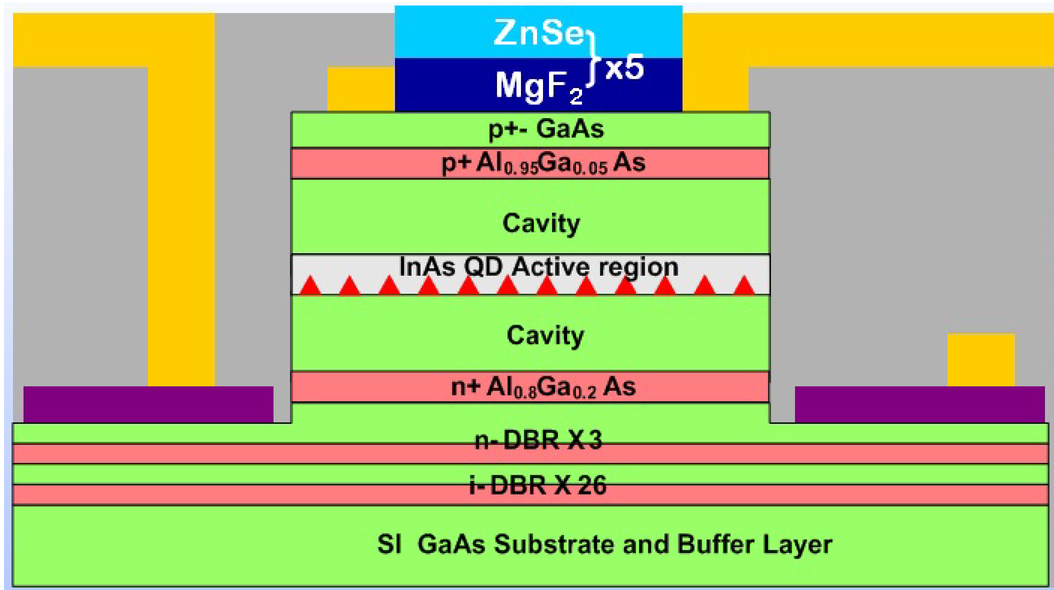

Fig. E.5: Dielectric mirror (ZnSe/MgF_2) deposition in an e-beam evaporator and finally lift off is the last step in the VCSEL fabrication.

BIBLIOGRAPHY

[1] G. E. Moore, *Electronics* **38**(8) (1965).

[2] http://www.itrs.net/links/2009ITRS/Home2009.htm

[3] S.D. Bader and S.S.P. Parkin, *Annu. Rev. Condens. Matter Phys.* (2010).

[4] M. N. Baibich, J. M. Broto, A. Fert, F. N. Van Dau, F. Petroff, P. Etienne, G. Creuzet, A. Friederich, and J. Chazelas, *Phys. Rev. Lett.* **61**, 2472 (1988).

[5] G. Binasch, P. Grünberg, F. Saurenbach, and W. Zinn, *Phys. Rev. B* **39**, 4828 (1989).

[6] F. Meier and B. P. Zakharchenya, *Optical Orientation* (Elsevier Science, 1984).

[7] P. R. Hammar, B. R. Bennett, M. J. Yang, and Mark Johnson *Phys. Rev. Lett.* **83**, 203 (1999).

[8] E. I. Rashba, *Phys. Rev. B* **62**, R16267 (2000).

[9] J. S. Moodera, J. Nowak, and R. J. M. van de Veerdonk, *Phys. Rev. Lett.* **80**, 2941 (1998).

[10] X. Lou, C. Adelmann, S. A. Crooker, E. S. Garlid, J. Zhang, K. S. M. Reddy, S. D. Flexner, C. J. Palmstrom, and P. A. Crowell, *Nature Phys.* **3**, 197 (2007).

[11] D. Saha, M. Holub, P. Bhattacharya, and Y. C. Liao, Appl. Phys. Lett. 89, 142504 (2006).

[12] Y. K. Kato, R. C.Myers, A. C. Gossard, D. Awschalom, *Science* **306**,1910(2004).

[13] J. N. Chazalviel, *Phys. Rev. B* **11**, 3918 (1975).

[14] R. J. Elliott, *Phys. Rev.* **96**, 266 (1954).

[15] M. I. D'yakonov and V. I. Perel', *Sov. Phys. Solid. State* **13**, 3023 (1971).

[16] G. L. Bir, A. G. Aronov, and G. E. Pikus, *Sov. Phys. JETP* **42**, 705 (1976).

[17] I. Zutic, J. Fabian, and S. Das Sarma, *Rev. Mod. Phys.,* **76**, 2 (2004).

[18] R. H. Silsbee and F. Beuneu, *Phys. Rev. B* **27**, 2682 (1983).

[19] J. Fabian, A. Matos-Abiaguea, C. Ertlera, P. Stano and I. Zˇutic´, *Acta physica slovaca* **57,** 565 (2007).

[20] D'yakonov, M. I., and V. I. Perel', *Sov. Phys. JETP* **38**, 177 (1973).

[21] R. I. Dzhioev, K. V. Kavokin, V. L. Korenev, M. V. Lazarev, B. Y. Meltser, M. N. Stepanova, B. P. Zakharchenya, D. Gammon, and D. S. Katzer, *Phys. Rev. B* **66**, 245204 (2002).

[22] J. M. Kikkawa and D. D. Awschalom*, Phys. Rev. Lett.* **80**, 4313 (1998).

[23] Yu. A. Bychkov and E. I. Rashba, *J. Phys. C* **17**, 6039 (1984).

[24] G. Dresselhaus, *Phys. Rev.* **100**, 580 (1955).

[25] Yu. A. Bychkov and E. I. Rashba, *JETP Lett.* **39**, 78 (1984).

[26] S. Datta and B. Das, *Appl. Phys. Lett.* **56**, 665 (1990).

[27] J. Nitta, T. Akazaki, H. Takayanagi, and T. Enoki, *Phys. Rev. Lett.* **78**, 1335 (1997).

[28] T. Koga, J. Nitta, T. Akazaki, and H. Takayanagi, *Phys. Rev. Lett.* **89**,046801 (2002).

[29] N. S. Averkiev, L. E. Golub, and M. Willander, *J. Phys.: Condens. Matter* **14**, R271 (2002).

[30] S. D. Ganichev, E. L. Ivchenko, V. V. Belkov, S. A. Tarasenko, M. Sollinger, D. Weiss, W. Wegschelder, and W. Prettl, *Nature* **417**, 153 (2002).

[31] S. D. Ganichev, E. L. Ivchenko, S. N. Danilov, J. Eroms, W. Wegscheider, D. Weiss, and W. Prettl, *Phys. Rev. Lett.* **86**, 4358 (2001).

[32] S. D. Ganichev, V. V. Bel'kov, L. E. Golub, E. L. Ivchenko, P. Schneider, S. Giglberger, J. Eroms, J. De Boeck, G. Borghs, W. Wegscheider, D. Weiss, and W. Prettl, *Phys. Rev. Lett.* **92**, 256601 (2004).

[33] H. Ohno, Science 281, 951 (1998).

[34] R. C. Myers, B. L. Sheu, A. W. Jackson, A. C. Gossard, P. Schiffer, N. Samarth & D. D. Awschalom. *Phys. Rev. B* **74**, 155203 (2006).

[35] B. T. Jonker, G. Kioseoglou, A. T. Hanbicki, C. H. Li, and P. E. Thompson, *Nat. Phy.* **3**, 542 (2007).

[36] P. V. Dorpe, Z. Liu, W. V. Roy, V. F. Motsnyi, M. Sawicki, G. Borghs, and J. D. Boeck, *Appl. Phys. Lett.* **84**, 3495 (2004).

[37] I. Appelbaum, B. Huang, and D. J. Monsma, *Nature* **447**, 295 (2007).

[38] S. P. Dash, S. Sharma, R. S. Patel, M. P. de Jong, and R. Jansen, *Nature* **462**, 491 (2009).

[39] E. D. Fraser, S. Hegde, L. Schweidenback, A. H. Russ, A. Petrou, H. Luo, and G. Kioseoglou, *Appl. Phys. Lett.* **97**, 041103 (2010).

[40] J.M.D. Coey and C.L. Chien, *MRS Bulletin* **720** (2003).

[41] C. Palmstrom, *MRS Bulletin* **725** (2003).

[42] H. Dery, P. Dalal, L. Cywinski, and L. J. Sham, Nature **447**, 573 (2007).

[43] H. Dery, L. Cywinski, and L. J. Sham, *Phys. Rev. B* **73**, 161307(R) (2006).

[44] R. Vrijen, E. Yablonovitch, K. Wang, H. W. Jiang, A. Balandin, V. Roychowdhury, T. Mor, and D. DiVincenzo, *Phys. Rev. A* **62**, 012306 (2000).

[45] C. Ciuti, J. P. McGuire, and L. J. Sham, *Appl. Phys. Lett.* **81**, 4781 (2002).

[46] S. Datta, *Appl. Phys. Lett.* **87**, 013115 (2005).

[47] M. Kohda, Y. Ohno, K. Takamura, F. Matsukura, and H. Ohno, *Jpn. J. Appl. Phys.* **40**, L1274 (2001).

[48] J. Rudolph, D. Hagele, H. M. Gibbs, G. Khitrova, and M. Oestreich, *Appl. Phys. Lett.* **82**, 4516 (2003).

[49] M. E. Flatt´e, and G. Vignale, *Appl. Phys. Lett.* **78**, 1273 (2001).

[50] R. Fiederling, M. Kleim, G. Reuscher, W. Ossau, G. Schmidt, A. Waag, and L. W. Molenkamp, *Nature* **402**, 787 (1999).

[51] H. Ohno, D. Chiba, F. Matsukura, T. O. E. Abe, T. Dietl, Y. Ohno, and K. Ohtani, *Nature* **408**, 944 (2000).

[52] W. Wetzels, G. E.W. Bauer, and M. Grifoni, *Phys. Rev. B* **72**, 020407(R) (2005).

[53] D. Nikonov http://arxiv.org/abs/cond-mat/0605298, 2006.

[54] F. Heusler, *Z. Angew. Chem.* **17** 260 (1904).

[55] S. Hilpert and T. Dieckmann, Ber. Dtsch. *Chem. Ges. A*, **44,** 2378 (1911).

[56] B. T. M. Willis and H. P. Rooksby, *Proc. Phys. Soc. London B*, **67,** 290 (1954).

[57] R. H. Wilson and J. S. Kasper, *Acta Cryst.* **17**, 95 (1964).

[58] L. M. Sandratskrii, F. Egorov and A. A. Berdyshev, *Phys. stat. sol. (b)* **103**, 511 (1981).

[59] F. Schippan, M. Kästner, L. Däweritz and K. H. Ploog, *Appl. Phys. Lett.* **76,** 834 (2000).

[60] D. K. Satapathy, B. Jenichen, V. M. Kaganer, W. Braun, L. Däweritz, and K. H. Ploog *J. Vac. Sci. Technol. B* **22**, 2079 (2004).

[61] M. Tanaka, J. P. Harbison, M. C. Park, Y. S. Park, T. Shin, and G. M. Rothberg, *Appl. Phys. Lett.* **65**, 1964 (1994).

[62] A. K. Das, C. Pampuch, A. Ney, T. Hesjedal, L. Däweritz, R. Koch, and K. H. Ploog, *Phys. Rev. Lett.* **91**, 087203 (2003).

[63] P. Wolniansky, S. Chase, R. Rosenvold, M. Ruane, and M. Mansuripur, *J. Appl. Phys.* **60**, 346 (1986).

[64] R. Engel-Herbert, T. Hesjedal, D. M. Schaadt, L. Däweritz, and K. H. Ploog, *Appl. Phys. Lett.* **88**, 052505 (2006).

[65] R.W. De Blois and D.S. Rodbell, *Phys. Rev.* **130,** 1347 (1963).

[66] A.H.V. Repetto Llamazaresa, J. Milanoa, L.B. Sterena, V. Garciab, M. Marangolob, M. Eddriefb and V.H. Etgensb, *Physica B* **398,** 372 (2007).

[67] A. Ney, T. Hesjedal, C. Pampuch, J. Mohanty, A. K. Das, L. Däweritz, R. Koch, and K. H. Ploog, *Appl. Phys. Lett.* **83,** 2850 (2003).

[68] D. Saha, L. Siddiqui, P. Bhattacharya, S. Datta, D. Basu, and M. Holub, *Phys. Rev. Lett.* **100**, 196603 (2008).

[69] D. Basu, D. Saha, and P. Bhattacharya, *Phys. Rev. Lett.* **102**, 093904 (2009).

[70] M. Holub, J. Shin, D. Saha, and P. Bhattacharya, *Phys. Rev. Lett.* **98**, 146603 (2007).

[71] D. Saha, M. Holub, and P. Bhattacharya, *Appl. Phys. Lett.* **91**, 072513 (2007).

[72] S. Datta and B. Das, *Appl. Phys. Lett.* **56**, 665 (1990) and J. H. Kwon, H. C. Koo, J. Chang, S. H. Han, and J. Eom, *Appl. Phys. Lett.* **90**, 112505 (2007).

[73] H. C. Koo, J. H. Kwon, J. Eom, J. Chang, S. H. Han, and M. Johnson, *Science* **325**, 1515 (2009).

[74] H. Koo, H. Yi, J. B. Ko, J. Chang, S. H. Han, D. Jung, S. G. Huh, and J. Eom, *Appl. Phys. Lett.* **90,** 022101 (2007).

[75] D. Basu, P. Bhattacharya, W. Guo, and H. Kum, *J. Phys. D: Appl. Phys.* **42**, 092001 (2009).

[76] Y. Y. Wang and M. W. Wu, *Phys. Rev. B* **72**, 153301 (2005).

[77] See EPAPS supplementary material at http://dx.doi.org/10.1063/1.3268432 for data on control devices. [EPAPS]

[78] N. S. Averkiev, L. E. Golub, and M. Willander, *Semiconductors* **36**, 91 (2002).

[79] M. H. Liu and C. R. Chang, *Phys. Rev. B* **74**, 195314 (2006).

[80] R. Mattana, J.-M. George, H. Jaffrès, F. Nguyen Van Dau, A. Fert, B. Lépine, A. Guivarc'h, and G. Jézéquel, *Phys. Rev. Lett.* **90**, 166601 (2003).

[81] Y. Mizuno, S. Ohya, P. N. Hai, and M. Tanaka, *Appl. Phys. Lett.* **90**, 162505 (2007).

[82] S. Ohya, I. Muneta, P. N. Hai, and M. Tanaka, *Phys. Rev. Lett.* **104**, 167204 (2010).

[83] Y. G. Chai, R. Chow, and C. E. C. Wood, *Appl. Phys. Lett.* **39,** 800 (1981).

[84] M. Tanaka, J. P. Harbison, M. C. Park, Y. S. Park, T. Shin, and G. M. Rothberg, *J. Appl. Phys.* **76**, 6278 (1994).

[85] See EPAPS Document No. E-PRLTO. For more information on EPAPS, see http://www.aip.org/pubservs/epaps.html. (2010).

[86] R. P. Panguluri, G. Tsoi, B. Nadgorny, S. H. Chun, N. Samarth, and I. I. Mazin, *Phys. Rev. B*, **68**, 201307(R) (2003).

[87] R. H. Fowler and L. Nordheim, *Proceedings of the Royal Society of London* **119**, 173 (1928).

[88] S. Yuasa, T. Nagahama, A. Fukushima, Y. Suzuki, and K. Ando, *Nat. Mat.* **3**, 869 (2004).

[89] H.J.M. Swagten from *Handbook of Magnetic Materials*, Edited by K. H. J. Buschow

(Elsevier BV, Amsterdam,2003)

[90] R. Tsu and L. Esaki, *Appl. Phys. Lett.* **22**, 562 (1973).

[91] Z. G. Yu and M. E. Flatte, *Phys. Rev. B* **66**, 201202 (2002).

[92] Y. Xu, D. Ephron, and M. R. Beasley, *Phys. Rev. B* **52**, 2843 (1995).

[93] J. H. Jiang and M. W. Wu, *Phys. Rev. B* **79**, 125206 (2009).

[94] S. Hallstein, *et.al, Phys. Rev. B* **56**, R7076 (1997).

[95] H. Ando, T. Sogawa, and H. Gotoh, *Appl. Phys. Lett.* **73**, 566 (1998).

[96] K. D. Choquette, D. A. Richie, and R. E. Leibenguth, *Appl. Phys. Lett.* **64,** 2062 (1994).

[97] M. Shimuzi, T. Mukaihara, F. Koyama, and K. Iga, *Electron. Lett.* **27,** 1067 (1991).

[98] S. A. Crooker, *et.al*, *Phys. Rev. B* **56**, 7574 (1997).

[99] J. Rudolph, S. Dohrmann, D. Hagele, M. Oestreich, and W. Stolz, *Appl. Phys. Lett.* **87,** 241117(2005).

[100] I. Žutić, J. Fabian, and S. D. Sarma, *Rev. Mod. Phys.* **76**, 323 (2004).

[101] Y. Ohno, *et.al*, *Physica E (Amsterdam)* **6**, 817 (2000).

[102] M. Paillard, *et.al*, *Appl. Phys. Lett*. **76,** 76 (2000).

[103] A. Tackeuchi, R. Ohtsubo, K. Yamaguchi, M. Murayama, T. Kitamura, T. Kuroda, and T. Takagahara, *Appl. Phys. Lett.* **84**, 3576 (2004).

[104] D. V. Kuksenkov, H. Temkin, and S. Swirhun, *Appl. Phys. Lett*. **67**, 2141 (1995).

[105] N. Kirstaedter, O. G. Schmidt, N. N. Ledentsov, D. Bimberg, V. M. Ustinov, A. Y. Egorov, A. E. Zhukov, M. V. Maximov, P. S. Kopev, and Z. I. Alferov, *Appl. Phys. Lett.* **69**, 1226 (1996).

[106] I. Novikov, *et.al*, *Semiconductors* **39**, 481 (2005).

[107] L. V. Dao, *et.al*, *Appl. Phys. Lett.* **73**, 3408 (1998).

[108] R. Ram, E. Goobar, M. Peters, L. Coldren, and J. Bowers, *IEEE Photonics Technol. Lett.* **8**, 599 (1996).

[109] Optical Orientation, edited by F. Meier and B. P. Zakharchenya (Elsevier Science, Amsterdam, 1984).

[110] D. Basu, D. Saha, C. C. Wu, M. Holub, Z. Mi, and P. Bhattacharya *Appl. Phys. Lett.* **92**, 091119 (2008).

[111] M. San Miguel, Q. Feng, and J. V. Moloney, *Phys. Rev. A* **52**, 1728 (1995).

[112] See EPAPS Document No. E-PRLTAO-102-006912 for derivation of all the analytical expressions for a spin laser. For more information on EPAPS see, http://www.aip.org/pubservs/epaps.html (2008).

[113] S. Ghosh, P. Bhattacharya, E. Stoner, J. Singh, H. Jiang, S. Nuttinck, and J. Laskar, *Appl. Phys. Lett.* **79**, 722 (2001).

[114] P. Bhattacharya, *Semiconductor Optoelectronic Devices* (Prentice Hall, 1996).

[115] K. Y. Lau, N. Bar-Chaim, I. Ury, Ch. Harder, and A. Yariv, *Appl. Phys. Lett.* **43**, 1 (1983).

[116] H. Dery, G. Eisenstein, *IEEE J. Quant. Electron.* **40,** 1398 (2004).

[117] C. H. Li, G. Kioseoglou, O. M. J. van 't Erve, M. E. Ware, D. Gammon, R. M. Stroud, B. T. Jonker, R. Mallory, M. Yasar, and A. Petrou, *Appl. Phys. Lett.* **86,** 132503 (2005).

[118] Rafał Oszwałdowski, Christian Gøthgen, and Igor Žutić, *Phys. Rev. B*, **82**, 085316 (2010).

[119] J. Lee, W. Falls, R. Oszwałdowski, and I. Žutić, *Appl. Phys. Lett.* **97**, 041116

(2010).

[120] T. Shibata, K. Soai, *Angew. Chem., Int. Ed.* **40**, 1096 (2001).

[121] M. Holub and P. Bhattacharya, *J. Phys. D* **40**, R179 (2007).

[122] D. Bimberg, N. Kirstaedter, N. N. Ledentsov, Zh. I. Alferov, P. S. Kop'ev, V. M. Ustinov, *IEEE J. Quantum Electron.* **3**,196 (1997).

[123] G. Kioseoglou, A.T. Hanbicki, J.M. Sullivan, O.M.J van't Erve, C.H. Li, S.C. Erwin, R. Mallory, M. Yasar, A. Petrou, and B.T. Jonker, *Nature Materials*, **3**, 799-803, (2004).

[124] S. Hövel, N. C. Gerhardt, M. R. Hofmann, F.-Y. Lo, A. Ludwig, D. Reuter, A. D. Wieck, E. Schuster, H. Wende, W. Keune, O. Petracic, and K. Westerholt, *Appl. Phys. Lett.* **93**, 021117 (2008).

[125] S. Ikeda, K. Miura, H. Yamamoto, K. Mizunuma, H. D. Gan, M. Endo, S. Kanai, J. Hayakawa, F. Matsukura & H. Ohno, *Nature. Mater.* **9,** 721 (2010).